Charge Carrier Dynamics in Nontoxic Semiconductor Quantum Dots

Alexander Florian Richter

München, Oktober 2020

Charge Carrier Dynamics in Nontoxic Semiconductor Quantum Dots

Dissertation

to obtain the doctoral degree of natural sciences (Dr. rer. nat.)

at the Faculty of Physics

of the Ludwig-Maximilians-Universität München

submitted by

Alexander Florian Richter

from Ebersberg

Munich, 13. October 2020

First referee:	Prof. Dr. Jochen Feldmann
Second referee:	Prof. Dr. Marcus Scheele
Date of oral examination:	15. December 2020

Ladungsträgerdynamik in ungiftigen Halbleiter-Quantenpunkten

Dissertation

zur Erlangung des Doktorgrades der Naturwissenschaften (Dr. rer. nat.)

an der Fakultät für Physik

der Ludwig-Maximilians-Universität München

vorgelegt von

Alexander Florian Richter

aus Ebersberg

München, 13. Oktober 2020

Erstgutachter:	Prof. Dr. Jochen Feldmann
Zweitgutachter:	Prof. Dr. Marcus Scheele
Tag der mündlichen Prüfung:	15. Dezember 2020

Publications, Conferences, and Awards

Scientific Publications of Results Presented in This Work

- A. F. Richter, M. Binder, B. J. Bohn, N. Grumbach, S. Neyshtadt, A. S. Urban, J. Feldmann
  Fast Electron and Slow Hole Relaxation in InP-Based Colloidal Quantum Dots
  ACS Nano 13 (12), 14408-14415 (2019)

- A. Dey,[†] A. F. Richter,[†] T. Debnath, H. Huang, L. Polavarapu, J. Feldmann
  Transfer of Direct to Indirect Bound Excitons by Electron Intervalley Scattering in $Cs_2AgBiBr_6$ Double Perovskite Nanocrystals
  ACS Nano 14 (5), 5855–5861 (2020)

Additional Publications

- V. A. Hintermayr, A. F. Richter, F. Ehrat, M. Döblinger, W. Vanderlinden, J. A. Sichert, Y. Tong, L. Polavarapu, J. Feldmann, A. S. Urban
  Tuning the Optical Properties of Perovskite Nanoplatelets through Composition and Thickness by Ligand-Assisted Exfoliation
  Advanced Materials 28 (43), 9478-9485 (2016)

- B. J. Bohn, T. Simon, M. Gramlich, A. F. Richter, L. Polavarapu, A. S. Urban, J. Feldmann
  Dephasing and Quantum Beating of Excitons in Methylammonium Lead Iodide Perovskite Nanoplatelets
  ACS Photonics 5 (2), 648-654 (2017)

- Y. Tong, M. Fu, E. Bladt, H. Huang, A. F. Richter, K. Wang, P. Müller-Buschbaum, S. Bals, P. Tamarat, B. Lounis, J. Feldmann, L. Polavarapu
  Chemical Cutting of Perovskite Nanowires into Single-Photon Emissive Low-Aspect-Ratio $CsPbX_3$ (X = Cl, Br, I) Nanorods
  Angewandte Chemie, International Edition 130 (49), 16326-16330 (2018)

- Y. Li, H. Huang, Y. Xiong, A. F. Richter, S. V. Kershaw, J. Feldmann, A. L. Rogach
  Using Polar Alcohols for the Direct Synthesis of Cesium Lead Halide Perovskite Nanorods with Anisotropic Emission
  ACS Nano 13 (7), 8237-8245 (2019)

- H. Huang, Y. Li, Y. Tong, E-P. Yao, M. W. Feil, A. F. Richter, M. Döblinger, A. L. Rogach, J. Feldmann, L. Polavarapu
  Spontaneous Crystallization of Perovskite Nanocrystals in Nonpolar Organic Solvents: A Versatile Approach for Their Shape-Controlled Synthesis
  Angewandte Chemie, International Edition 58 (46), 16558-16562 (2019)

- P. I. Scheurle, A. Mähringer, A. C. Jakowetza, P. Hosseinid, A. F. Richter, G. Wittstockd, D. D. Medina, T. Bein
  A Highly Crystalline Anthracene-Based MOF – 74 Series Featuring Electrical Conductivity and Luminescence
  Nanoscale 11 (43), 20949-20955 (2019)

- Y. Xiong,† X. Zhang,† A. F. Richter,† Y. Li, A. Döring, P. Kasák, A. Popelka, J. Schneider, S. V. Kershaw, S. Jo Yoo, J-G. Kim, W. Zhang, W. Zheng, E. V. Ushakova, J. Feldmann, A. L. Rogach
  Chemically Synthesized Carbon Nanorods with Dual Polarized Emission
  ACS Nano 13 (10), 12024-12031 (2019)

- S. Rieger, B. J. Bohn, M. Döblinger, A. F. Richter, Y. Tong, K. Wang, P. Müller-Buschbaum, L. Polavarapu, L. Leppert, J. K. Stolarczyk, J. Feldmann
  Excitons and Narrow Bands Determine the Optical Properties of Cesium Bismuth Halides
  Physical Review B 100 (20), 201404 (2019)

- H. Huang, L. Wu, Y. Wang, A. F. Richter, M. Döblinger, J. Feldmann
  Facile Synthesis of $FAPbI_3$ Nanorods
  Nanomaterials 10 (1), 72 (2020)

- S. Paul, E. Bladt, A. F. Richter, M. Döblinger, Y. Tong, H. Huang, A. Dey, S. Bals, T. Debnath, L. Polavarapu, J. Feldmann
  Manganese-Doping-Induced Quantum Confinement within Host Perovskite Nanocrystals through Ruddlesden-Popper Defects
  Angewandte Chemie, International Edition 59 (17), 6794-6799 (2020)

- H. Huang, M. W. Feil, S. Fuchs, T. Debnath, A. F. Richter, Y. Tong, L. Wu, Y. Wang, M. Döblinger, B. Nickel
  Growth of Perovskite $CsPbBr_3$ Nanocrystals and Their Formed Superstructures Revealed by In Situ Spectroscopy
  Chemistry of Materials 32 (20), 8877–8884 (2020)

- B. Heyne, K. Arlt, A. Geßner, A. F. Richter, M. Döblinger, J. Feldmann, A. Taubert, A. Wedel
  Mixed Mercaptocarboxylic Acid Shells Provide Stable Dispersions of InPZnS/ZnSe/ZnS Multishell Quantum Dots in Aqueous Media
  Nanomaterials 10 (9), 1858 (2020)

Conferences and Workshops

- *Workshop on Optical Spectroscopy of New Materials* (Talk)
  Syracuse, Italy, March 2017

- *German Physical Society (DPG) Spring Meeting* (Talk)
  Dresden, Germany, March 2017

- *International WE-Heraeus-Physics School on Exciting Nanostructures: Probing and Tuning the Electronic Properties of Confined Systems* (Poster)
  Bad Honnef, Germany, July 2017

- *Nanosystems Initiative Munich (NIM) Summer Retreat* (Poster)
  Beilngries, Germany, July 2017

- *Electroluminescent Quantum Materials-Based Light-Emitting Device (ELQ-LED): Project Kick-Off Meeting*
  Darmstadt, Germany, August 2017

- 6^{th} *International Solar Technologies go Hybrid (SolTech) Conference* (Poster)
  Munich, Germany, October 2017

- *ELQ-LED:* 1^{st} *Project Meeting* (Talk)
  Potsdam, Germany, January 2018

- 10^{th} *Biannual Conference on Quantum Dots* (Poster)
  Toronto, Canada, June 2018

- *ELQ-LED:* 2^{nd} *Project Meeting* (Talk)
  Oldenburg, Germany, August 2018

- *Center for NanoScience (CeNS) Workshop Venice 2018: Celebrating NanoScience* (Poster)
  Venice, Italy, September 2018

- *ELQ-LED:* 3^{rd} *Project Meeting* (Talk)
  Augsburg, Germany, February 2019

- *Workshop on Optical Spectroscopy of New Materials 2019* (Talk)
  Haigerloch, Germany, March 2019
- *ELQ-LED: 4th Project Meeting* (Talk)
  Munich, Germany, September 2019
- *NaNaX 9: Nanoscience with Nanocrystals* (Poster)
  Hamburg, Germany, September 2019
- *ELQ-LED: 5th Project Meeting* (Talk)
  Online, April 2020
- *iCQD: Internet Conference for Quantum Dots* (Talk)
  Online, July 2020
- *11th International Conference on Quantum Dots* (Poster)
  Online, December 2020

Awards

- **CeNS Publication Award, Best Junior Scientist Publication**
  for *"Tuning the Optical Properties of Perovskite Nanoplatelets through Composition and Thickness by Ligand-Assisted Exfoliation"* in *Advanced Materials*
  Munich, Germany, November 2016

- **Best Poster Award**
  International WE-Heraeus-Physics School on Exciting Nanostructures: Probing and Tuning the Electronic Properties of Confined Systems
  Bad Honnef, Germany, July 2017

- **CeNS Publication Award, Best Junior Scientist Publication**
  for *"Chemical Cutting of Perovskite Nanowires into Single-Photon Emissive Low-Aspect Ratio $CsPbX_3$ (X = Cl, Br, I) Nanorods"* in *Angewandte Chemie, International Edition*
  Munich, Germany, November 2018

- **Best Poster Award** by ACS Nano
  NaNaX 9: Nanoscience with Nanocrystals
  Hamburg, Germany, September 2019

- **CeNS Publication Award, Best Junior Scientist Publication**
  for *"Spontaneous Crystallization of Perovskite Nanocrystals in Nonpolar Organic Solvents: A Versatile Approach for their Shape-Controlled Synthesis"* in *Angewandte Chemie, International Edition*
  Munich, Germany, November 2019

- **ACS Editors' Choice**
  for *"Transfer of Direct to Indirect Bound Excitons by Electron Intervalley Scattering in $Cs_2AgBiBr_6$ Double Perovskite Nanocrystals"* in *ACS Nano*
  April 2020

Zusammenfassung

Die Verwendung ungiftiger Halbleiter-Nanokristalle für optoelektronische Anwendungen erfordert eine genaue Kenntnis deren physikalischer Eigenschaften. Die bisherige Forschung konzentrierte sich allerdings auf Materialien, die giftige Elemente wie Blei oder Cadmium enthalten. Für kommerzielle Anwendungen sind diese jedoch nicht geeignet. Daher wurden für diese Arbeit ungiftige Nanokristalle mittels optischer Spektroskopie untersucht. Somit konnten Vorteile und Herausforderungen für die Entwicklung von zukünftigen Bauelementen benannt werden.

Kolloidale Quantenpunkte sind helle Lichtquellen, die in der nächsten Generation von Leuchtdioden Verwendung finden könnten. Im Gegensatz zu den Cadmium-basierten Varianten werden hier Kern/Schale-Quantenpunkte auf Indiumphosphid-Basis untersucht. Für diese konnten die genauen Relaxationszeiten von Ladungsträgern bestimmt werden. Mit zunehmender Überschussenergie dauert die Relaxation länger. Interessanterweise relaxieren Elektronen trotz größerer energetischer Lücken zwischen den diskreten Energieniveaus schneller als Löcher. Dies konnte mit einem effizienten Auger-ähnlichen Streumechanismus erklärt werden. Darüber hinaus nimmt die Relaxationszeit sogar um eine Größenordnung zu und erreicht Pikosekunden, wenn Löcher aus der Schale in den Kern relaxieren müssen. Aufgrund dieses langsamen Prozesses können Löcher von Fallenzuständen eingefangen werden, was zu strahlungsfreier Rekombination führt. Daher ist eine optimierte Ladungsträgerinjektion für die Entwicklung von effizienten Bauelementen nötig.

Als zweites Materialsystem wurde die Gruppe der Perowskite untersucht. Diese ermöglichen eine kostengünstige und einfache Herstellung von hocheffizienten Solarzellen, enthalten aber meist Blei. Eine mögliche Alternative stellen bleifreie Doppelperowskit-Nanokristalle dar. Für diese wurde die Ladungsträgerdynamik auf Basis ihrer indirekten Bandstruktur charakterisiert. Es konnte gezeigt werden, dass defektbedingt gebundene Exzitonen hierbei eine maßgebliche Rolle spielen. Diese Exzitonen führen nicht nur zu einem deutlichen Absorptionsmaximum unterhalb des direkten Bandkantenübergangs, sondern auch zu einer hochenergetischen Emission. Dies ist überraschend, da die Elektronen innerhalb von 10 ps zum Leitungsbandminimum streuen. Dadurch nehmen die Exzitonen einen indirekten Charakter an und die Photolumineszenz verschiebt sich um 1 eV in den roten Spektralbereich, wo die Hauptemission beobachtet werden kann. Somit zeigen diese Ergebnisse den großen Einfluss von Defektzuständen auf die optischen Eigenschaften und die Ladungsträgerdynamik.

Die Resultate dieser Arbeit demonstrieren, dass es möglich ist giftige Elemente bei Nanokristallen zu vermeiden und trotzdem vielversprechende optoelektronische Eigenschaften zu erzielen. Die Charakterisierung der Ladungsträgerdynamik mittels optischer Spektroskopie ist gleichzeitig ein wichtiger Beitrag für die Entwicklung von zukünftigen Anwendungen.

Abstract

The use of nontoxic semiconductor nanocrystals for optoelectronic applications requires precise knowledge of their physical properties. The previous research, though, has focused on materials that contain toxic elements such as lead or cadmium. However, these are not suitable for commercial applications. Therefore, in this thesis, nontoxic nanocrystals were investigated by optical spectroscopy. Thus, advantages and challenges for the development of future devices could be identified.

Colloidal quantum dots are bright emitters that may be used in the next generation of light-emitting diodes. In contrast to the cadmium-based variants, core/shell quantum dots based on indium phosphide are here investigated. It was possible to determine the exact relaxation time scales of charge carriers. With increasing excess energy the relaxation takes longer. Interestingly, electrons relax faster than holes despite larger energy gaps between the discrete energy levels. This can be explained by an efficient Auger-like scattering mechanism. Furthermore, the relaxation time increases even by an order of magnitude reaching several picoseconds if holes have to relax from the shell into the core. Due to this slow process, hole trapping becomes significant and leads to nonradiative recombination. Therefore, an optimized charge carrier injection process is necessary for the development of efficient devices.

As a second material system, the group of perovskites was investigated. They enable a cheap and facile production of highly efficient solar cells, but mostly contain lead. A possible alternative is given by lead-free double perovskite nanocrystals. For these, the charge carrier dynamics was characterized based on their indirect electronic band structure. It could be shown that defect-related bound excitons play a significant role in this process. These excitons not only cause a strong absorption peak below the direct band edge transition but also give rise to a high-energetic emission. This is surprising since the electrons scatter within 10 ps toward the conduction band minimum. Thus, the excitons become indirect and the photoluminescence shifts by 1 eV into the red spectral region, where the main emission peak can be observed. Hence, these results show the important role of defect states for the optical properties and charge carrier dynamics.

The results of this thesis demonstrate that it is possible to avoid toxic elements in nanocrystals and still achieve desirable optoelectronic properties. The characterization of the charge carrier dynamics by optical spectroscopy is also an important contribution to the development of future applications.

Table of Contents

1

Introduction

There's Plenty of Room at the Bottom — with this famous lecture, Richard Feynman predicted the enormous potential of nanotechnology already in 1959.[1] His main message was that different physical processes dominate on a nanometer length scale compared to the macroscopic world and that this will enable new applications. With the development of electron microscopy, the research on the nanoscale made huge progress in the following decades and a subfield of nanotechnology focused on colloidal nanocrystals (NCs). Nowadays, there is a huge variety of NCs showing different shapes such as spheres, cubes, platelets, rods, wires, and tetrapods. Furthermore, these NCs can be made of various materials: CdSe, Au, Cu_2O, PbS, Fe_2O_3, and many more. Notably, the diversity of NCs enables multifarious optoelectronic applications including light-emitting diodes (LEDs), photovoltaics, plasmonics, bioimaging, biomedicine, and telecommunication.[2]

However, semiconductor NCs that show a high performance in various applications are usually made of toxic elements. This hinders further commercialization given the fact that most of these chemical elements including lead and cadmium are even banned in almost all electronic products by the European Union.[3] Accordingly, there is a need for new nontoxic material systems with comparable performance. In this thesis, two of them are investigated in order to characterize the advantages and challenges regarding optoelectronic applications.

The first field of interest are colloidal quantum dots (QDs). They are not only a topic of fundamental research but also an important component in various applications. Especially, their size-dependent optical properties and solution-based low-cost synthesis are of major interest for the industry. So far, QDs are for example used as fluorescent labels in bioimaging applications,[4] as infrared absorbers in solution-processed photovoltaics,[5] and as

bright emitters in LEDs.[6,7] Notably, the combination of a tunable emission color and a narrow linewidth enables displays with an enhanced color gamut compared to other technologies.[8] Nevertheless, these applications typically rely on toxic components such as cadmium in order to achieve excellent performance.[9,10] Recently, it was shown that InP-based QDs are a promising candidate that could be used to replace cadmium.[11,12] In this thesis, the focus lies on QDs emitting in the red spectral region. LEDs with such an emission are not only needed for displays in combination with blue and green ones but also allow for applications on their own (*e. g.*, as car rear lights). My research on these QDs was conducted in the scope of a project by the German *Federal Ministry of Education and Research* named *Electroluminescent Quantum Materials-Based Light-Emitting Device (ELQ-LED)*. The goal of this project was to utilize nontoxic QDs for display and lighting applications. With partners from industry (*Merck*, *Osram*) and research (*e. g.*, *Fraunhofer IAP*), it was possible to cover many different aspects concerning the development of a new LED structure. This ranges from the chemical synthesis of QDs *via* fundamental investigations of physical properties to the design and construction of final devices.

The second field of interest is the group of halide perovskites. In particular, the subgroup of lead halide perovskites became popular in the last decade as a new class of semiconducting materials owing to their plethora of intriguing optical properties such as a large absorption cross section, a bright and narrow-band emission, a large diffusion constant of charge carriers, and a high defect tolerance.[13–18] Especially the outstanding efficiency rise of solar cells based on these perovskites caught the attention of a broad research community. Nowadays, they are already competing with the established silicon-based photovoltaic technology.[19] Furthermore, perovskites also show great potential for light-emitting applications since their emission wavelength can be tuned across the complete visible spectrum by changing the crystal morphology and elemental composition.[20–24] Although lead-based halide perovskites facilitate various optoelectronic applications, they show a few drawbacks. The most important ones are their intrinsic instability at ambient conditions[25–27] and the toxicity of lead, which impedes commercialization.[28] Therefore, various nontoxic materials have already been reported that could replace lead-based perovskites. These include the new group of double perovskites (DPs).[29] Nevertheless, further investigations of their physical properties are needed to clarify the real applicability for optoelectronic applications.

A thorough understanding of the physical processes taking place within nanomaterials is needed for the successful development of applications. In this thesis, optical spectroscopy was used to characterize the ultrafast charge carrier dynamics after photoexcitation. On the one hand, colloidal InP/ZnS and InP/ZnSe core/shell QDs will be discussed. On the other hand, $Cs_2AgBiBr_6$ NCs that are a promising type of DPs were investigated. In both cases, the energetic structure of the respective material system plays a crucial role for the understanding of the physical processes taking place. Hence, Chapter 2 highlights the needed

theoretical concepts starting from the semiconductor basics. In Chapter 3, the chemical synthesis of the respective NCs is presented. Moreover, the used experimental techniques of optical spectroscopy are described. On this basis, the optical properties of InP-based QDs are characterized in Chapter 4 and the relaxation dynamics of electrons and holes is investigated in detail. Furthermore, Chapter 5 focuses on the charge carrier dynamics within $Cs_2AgBiBr_6$ DP NCs. Finally, a summary of my findings will be given in Chapter 6.

2

Fundamentals

The following chapter will highlight the physical concepts that are needed for the description of charge carriers within semiconductor NCs. The fundamental energetic band structure of semiconductors will be introduced using the unique example of perovskites. Furthermore, it will be shown how charge carriers behave in such materials. This includes the interaction with light and the formation of excitons. Moreover, the transition to zero-dimensional QDs will be discussed in detail. Namely, the discrete energetic structure of QDs will be derived within the effective mass approximation. Finally, different effects leading to a broadening of optical spectra will be discussed before the chapter closes with an explanation of the so-called phonon bottleneck in QDs.

2.1 Halide Perovskites and Double Perovskites

Back in 1839, Gustav Rose characterized the mineral calcium titanate ($CaTiO_3$), which was found in the Ural Mountains, and named it *perovskite* in honor of the Russian mineralogist Count Lev Alekseyevich von Perovski.[30] Thereupon, all crystals with a general ABX_3 stoichiometry that adopt a similar crystal structure were termed perovskites. The group of cesium lead halide perovskites ($CsPbX_3$, X = Cl, Br, I), which plays a crucial role in the current development of the field, was first discussed in the 1890s.[31] Already in the middle of the 20th century, perovskites became popular in specific research fields, *e. g.*, due to the observation of ferroelectricity ($BaTiO_3$),[32] photoconductivity ($CsPbX_3$),[33] and even layered structures (K_2NiF_4).[34] Nevertheless, they only became known to a broad scientific community

by the demonstration of their strong potential for solar cells at the beginning of the new century.[35]

In this section, various types of halide perovskite crystals including nontoxic DPs will be presented. At the same time, physical concepts needed to explain their properties will be highlighted. A special focus lies hereby on their unique band structure and the role of excitons with regard to their optical properties. Finally, the quantum size effect will be introduced, which enables many new possibilities for their application.

2.1.1 The Great Variety of Perovskites

There is already a large variety of naturally-occurring minerals with a general ABX_3 stoichiometry (*e. g.*, silicates, oxides, fluorides, chlorides, hydroxides, arsenides, antimonides, and intermetallic compounds).[36] However, by employing synthetic methods, crystals can be obtained spanning across the whole periodic table in terms of elemental composition (*e. g.*, metal-free, hybrid organic–inorganic, metallic, and even noble gas-based perovskites).[37] Equation 2.1 defines the Goldschmidt tolerance factor t_G, with r_i corresponding to the respective ionic radii.[38] To enable a stable perovskite structure, t_G must be in the range of 0.8–1.0.[39]

$$t_G = \frac{r_A + r_X}{\sqrt{2}\,(r_B + r_X)} \tag{2.1}$$

The highest symmetric structure adopted by some perovskites corresponds to the $Pm\bar{3}m$ cubic space group (*e. g.*, $SrTiO_3$, $KMgF_3$). As shown in Figure 2.1a, the B and X ions form corner-sharing octahedra (BX_6), while the A ions are located in the voids between them. This

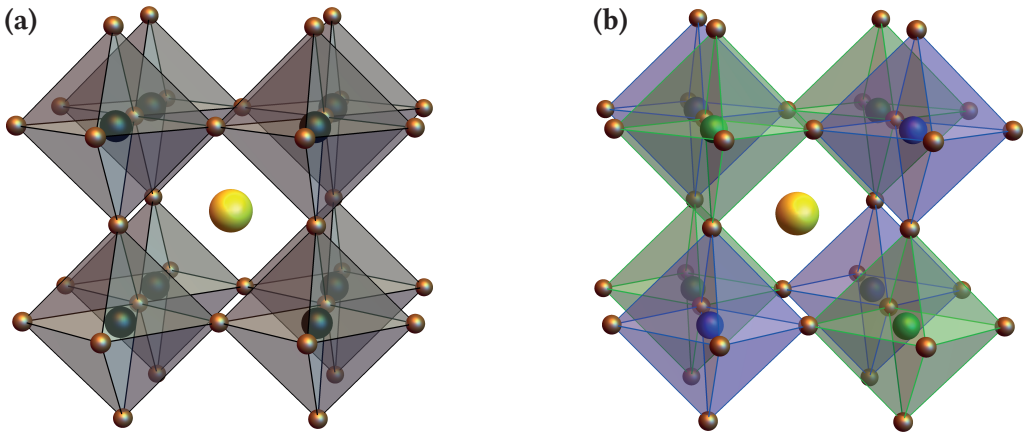

Figure 2.1: Perovskite Crystal Structure. (a) In case of the general ABX_3 stoichiometry, the highest symmetric structure corresponds to the cubic space group $Pm\bar{3}m$. The B and X ions form corner-sharing octahedra, while the A ions are located in the voids between them. A: yellow (*e. g.*, Cs^+), B: black (*e. g.*, Pb^{2+}), and X: brown (*e. g.*, Br^-). **(b)** In the case of an $A_2BB'X_6$ stoichiometry corresponding to DPs, the octahedra are alternately centered by B and B′ ions, while charge balance is maintained. B: blue (*e. g.*, Ag^+), B′: green (*e. g.*, Bi^{3+}).

ideal crystal structure can be modified by, *e. g.*, introducing ordered vacancies, replacing the elements on specific lattice sites, or tilting the octahedra. The last case can be associated with various crystal structure phase transitions depending on the temperature (*e. g.*, from orthorhombic *via* tetragonal to cubic as the temperature increases).[40] Which structure is present at room temperature is closely related to t_G.

Besides variations in the crystal structure and composition, the morphology plays an important role. It may be a macroscopic single crystal or a solid film with similar bulk-like properties. Using methods of colloidal chemistry, NCs can be obtained, whose properties can even be influenced by quantum confinement effects.[23]

In this thesis, the focus lies on perovskite NCs comprising halides. There are the heavily researched organic-inorganic $CH_3NH_3PbX_3$[41] and all-inorganic $CsPbX_3$[42] perovskites. However, the toxicity of lead motivates the investigation of lead-free perovskites. Especially DPs get more and more attention since they may be less toxic (*e. g.*, $Cs_2AgBiBr_6$).[43] They possess a general $A_2BB'X_6$ stoichiometry as shown in Figure 2.1b. In this case, the crystal structure shows alternating octahedra, which are centered by B and B′ cations, respectively. This explains why they are termed *double* perovskite. In the following sections, the optical and electronic properties of the established $CsPbX_3$ and $CH_3NH_3PbX_3$ perovskites are discussed and compared to recent reports on $Cs_2AgBiBr_6$ DP.

2.1.2 Does the Simple and Unique Band Structure of Lead-Based Perovskites Survive?

The periodic arrangement of atoms in a crystalline solid gives rise to many possible delocalized electron states. They are characterized by a certain relation between energy and wave vector, which is known as the *electronic band structure*. The following section outlines the corresponding basic principles.[44] Afterwards, the special case of lead halide perovskites is discussed. The section closes with a presentation of the band structure of lead-free DPs, which shows several differences compared to the one of lead-containing perovskites.

Semiconductor Basics

The Hamiltonian $\mathscr{H}$ describing a crystalline solid comprising M ion cores (including the tightly bound electrons in the inner shells) and N valence electrons is given by Equation 2.2.

$$\mathscr{H} = -\sum_{j=1}^{M} \underbrace{\frac{\hbar^2}{2m_j}\Delta_{\boldsymbol{R}_j}}_{\substack{\text{movement}\\ \text{of cores}}} - \sum_{i=1}^{N} \underbrace{\frac{\hbar^2}{2m_0}\Delta_{\boldsymbol{r}_i}}_{\substack{\text{movement}\\ \text{of electrons}}} + \frac{1}{4\pi\epsilon_0}\left(\sum_{j>j'} \underbrace{\frac{e^2 Z_j Z_{j'}}{|\boldsymbol{R}_j - \boldsymbol{R}_{j'}|}}_{\substack{\text{repulsion}\\ \text{of cores}}} + \sum_{i>i'} \underbrace{\frac{e^2}{|\boldsymbol{r}_i - \boldsymbol{r}_{i'}|}}_{\substack{\text{repulsion}\\ \text{of electrons}}} - \sum_{i,j} \underbrace{\frac{e^2 Z_j}{|\boldsymbol{r}_i - \boldsymbol{R}_j|}}_{\substack{\text{attraction of}\\ \text{electrons and cores}}}\right) \tag{2.2}$$

The core and electron positions are noted by $\boldsymbol{R}_j$ and $\boldsymbol{r}_i$, respectively. The atomic number Z_j and the mass m_j of the atomic cores may vary, whereas the electron mass always equals m_0. $\hbar$, ϵ_0, and e represent the reduced Planck constant, vacuum permittivity, and elementary charge, respectively. Δ_x stands for the Laplace operator (2^{nd} derivative) with respect to the coordinate x. The first two sums equal the kinetic energy $\frac{\hat{\mathbf{p}}^2}{2m}$ of the cores and electrons, respectively, whereby the momentum operator $\hat{\mathbf{p}} = -\mathrm{i}\hbar\nabla$ was used in the position representation. The terms in brackets correspond to the Coulomb interaction between all cores and electrons.

In order to describe all physical properties of a crystal, it would be in principle enough to solve the corresponding Schrödinger equation: $\mathscr{H}\Psi(\boldsymbol{r}_i, \boldsymbol{R}_j) = E\,\Psi(\boldsymbol{r}_i, \boldsymbol{R}_j)$, where $\Psi(\boldsymbol{r}_i, \boldsymbol{R}_j)$ is the wave function of an eigenstate with energy E. However, due to the fact that there are roughly 10^{23} particles per cm^3, there is no realistic chance to solve this equation. Accordingly, several approximations are needed.

The most important one is the so-called *adiabatic* or *Born–Oppenheimer approximation*, which is based on two facts. First, the mass of an ion core is three to five orders of magnitude heavier than the one of a free electron. Second, the forces that bind the outer electrons to an atom are comparable to the ones which bind neighboring atoms. Thus, the electrons can oscillate with a much higher frequency than the cores. Therefore, electrons can instantaneously follow the movement of the cores, but not vice versa. Hence, the wave function can be separated into two parts describing cores and electrons individually.

The periodicity of a crystal with infinite size leads to the fact that a certain point $\boldsymbol{r}$ is indistinguishable from a point $\boldsymbol{r}+\boldsymbol{R}$, where $\boldsymbol{R} = \sum_i n_i \boldsymbol{a}_i$ with integers n_i and the primitive lattice vectors $\boldsymbol{a}_i$ of the underlying Bravais lattice. It is convenient to introduce the so-called *reciprocal lattice* (*k-space*), which is connected to real space *via* Fourier transformation. Harnessing the symmetry of the crystal, it is sufficient to restrict the range of possible $\boldsymbol{k}$-values to a polyhedron in k-space known as the *1st Brillouin zone*. Any larger vector is equivalent to a vector within this zone. Hence, most of the following topics are discussed in k-space instead of real space.

For ions at their equilibrium position in real space, the surrounding potential can be approximated by a parabolic one. This leads to the *harmonic approximation*, which is valid for small dislocations. Thus, certain longitudinal or transversal oscillating modes are possible. These can be described as bosonic quasiparticles known as *phonons*. They are named *acoustic* if the atoms within a unit cell oscillate in phase. If they move out of phase, which requires at least two basis atoms, they are termed *optical*. In this case, an electric dipole may build up during oscillation if an ionic crystal is present. Therefore, optical phonons may scatter with photons, which explains their name. The oscillation of cores in real space can be related to a phonon wave vector $\boldsymbol{k}_{\mathrm{ph}}$ in reciprocal space. The possible modes are characterized by the phonon dispersion, which gives the energy E_{ph} of a phonon with wave vector $\boldsymbol{k}_{\mathrm{ph}}$. Typically, optical phonons have a relatively flat dispersion and an energy in the range of several tens of meV. Acoustic phonons, on the other hand, have a linear dispersion for small $\boldsymbol{k}$ and are less energetic.[45,46]

When describing electrons, the so-called *one-electron approximation* comes into play. It states that the interaction of all electrons and ion cores can be captured in a periodic potential $V(\boldsymbol{r})$ and that it is sufficient to solve the simplified Schrödinger Equation 2.3 for an individual electron.

$$\left(-\frac{\hbar^2}{2m_0}\Delta_{\boldsymbol{r}} + V(r)\right)\Phi(r) = E\,\Phi(r) \tag{2.3}$$

There are essentially two approaches possible. On the one hand, $V(r)$ can be treated as a perturbation. As shown in Figure 2.2a, the parabolic dispersion of a free electron, which leads to plane waves as eigenfunctions, is slightly altered and energetic gaps appear at the border of the 1st Brillouin zone, where no electron states are possible. Due to the crystal symmetry, all dispersion branches have an equivalent within the 1st Brillouin zone, which leads to the reduced zone scheme displayed in Figure 2.2b. On the other hand, a similar result can be found when looking at overlapping wave functions of electrons bound to individual cores. As illustrated by Figure 2.2c, the consequence is an energy splitting between bonding and antibonding states, which results in the formation of energy bands as well.

The electron eigenfunction for such a periodic potential is in both cases given by the so-called *Bloch function* $\Phi_{\boldsymbol{k},\nu}(\boldsymbol{r}) = \mathrm{e}^{\mathrm{i}\boldsymbol{k}\boldsymbol{r}} u_{\boldsymbol{k},\nu}(\boldsymbol{r})$, where ν is the index of a specific band and $u_{\boldsymbol{k},\nu}(\boldsymbol{r})$ is a

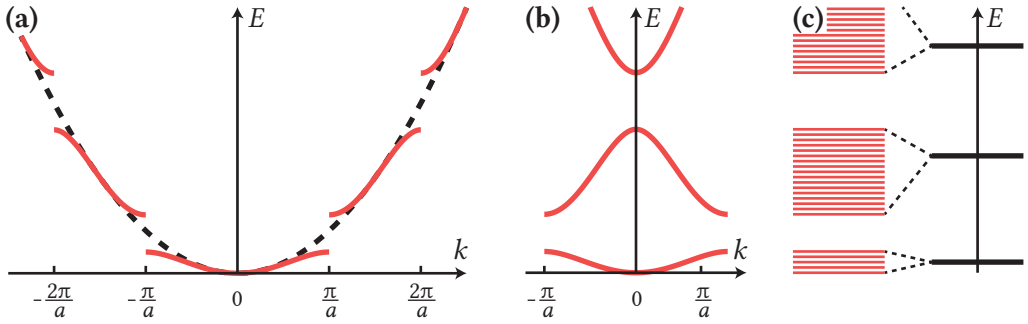

Figure 2.2: Formation of Energy Bands in Crystalline Solids. **(a)** Compared with the parabolic dispersion of a free electron (dashed line), small energetic gaps open at the boarders of the Brillouin zones if an electron is located in a weak potential with periodicity *a*. **(b)** The reduced zone scheme. **(c)** An alternative approach starts from the atomic orbitals of individual atoms (black horizontal lines). If the atoms are located in close vicinity, their interaction leads to a splitting of the atomic levels in as many states as there are atoms. Due to the large number of atoms, energy bands form as well (red horizontal lines). Figure is adapted from Reference 44.

fast oscillating function having the same periodicity as the crystal lattice: $u_{\boldsymbol{k},\nu}(\boldsymbol{r}) = u_{\boldsymbol{k},\nu}(\boldsymbol{r}+\boldsymbol{R})$. Notably, the Bloch function 'remembers' both, the plane wave describing a free electron $e^{i\boldsymbol{k}\boldsymbol{r}}$ and the wave function of the parent atoms, which are connected with the $u_{\boldsymbol{k},\nu}(\boldsymbol{r})$ function. The corresponding energies of specific electron states can be summarized in the *electronic band structure* $E_\nu(\boldsymbol{k})$, which shows certain energetic gaps. The maxima and minima of a specific band typically appear at high-symmetry points like the center (Γ point) or the edges of the 1st Brillouin zone. Furthermore, they can be approximated with a parabolic dispersion. It should be noted, that a *quasi-momentum* $\hbar\boldsymbol{k}$ can be associated with each Bloch function.

The band structure depicts all possible electron states, however, not all of them are occupied in the ground state of the crystal. At 0 K, all states up to the *Fermi energy* E_F are occupied. This energy can be either within a band, which is the case for a metal, or in a band gap. In the latter case, all bands below E_F are named *valence bands (VBs)*, whereas the bands above are referred to as *conduction bands (CBs)*. The band gap energy E_g is thus defined as the energetic difference between the valence band maximum (VBM) and the conduction band minimum (CBM). If minimum and maximum appear at the same point in k-space, the band gap is *direct*, otherwise, it is *indirect*. Materials with a band gap of $0 < E_g \leq 4$ eV are typically classified as semiconductors. If the band gap is larger, an insulator is present. The band gap energies of some materials are listed in Table 2.1.

Table 2.1: Band Gap Energies at Room Temperature.

	InP[47]	ZnS[48]	ZnSe[49]	$CH_3NH_3PbI_3$[50]	$CsPbBr_3$[51]	$Cs_2AgBiBr_6$[29]
E_g (eV)	1.35	3.54	2.67	1.6	2.25	2.19

In the case of an excited state, there is a vacant electron state in the VB and a previously empty state in the CB is now occupied by the respective electron. While it is comparably

simple to describe the behavior of a single electron in the CB, it is complicated to do the same for all remaining electrons in the VB. Hence, a new quasiparticle is introduced. Instead of describing all electrons in the VB, the 'movement' of the vacant state named *hole* is analyzed.

As stated before, the minima and maxima of the electronic band structure can be approximated by a parabolic dispersion. In analogy to the parabolic dispersion of a free electron, this leads to the definition of an *effective mass* m^* for electron (e) and hole (h) according to Equation 2.4.

$$\frac{1}{m^*_{\mathrm{e/h}}} = \frac{1}{\hbar^2}\left|\frac{\partial^2 E_{\mathrm{CB/VB}}(\boldsymbol{k})}{\partial \boldsymbol{k}^2}\right| \tag{2.4}$$

Consequently, the effective mass decreases with increasing band curvature. It should be noted that the effective mass may be anisotropic. Moreover, a degenerated band extremum may lead to the existence of heavy and light holes/electrons. Furthermore, spin-orbit coupling may lead to a split-off band at lower energies, especially for semiconductors comprising heavy atoms. The effective mass concept allows for an intuitive description of the behavior of the quasiparticles electron and hole in a solid (*e. g.*, their reaction to an applied electric field). Table 2.2 lists the effective masses for some materials.

Table 2.2: Effective Mass of Charge Carriers. The values are given in units of the free electron mass m_0. If only one hole mass is given, the reference does not distinguish between different hole types. The mass is given for charge carriers located at the respective band maximum. Perovskites exhibit different crystal structures depending on temperature. The values given for $CH_3NH_3PbI_3$ correspond to the low-temperature orthorhombic phase, whereas the ones of $CsPbBr_3$ are given for the high-temperature cubic phase. In the case of $Cs_2AgBiBr_6$, the effective mass is anisotropic (see discussion of Figure 2.5b for details).

	InP[47]	ZnS[52]	ZnSe[49]	$CH_3NH_3PbI_3$[53]	$CsPbBr_3$[29]	$Cs_2AgBiBr_6$[29]
electron	0.079	0.28	0.13	0.22	0.34	0.37
heavy hole	0.45	0.51	0.935	0.23	0.37	0.14
light hole	0.12					
split-off hole	0.21					

It is useful to define a *density of states* $D(E)$ according to Equation 2.5, where V is the volume of the crystal and δ represents the Dirac delta function.

$$D(E) = \frac{1}{V}\sum_{\boldsymbol{k},\nu}\delta\Big(E - E_\nu(\boldsymbol{k})\Big) \tag{2.5}$$

Thus, the quantity $D(E)\mathrm{d}E$ gives the number of all states within an energy interval of width $\mathrm{d}E$. At elevated temperatures T, electrons, being fermions, occupy states according to the Fermi-Dirac statistics $f_{\mathrm{FD}}(E,T)$ given by Equation 2.6, with k_{B} being the Boltzmann constant.

$$f_{\mathrm{FD}}(E,T) = \left[\exp\left(\frac{E - E_{\mathrm{F}}}{k_{\mathrm{B}}T}\right) + 1\right]^{-1} \tag{2.6}$$

At 0 K, this resembles a simple step function, but with increasing temperature, the step 'smears out'. Hence, some of the electrons possess enough thermal energy to overcome the band gap and enter the CB. Now, electrons and holes can contribute to the conductivity of the semiconductor. Nevertheless, the number of thermally excited charge carriers is quite low at room temperature since $k_B T = 25\,\text{meV} \ll E_g$. Accordingly, they play only a minor role for the optical experiments conducted within this thesis and can be neglected.

Actually, while changing temperature, the band gap energy varies as well. In a simple picture, this can be explained as follows. With increasing temperature, the lattice constant typically increases. Thus, the electron wave function overlap of adjacent atoms decreases, which leads to a smaller splitting between bonding and antibonding states. The highest VB of many semiconductors is given by bonding states, whereas the lowest CB corresponds to the respective antibonding states. Hence, the band gap energy decreases with increasing temperature. It should be noted that perovskites are an exception to this typical behavior as will be discussed later. For many semiconductors, the temperature dependence of the band gap can be empirically described by the *Varshni formula* given by Equation 2.7, with α, β, and γ being constants.[54]

$$E_g(T) = E_g(0\,\text{K}) + \frac{\alpha T^2}{\beta + \gamma T} \tag{2.7}$$

Now that the physical foundation of electron and hole states in semiconductors has been laid, their interaction with electromagnetic waves should be outlined.[46] In a semiclassical approach and with the electric dipole approximation, it can be shown that the interaction Hamiltonian is given by $-e\boldsymbol{r}\boldsymbol{E}$, with $\boldsymbol{E}$ being the electromagnetic light field. Based on *Fermi's Golden Rule* given by Equation 2.8, the probability per time, *i. e.*, the rate $k_{i\to f}$, that a photon with energy $E = \hbar\omega$ excites an electron from an initial state i to a final state f leaving a hole behind can be calculated.

$$k_{i\to f} = \frac{2\pi}{\hbar} \sum_{\boldsymbol{k}_i, \boldsymbol{k}_f} \left| \langle f | e\boldsymbol{r}\boldsymbol{E} | i \rangle \right|^2 \cdot \delta\Big(E(\boldsymbol{k}_f) - E(\boldsymbol{k}_i) - \hbar\omega \Big) \tag{2.8}$$

The term $\langle f | e\boldsymbol{r}\boldsymbol{E} | i \rangle$ is the *dipole matrix element*, which is closely related to the *oscillator strength* of the respective optical transition. The Dirac delta function provides not only energy conservation but also leads in combination with the sum to a *joint density of states* $D_j(E)$, which counts the number of possible transitions with a certain energy E. Thus, the joint density of states is proportional to the absorption coefficient.

Besides energy conservation, momentum conservation must be fulfilled during an optical transition. The linear dispersion relation of a photon $E = \hbar\omega(\boldsymbol{k}) = \hbar c|\boldsymbol{k}|$, with c being the speed of light, is much steeper compared to the band structure of a semiconductor. As can be seen in Figure 2.3a, this means that mainly energy is transferred between photon and electron during an optical transition, while the momentum of the electron hardly changes. In reality,

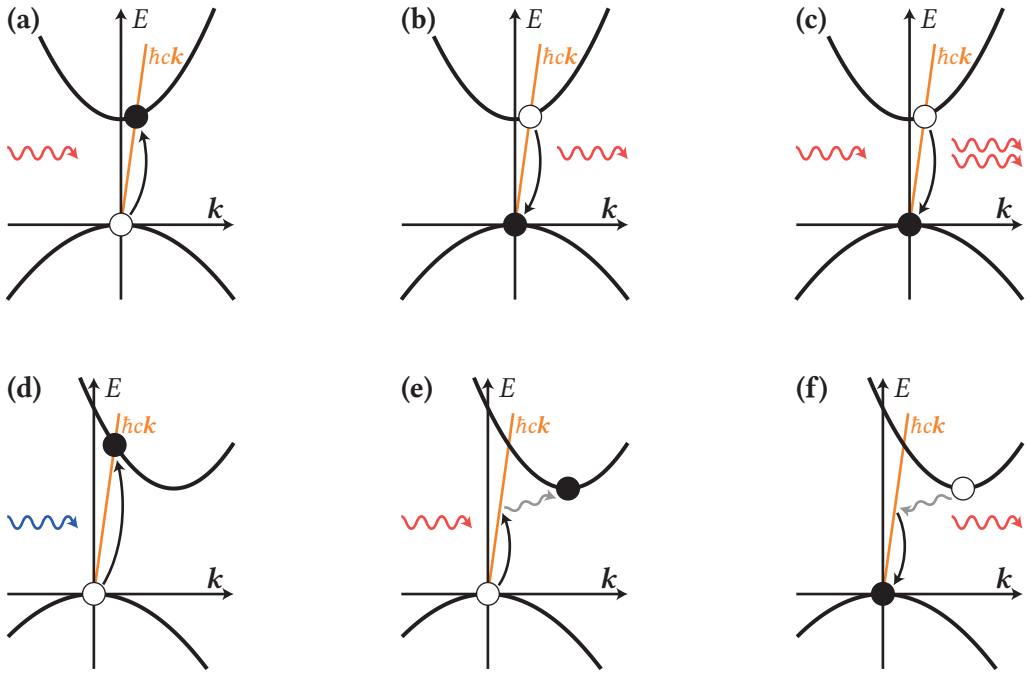

Figure 2.3: Examples for Optical Transitions. (a) By absorption of a photon, an electron is excited into the CB of a direct semiconductor leaving a hole behind (the orange line representing the light dispersion is in reality much steeper). **(b)** An electron in the CB recombines with a hole in the VB after a certain average lifetime, whereby a photon is emitted. **(c)** An incoming photon stimulates the recombination of an excited electron-hole pair. Thus, a second photon is emitted in phase with the first one. **(d)** Purely optical excitation of an electron into the CB of an indirect semiconductor requires a photon with larger energy than the band gap energy. **(e)** The electron can be excited directly to the CBM by involving an additional phonon (gray arrow) in the absorption process. However, such a process is less likely. **(f)** Emission stemming from the indirect band gap transition requires a phonon as well.

the light dispersion is even much steeper than depicted. Therefore, a purely optical transition can be approximately seen as a vertical transition in the energy band structure.

An electron in the CB can also recombine with a hole in the VB after a certain average lifetime, while energy and momentum conservation must be given as well. This process may be radiative and, thus, lead to the emission of a photon as illustrated in Figure 2.3b. However, there are also nonradiative recombination processes. For example, an electron can be trapped in a defect state and subsequently recombine with the hole, while the energy is transferred to phonons. It is also possible that the energy of an electron-hole pair is transferred to a third charge carrier, which then will occupy a higher energetic state (Auger process). Besides spontaneous emission, the possibility of stimulated emission should be noted. This case can be understood as a reversed absorption process where the recombination of an excited electron-hole pair is stimulated by an incident photon of the corresponding energy (see Figure 2.3c). As a result, a second photon is emitted in phase with the stimulating one.

In the case of an indirect semiconductor, the photon energy must be larger than the band gap energy to enable a purely optical excitation of an electron into the CB (see Figure 2.3d).

Nevertheless, an indirect transition can be excited if a phonon is additionally involved in the absorption process as illustrated in Figure 2.3e. However, such a process is less likely. The radiative recombination of electron and hole *via* an indirect transition must involve a phonon as well (Figure 2.3f). Hence, long radiative lifetimes are expected in this case and nonradiative processes may dominate. It is also possible that an electron (or hole) scatters only with a phonon or with another charge carrier. These are typical processes leading to charge carrier relaxation toward the band edge states. This topic will be discussed in Subsection 2.2.3.

As the last part of this section, the recombination dynamics of charge carriers at the lowest excited state should be discussed.[50] The recombination of an electron-hole pair happens with a certain probability per time. Furthermore, the number of excited charge carriers can be described as a density $n_e = n_h = n$, since there are many optically excited electron-hole pairs. Therefore, *rate equations* can be used to describe the corresponding dynamics of the charge carrier density.

In the case of free charge carriers, electron and hole first have to 'find' each other before they can recombine. Accordingly, such a process is named *bimolecular*. The probability that they find each other scales with n for typical charge carrier concentrations. Hence, the change of the density with time $n'(t)$ is given by $-k_2 n(t)^2$, while $k_2 n(t)$ equals the density-dependent recombination rate. The solution to this differential equation is a reciprocal function given by Equation 2.9, with $n(0\,\mathrm{ns}) = n_0$.

$$n_{\mathrm{bimolec.}}(t) = \frac{1}{\frac{1}{n_0} + k_2 t} \tag{2.9}$$

Such a 'finding process' is not always necessary. In the case of trap-mediated recombination, the change of n with time is given by $-k_{\mathrm{trap}} n_{\mathrm{trap}} n(t)$, where n_{trap} is the density of occupied trap states, which is assumed to be constant. Furthermore, if a bound electron-hole pair is already present (see Subsection 2.1.3 for details), the change is simply $-kn(t)$. Such processes are called *monomolecular*. The solution to the general differential equation $n'(t) = -k_1 n(t)$ is a monoexponential function given by Equation 2.10. Here, the recombination rate k_1 is independent of the charge carrier density and can be determined as the inverse of the time at which the normalized $n(t)$ decayed to the 1/e-value. This time is defined as the charge carrier lifetime.

$$n_{\mathrm{monomolec.}}(t) = n_0 \mathrm{e}^{-k_1 t} \tag{2.10}$$

The case of *trimolecular* recombination is given when three particles have to find each other (*e. g.*, Auger process). The corresponding differential equation $n'(t) = -k_3 n(t)^3$ is solved by a more complex function given by Equation 2.11.

$$n_{\text{trimolec.}}(t) = \frac{1}{\sqrt{\frac{1}{n_0^2} + 2k_3 t}} \tag{2.11}$$

Due to the different n-dependency of these processes, they are dominating at different charge carrier concentrations and, thus, in different time regimes. An Auger process requires a high charge carrier density. Accordingly, it may only become significant directly after photoexcitation with a strong laser pulse. If subsequently mono- or bimolecular processes dominate, typically depends on the sample of interest. It is also possible to combine the different processes in one differential equation: $n'(t) = -k_1 n(t) - k_2 n(t)^2 - k_3 n(t)^3$. However, it is not possible to solve this equation analytically.

It should be noted that the considerations above only hold for a two-level system. If an additional energy level is relevant (*e. g.*, an optically dark but energetically close-lying state), the rate equations become more complex. Using further approximations, $n(t)$ can be modeled by a biexponential function in this case.[55,56]

Experimentally, it is is possible to directly probe the charge carrier density using time-resolved photoluminescence (PL) (see Subsection 3.2.3) and differential transmission (DT) spectroscopy (see Subsection 3.2.4). Therefore, it is possible to investigate the underlying physical processes using these methods and comparing the obtained data with the models described above. Care must be taken to differentiate between radiative and nonradiative recombination processes since both lead to a similar change of $n(t)$. How to obtain radiative and nonradiative rates in the case of monomolecular recombination will be explained in Subsection 3.2.3.

The Unique Band Structure of Lead Halide Perovskites

InP can be seen as a typical example of a direct semiconductor. The VBM is given by In_{5s}-P_{3p} and In_{5p}-P_{3p} bonding states. The dominating contribution of p-orbitals causes a degeneracy of the VBM, which results in the formation of a heavy hole (hh) and a light hole (lh) as well as in a split-off hole (soh) due to spin-orbit coupling. The CBM, on the other hand, is given by the respective antibonding states (In_{5s}-P_{3p} and In_{5p}-P_{3p}), while the In_{5s}-orbital is dominating.[57] The resulting band structure is sketched in Figure 2.4a.

The band structure of lead halide perovskites differs significantly from this typical one. It is 'inverted', meaning that the bonding/antibonding and p/s-orbital character of the VB/CB is switched compared to InP. In the case of $CsPbBr_3$, the VBM is given by antibonding states derived from the hybridization of Pb_{6s} and Br_{4p} atomic orbitals, while the s-character is dominating. The empty Pb_{6p}-orbitals couple to each other and the respective bonding states form the CB.[58] Actually, spin-orbit coupling affects this time the CB in contrast to InP. Thus, the CBM is purely given by a split-off electron (soe) dispersion, while the corresponding heavy

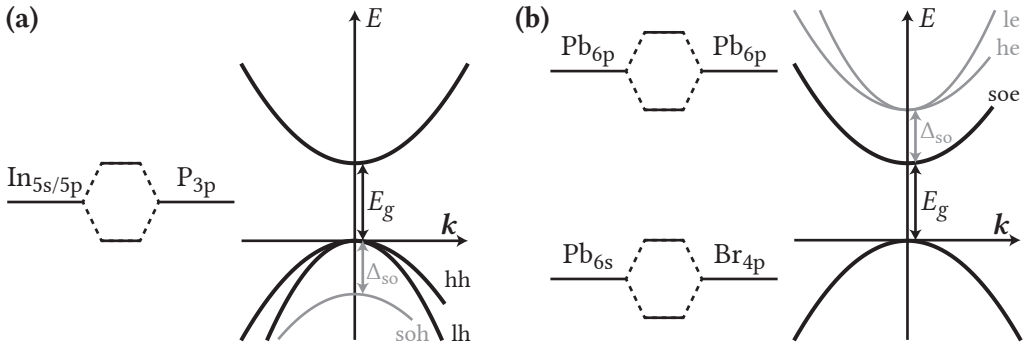

Figure 2.4: Origin of the Perovskite Band Structure. **(a)** Schematic band structure of InP. The antibonding interaction of In and P atomic orbitals gives rise to an s-like state forming the CBM. The respective bonding state is p-like and affected by spin-orbit coupling. Thus, the VBM is given by a hh and a lh dispersion along with a soh band, which is shifted by Δ_{so} to lower energies. **(b)** Schematic band structure of orthorhombic $CsPbBr_3$. Here, VB and CB stem from different orbitals. The bonding interaction of Pb_{6p}-orbitals in combination with spin-orbit coupling results in a single parabola (soe) forming the CBM in k-space. The antibonding interaction of Pb_{6s}- and Br_{4p}-orbitals leads to an s-like state as the VBM. All energy levels are drawn at an arbitrary position and just for illustration purposes.

electron (he) and light electron (le) bands are located at higher energies.[50,59] It should be noted that the Cs atoms, like all typical A-site cations, do not contribute to the band edge states. The resulting band structure is sketched in Figure 2.4b. Interestingly, VBM and CBM are each only given by a single parabolic band, which is unusual compared to most semiconductors. The only remaining degeneracy is due to the electron/hole spin. This might be lifted by the Rashba effect.[60] However, this is still under debate in literature and not discussed within this thesis.[61]

A remarkable consequence of this band structure is the *defect tolerance* of perovskites. This means that typical defect states (*e. g.*, Br dangling bond states as acceptor defects and Pb or Cs dangling bond states as donor defects, with energies close to the respective atomic states) appear either within the VB or CB or as shallow defects close to the band edges.[58] This is one of the reasons why solution-processed perovskites yield such high efficiencies in solar cells despite the presence of many defects.[62]

As mentioned above, VB and CB of perovskites show an opposite (anti-)bonding character compared to most other semiconductors. This results in an unusual temperature dependence of the band gap. With increasing temperature, the antibonding VBM moves to lower energies, whereas the bonding CBM appears at higher energies. Thus, the band gap energy increases with increasing temperature.[63]

The elemental composition of perovskites can be easily varied, as already discussed in Subsection 2.1.1. Depending on the halide content, the band gap energy can be continuously tuned over the complete visible range. The used cation affects not only the band gap energy as well but also changes the position of the VBM/CBM in k-space (Γ point for $CsPbBr_3$, R point for $CH_3NH_3PbI_3$ at room temperature).[50]

What Changes for Lead-Free Double Perovskites?

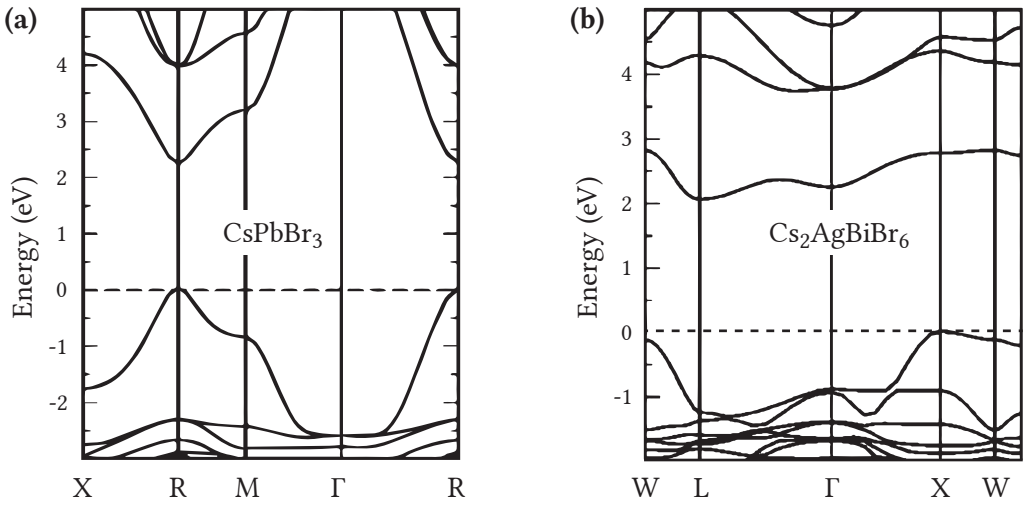

Figure 2.5: Band Structure of $Cs_2AgBiBr_6$ DP. Band structures of cubic **(a)** $CsPbBr_3$ and **(b)** $Cs_2AgBiBr_6$ obtained by DFT calculations. Adapted with permission from Reference 29. Copyright 2016 American Chemical Society.

At room temperature, $CsPbBr_3$ has an orthorhombic crystal structure and both, VBM and CBM, are located at the Γ point as illustrated in Figure 2.4b.[58] $Cs_2AgBiBr_6$, on the other hand, adopts the face-centered cubic (FCC) phase at room temperature. Hence, the band structure of $Cs_2AgBiBr_6$ should be compared to the one of cubic $CsPbBr_3$, which forms at high temperatures ($\geq 130\,^{\circ}C$).[40] As shown in Figure 2.5a, the band structure of cubic $CsPbBr_3$ obtained by density functional theory (DFT) calculations[64,65] looks similar compared to the one of orthorhombic $CsPbBr_3$, but the VBM and the CBM are located at the boundary of the Brillouin zone in the (111) direction. This corresponds to the R point of a primitive cubic cell and the L point of an FCC cell, respectively. In the case of $Cs_2AgBiBr_6$, the CBM is still at the L point. However, the VBM moved away to the X point, which is in the (010) direction. This yields an indirect band gap as shown in Figure 2.5b.

The highest VB mainly originates from Br_{4p} atomic orbitals, while a contribution from Ag_{4d} states leads to several relatively flat bands at lower energies. Those Ag_{4d} states are also partially responsible for the formation of the indirect band gap. The lowest CB is given by antibonding states derived from the hybridization of Ag_{5s} and Bi_{6p} atomic orbitals. It is energetically very narrow and separated from the next higher energetic bands by 1–1.5 eV. Accordingly, the effective mass of electrons is very high, especially around the X point. Only due to the participation of both atoms, Ag and Bi, at least some dispersion is maintained.[29] Interestingly, another bismuth-based perovskite ($Cs_3Bi_2I_9$) also shows a large energetic separation between the dispersion branch forming the CBM and higher energetic states in the CB. In this case, the energetic separation was attributed to the presence of quasi-0D subunits and the formation of minibands.[66]

To estimate the potential of $Cs_2AgBiBr_6$ DPs for optoelectronic applications, a closer look at the effective masses at the band maxima is needed. They directly influence the charge carrier mobility μ, which is given by Equation 2.12, with τ being a phenomenological scattering time of a charge carrier.[46]

$$\mu = \frac{e\tau}{m^*} \tag{2.12}$$

For $CsPbBr_3$, the electron effective mass along the R → X direction is $0.34\,m_e$. This value is comparable to the one of $Cs_2AgBiBr_6$ ($0.37\,m_e$ along the L → W direction). The hole effective mass, on the other hand, is smaller in $Cs_2AgBiBr_6$ compared to $CsPbBr_3$: $0.14\,m_e$ (X → Γ) and $0.37\,m_e$ (R → X), respectively. Nevertheless, the effective mass of a hole at the X point is highly anisotropic and strongly increases in the direction of the W point. In terms of mobility, these values allow only for a qualitative estimation since possible differences in carrier scattering rates are unknown. Nevertheless, the low hole effective mass is encouraging since it may result in a large mobility of holes.[29]

The indirect band gap makes applications, which harness $Cs_2AgBiBr_6$ as a light emitter, challenging. Therefore, this material might be more suitable for solar cells, *e. g.*, in combination with silicon in tandem solar cells. Nevertheless, comprehensive knowledge about the charge carrier dynamics in this material is still missing. However, this is of utmost importance to enable applications based on $Cs_2AgBiBr_6$ DPs. Hence, Chapter 5 will focus on these processes.

2.1.3 What is the Role of Excitons in Perovskites?

Up to now, the Coulomb interaction between electrons and holes was neglected. However, it has important consequences. On the one hand, there is for example the *Sommerfeld enhancement*, which arises from the fact that the presence of an electromagnetic potential enhances the cross section of photon absorption.[67] On the other hand, the attractive force between electron and hole may lead to a bound state named *exciton*.

Electrons and holes in a semiconductor are so far represented by Bloch waves. This means they are not localized but extend over the whole crystal. Nevertheless, by forming a superposition of many Bloch wave functions in close vicinity of a band maximum, it is possible to create a wave packet that is well-localized and can move with time. This localized charge gives rise to a Coulomb potential. Thus, a bound state of electron and hole may have less energy than the band gap energy.[68]

If the bound state extends over many lattice sites, the Coulomb interaction between electron and hole can be seen as equivalent to a hydrogen atom. The only difference is that the electric charge is screened by the permittivity $\epsilon = \epsilon_0\epsilon_r$ of the crystal (ϵ_r corresponds to the respective dielectric constant) and that the electron mass is replaced by the reduced mass μ of the electron-hole pair, which is defined according to Equation 2.13. In this case, a

Wannier-Mott exciton is present and its dispersion relation is given by Equation 2.14.

$$\mu = \left(\frac{1}{m_e^*} + \frac{1}{m_h^*} \right)^{-1} \tag{2.13}$$

$$E_n(\boldsymbol{K}) = E_g - R_y^* \frac{1}{n^2} + \frac{\hbar^2 \boldsymbol{K}^2}{2\left(m_e^* + m_h^*\right)} \tag{2.14}$$

Compared to free charge carriers, the energy of the two-particle state is reduced by the *exciton binding energy* $E_b(n) = R_y^* \frac{1}{n^2}$, with the exciton Rydberg energy R_y^* given by Equation 2.15 and the integer n being the principal quantum number. The center of mass motion yields the typical parabolic dispersion, with $\boldsymbol{K} = \boldsymbol{k}_e + \boldsymbol{k}_h$ being the exciton wave vector.[44]

$$R_y^* = \frac{\mu e^4}{32\pi^2 \epsilon_0^2 \epsilon_r^2 \hbar^2} \tag{2.15}$$

Since an exciton is a combined state of two particles, it cannot be directly visualized in the band structure, which only describes the states of individual charge carriers. Hence, a *two-particle picture* is introduced to visualize excitonic states as displayed in Figure 2.6. In this picture, the energy of an excited electron-hole pair is shown as a function of the exciton wave vector $\boldsymbol{K}$. Besides the bound excitonic levels, there is also a continuum of states that corresponds to free electrons and holes.

If E_b is larger than the thermal energy $k_\mathrm{B}T$, the bound state is typically stable. The size of the exciton ground state is characterized by the exciton Bohr radius a_B^*, which relates to the Bohr radius a_B of the hydrogen atom by Equation 2.16. Table 2.3 lists the values of a_B^* for the materials discussed within this thesis. It should be mentioned that there are also

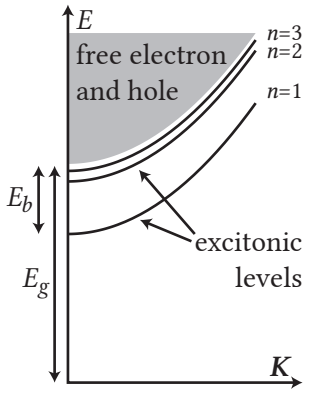

Figure 2.6: The Two-Particle Picture Illustrating Excitons. The energy of an electron-hole pair is visualized as a function of their combined wave vector. A bound state between electron and hole results in discrete excitonic levels below the band gap energy. The center of mass motion leads to a parabolic dispersion. Furthermore, a continuum of states appears above the band gap energy. This corresponds to free electron-hole pairs.

excitons, which are localized to a single unit cell of a crystal. These are named *Frenkel excitons* and typically appear in insulators or organic crystals. However, Frenkel excitons cannot be described in the effective mass approximation introduced above and are not relevant to this thesis.[69]

$$a_B^* = \frac{4\pi\epsilon_0\epsilon_r\hbar^2}{\mu e^2} = \epsilon_r\frac{m_0}{\mu}a_B \tag{2.16}$$

Table 2.3: Exciton Bohr Radius. The value for $Cs_2AgBiBr_6$ was calculated according to Equation 2.16 using the high-frequency dielectric constant $\epsilon_r = \epsilon_\infty = 5.8$[70] and the effective masses given in Table 2.2.

	InP[71]	ZnS[72]	ZnSe[73]	$CH_3NH_3PbI_3$[74]	$CsPbBr_3$[16]	$Cs_2AgBiBr_6$
a_B^* (nm)	9.6	2.5	8	2.2	3.5	3

It should be noted that excitons can localize at point defects, such as vacant crystal sites. This results in *bound excitons*, which have a complex structure of excited states. Since bound excitons have no degree of motion, the corresponding optical transitions may have a very narrow linewidth at low temperatures. Furthermore, the defects potentially cause quick nonradiative recombination. Interestingly, bound excitons can not only be observed in PL spectra but also in absorption spectra. This might be surprising since the number of defects causing bound excitons is typically much less than the number of unit cells, which give rise to normal absorption. Therefore, bound excitons are said to have a *giant oscillator strength*. However, this can be explained by the fact that a bound exciton still covers many unit cells, which increases the cross section.[44,75,76]

For perovskites, it has been proven to be difficult to determine the exciton binding energy. There are many contradictory values reported ranging from a few meV to several tens of meV.[50] According to Equation 2.15, the exciton binding energy depends critically on the dielectric constant. In contrast to many III-V and II-VI semiconductors, the dielectric constant of perovskites depends strongly on frequency. In $CH_3NH_3PbI_3$, for example, the dielectric constant decreases from a static value of roughly 25 to only 5 at high frequencies.[77] It is not obvious which value should be used within the hydrogen-like model.[50] Actually, it is not clear if this model is adequate at all to describe excitons in perovskites. For example, the coupling between optical phonons and charge carriers is completely neglected. While this is justified for many traditional semiconductors, it may have a tremendous impact on the electrical and optical properties of perovskites.[78]

A charge carrier within an at least partially ionic crystal will polarize the lattice by attracting or repulsing atoms depending on the charge. This lattice distortion can be described by a superposition of preferentially longitudinal optical (LO) phonons. Thus, a free charge carrier is accompanied by a 'phonon cloud'. The entity of charge carrier plus phonon cloud is a new quasiparticle named *polaron*. It should be noted that the fundamental Born-Oppenheimer

approximation does not hold anymore if polarons are present since the atomic cores adjust their positions depending on the one of the charge carriers. Nevertheless, the coupling of charge carriers to LO phonons with energy $E_{\mathrm{LO}} = \hbar\omega_{\mathrm{LO}}$ can be characterized by the dimensionless Fröhlich coupling constant $\alpha_{\mathrm{e/h}}$. It is defined by Equation 2.17 with ϵ_s and ϵ_∞ being the static and high-frequency dielectric constants, respectively.

$$\alpha_{\mathrm{e/h}} = \frac{1}{4\pi\epsilon_0}\frac{e^2}{\hbar}\left(\frac{1}{\epsilon_\infty} - \frac{1}{\epsilon_s}\right)\sqrt{\frac{m^*_{\mathrm{e/h}}}{2E_{\mathrm{LO}}}} \tag{2.17}$$

The lattice relaxation leads to a reduction of the band gap by $\alpha_{\mathrm{e/h}}E_{\mathrm{LO}}$ for electrons and holes. Furthermore, the effective mass of a polaron is larger than the mass of a bare charge carrier by a factor of $\left(1 + \frac{\alpha_{\mathrm{e/h}}}{6}\right)$.[44] For most traditional semiconductors, the Fröhlich coupling constant takes small values (*e. g.*, 0.068 for GaAs and 0.15 for InP).[79,80] Hence, polaronic effects are usually neglected. However, for perovskites, the value becomes significant (*e. g.*, 1.72 for $CH_3NH_3PbI_3$) and may explain the contrary reports on the exciton binding energy in literature.[81]

To take polaronic effects into account, the hydrogen-like model can be modified by making the dielectric constant distance-dependent. At a short range, the screening is low, whereas at larger distances the screening is enhanced since the atomic cores adjusted their position due to the electric field.[82] Accordingly, a higher excitonic state ($n > 1$), which has a larger extension compared to the ground state, feels a stronger screening. Thus, its binding energy is further reduced compared to the normal $\frac{1}{n^2}$-dependency of the standard hydrogen-like model. Moreover, the oscillator strength decreases with increasing screening.[78] Therefore, the higher excitonic states are hardly visible in the absorption spectrum of perovskites. Recent investigations have shown that several inconsistencies of former reports on the excitonic properties of perovskites can be solved in this polaron framework. In case of $CH_3NH_3PbI_3$ and $CH_3NH_3PbBr_3$ for example, the exciton binding energy can be determined as 10–15 meV at low temperatures.[83]

The role of excitons within DPs is still under debate. First investigations in 2016 have shown the potential of DPs for optoelectronic applications.[84] However, excitonic effects are rarely discussed despite a strong absorption feature energetically far below the direct band gap. Such a high exciton binding energy is unexpected, given that the effective masses and dielectric constant are comparable to lead halide perovskites. To solve this discrepancy, confinement effects, the possibility of a localized transition, and exciton self-trapping have been proposed.[85,86] Nevertheless, a consistent picture explaining the origin of the strong absorption peak, while being consistent with the charge carrier dynamics, remains elusive. In Section 5.1, it will be shown that this absorption peak can be explained by excitons bound to defects.

2.1.4 The Effect of Confinement

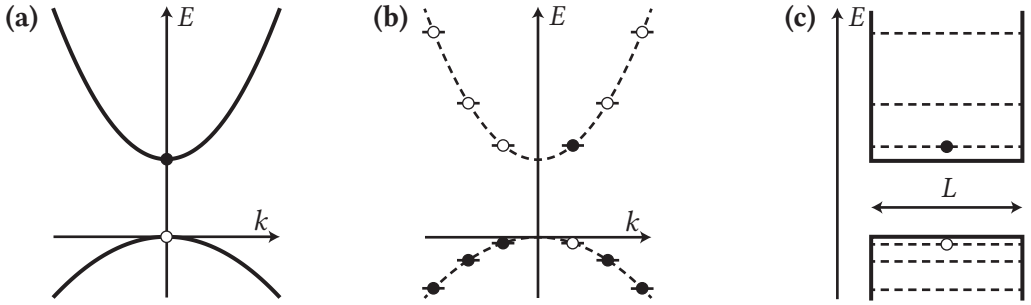

Figure 2.7: Band Structure: Transition to Crystals of Finite Size. **(a)** Normal parabolic dispersion of electron and hole. **(b)** Due to the finite size of the crystal, only certain k-values are allowed. **(c)** In real space, a square well potential can be used to describe the finite crystal size.

Up to now, a semiconductor was treated as a crystal of infinite size. However, the lateral extension has a huge impact on its properties as soon as the size becomes comparable to the natural length scale of an electron or hole, *i. e.*, the respective Bohr radius $\epsilon_r \frac{m_0}{m^*} a_B$. The easiest way to come to this conclusion is to consider the fact that the charge carriers represented by Bloch waves with wavelength $\lambda = 2\pi k^{-1}$ must 'fit' into a crystal with edge length L. This restriction can be written as $L = n\frac{\lambda}{2}$ or $k = n\frac{\pi}{L}$ with an integer n. Accordingly, charge carriers can only occupy states, which are separated by $\frac{\pi}{L}$ in k-space. For an infinite crystal, this becomes the known continuous dispersion as shown in Figure 2.7a. However, discrete states appear for small crystals (Figure 2.7b). This phenomenon is known as the *quantum size effect* and leads to atomic-like optical behavior of NCs as the bulk bands become quantized. Hence, NCs are sometimes referred to as *artificial atoms*.

Typically, the Bohr radius is larger than the atomic spacing (*e. g.*, 5.869 Å for InP).[87] Thus, the effective mass approximation can be used to describe electron and hole from a theory point of view. To this end, charge carriers are placed in a 3D potential well and the corresponding Schrödinger Equation 2.18 needs to be individually solved for electrons and holes (neglecting Coulomb attraction).

$$\left(\frac{\hbar^2}{2m^*}\Delta_{\boldsymbol{r}} + V(\boldsymbol{r})\right)\Psi(\boldsymbol{r}) = E\Psi(\boldsymbol{r}) \tag{2.18}$$

The wave function $\Psi(\boldsymbol{r})$ should be understood as an additional envelope function adjusting the normal Bloch function of a charge carrier in a bulk semiconductor. The obtained energies arising from the confinement are added to the normal band gap energy. Therefore, valence and conduction bands are quantized into a ladder of hole and electron levels, respectively (Figure 2.7c). Importantly, even the ground state has a confinement energy larger than zero. Hence, the observed optical band gap increases and the absorption spectrum shows discrete transitions instead of a continuum.[88] Accordingly, NCs showing such a behavior can be treated as zero-dimensional objects and are termed QDs.

The discrete nature of the energy states has also consequences for the description of the charge carrier dynamics in QDs. The rate equations introduced in Subsection 2.1.2 can be used to describe the dynamics of the charge carrier density in higher-dimensional systems. However, in QDs the concept of a charge carrier density breaks down since a certain state of an individual QD is either occupied or not. Furthermore, relaxation and recombination are random processes and, therefore, do not depend on the average occupation number of a certain state within a QD ensemble. Hence, each QD has to be modeled on its own and only thereafter an ensemble average can be made. To this end, microstates describing all possible occupation scenarios of a single QD can be introduced and these states are linked by equations that take care of possible relaxation and recombination processes. Such an equation system is known as *master equation*. Nevertheless, it was shown that rate equations still yield comparable results even for higher energetic states. Thus, the dynamics of the average occupation numbers of the lowest energetic electron and hole states can be described by exponential functions as a good approximation.[89–91]

It should be noted that excitonic as well as confinement effects modify the normal charge carrier states. Accordingly, the question arises how to combine them. Typically, the model describing the energetically stronger effect is used, while the other one is considered using perturbation theory. In small QDs, for example, the confinement energy is much larger than the exciton binding energy in a bulk crystal. Thus, electron and hole adopt specific states and the formation of an exciton is not possible. The Coulomb attraction between electron and hole may then be treated using perturbation theory leading to a small correction. This leads to the more sophisticated model of *pair states*.[92]

Besides spatial confinement, a variation in the dielectric environment may strongly affect the energy of electronic states. For example, solving the exciton model in two dimensions (representing NCs in form of platelets) yields a four times higher exciton binding energy. However, experimental observations demonstrate that the binding energy increases even more reaching several hundreds of meV.[93] This can be attributed to the low dielectric constant of the medium surrounding the NCs (*e. g.*, a solvent), since the Coulomb attraction between electron and hole is hardly screened.[23]

2.2 Quantum Dots in the Strong Confinement Regime

2.2.1 Discrete Energy States Instead of a Dispersion

In the following section, the quantum states of electron and hole in a spherical QD will be derived within the effective mass approximation.[94] This model will be extended in Section 4.1 to describe core/shell QDs as well. The relevant Schrödinger Equation 2.18 was already introduced in the previous section. In order to model a QD with radius R_{QD}, a spherical potential $V(r)$ according to Equation 2.19 is used.

$$V(\boldsymbol{r}) = V(r,\theta,\phi) = V(r) = \begin{cases} 0 & \text{for } r \leq R_{\mathrm{QD}} \\ \infty & \text{for } R_{\mathrm{QD}} < r \end{cases} \tag{2.19}$$

The spherical symmetry suggests treating the Schrödinger equation in spherical coordinates, which yields Equation 2.20.

$$\frac{\hbar^2}{2m^*}\left(\frac{1}{r^2}\partial_r\left(r^2\partial_r\right) + \frac{1}{r^2\sin\theta}\partial_\theta\left(\sin\theta\partial_\theta\right) + \frac{1}{r^2\sin^2\theta}\partial_\phi^2\right)\Psi(r,\theta,\phi) + \\ + V(r)\,\Psi(r,\theta,\phi) = E\,\Psi(r,\theta,\phi) \tag{2.20}$$

By separating the radial and angular parts of the wave function according to $\Psi(r,\theta,\phi) = R(r)\,\Theta(\theta)\,\Phi(\phi)$, three individual differential equations can be obtained, where m^2 and $l(l+1)$ are constants of separation.

$$\partial_\phi^2\Phi(\phi) = -m^2\Phi(\phi) \tag{2.21}$$

$$\sin\theta\,\partial_\theta\left[\sin\theta\,\partial_\theta\,\Theta(\theta)\right] + l(l+1)\sin^2\theta\,\Theta(\theta) = m^2\,\Theta(\theta) \tag{2.22}$$

$$\partial_r\left[r^2\partial_r R(r)\right] - \frac{2m^*}{\hbar^2}r^2\left[V(r) - E\right]R(r) = l(l+1)\,R(r) \tag{2.23}$$

Equation 2.21 is solved by $\Phi_m(\phi) = (2\pi)^{1/2}\mathrm{e}^{-im\phi}$. The solution to Equation 2.22 is proportional to the *associated Legendre function* $P_l^m(\cos\theta)$, while $0 \leq |m| \leq l$. $P_l^m(x)$ derives from the l^{th} *Legendre polynomial* $P_l(x)$, defined by Equation 2.24, according to $P_l^m(x) = (1-x^2)^{m/2}(\partial_x)^m P_l(x)$.

$$P_l(x) = \frac{1}{2^l\,l!}\partial_x^l\left(x^2-1\right)^l \tag{2.24}$$

The product $\Theta(\theta)\,\Phi(\phi)$ equals the *spherical harmonics* $Y_l^m(\theta,\phi)$ and is given by Equation 2.25.

$$Y_l^m(\theta,\phi) = (-1)^m\sqrt{\frac{2l+1}{4\pi}\frac{(l-m)!}{(l+m)!}}P_l^m(\cos\theta)\mathrm{e}^{im\phi} \tag{2.25}$$

The radial part, given by Equation 2.23, can be rewritten as Equation 2.26.

$$r^2R''(r) + 2rR'(r) + \left(\frac{2m^*r^2}{\hbar^2}\big(E - V(r)\big) - l(l+1)\right)R(r) = 0 \tag{2.26}$$

Since the potential is infinite outside of the QD, $R(r) = 0$ for $r > R_{\mathrm{QD}}$. Within the QD, the differential equation is solved by *spherical Bessel functions* $j_l(kr)$ and $y_l(kr)$ defined by Equation 2.27 with $k = \sqrt{\frac{2m^*E}{\hbar^2}}$.

$$j_l(x) = (-x)^l\left(\frac{1}{x}\partial_x\right)^l\frac{\sin x}{x} \tag{2.27a}$$

$$y_l(x) = -(-x)^l\left(\frac{1}{x}\partial_x\right)^l\frac{\cos x}{x} \tag{2.27b}$$

However, $y_l(kr)$ diverges at the origin, which is physically impossible. Hence, it is not a solution of interest. Focusing on $j_l(kr)$ and using the boundary condition that $R(R_{\mathrm{QD}}) = 0$, only certain wave vectors k_{nl} or energy values E_{nl} are possible and given by Equation 2.28 with β_{nl} being the n^{th} zero of the l^{th} spherical Bessel function $j_l(x)$ given by Table 2.4. Interestingly, the energies are still identical to the kinetic energy of a free particle, except that the wave vector is quantized.

$$E_{nl} = \frac{\hbar^2k_{nl}^2}{2m^*} = \frac{\hbar^2}{2m^*R_{\mathrm{QD}}^2}\beta_{nl}^2 \tag{2.28}$$

Table 2.4: Zeros β_{nl} of the Spherical Bessel Function $j_l(x)$.

β_{nl}	$l=0$	1	2	3	4	5
$n=1$	π	4.49	5.76	6.99	8.18	9.36
2	2π	7.73	9.10	10.42	11.70	12.97
3	3π	10.90	12.32	13.70	15.04	16.35

The quantum states are labeled in analogy to atomic physics as nl_X, with X being the underlying charge carrier type: e, hh, lh, or soh. The quantum number l (angular momentum) is encoded using the typical letters $s = 0$, $p = 1$, $d = 2$, and so on. The electron ground state, for example, is accordingly named $1s_{\mathrm{e}}$. Figure 2.8a shows the corresponding energy levels of electron and hole along with some radial wave functions. An InP QD with 1.7 nm radius and the effective masses of charge carriers given by Table 2.2 were used for the calculation. The energy levels related to the soh were shifted by the splitting energy $\Delta_{\mathrm{so}} = 0.108\,\mathrm{eV}$[47] arising from the spin-orbit coupling. The density of hole states is much higher compared to the one of electron states. This is caused by the presence of hh, lh, and soh and the higher hole mass in general. The full envelope wave function is given by $\Psi_{nlm}(r,\theta,\phi) \propto Y_l^m(\theta,\phi)\,j_l(k_{nl}r)$ and illustrated in Figure 2.8b.

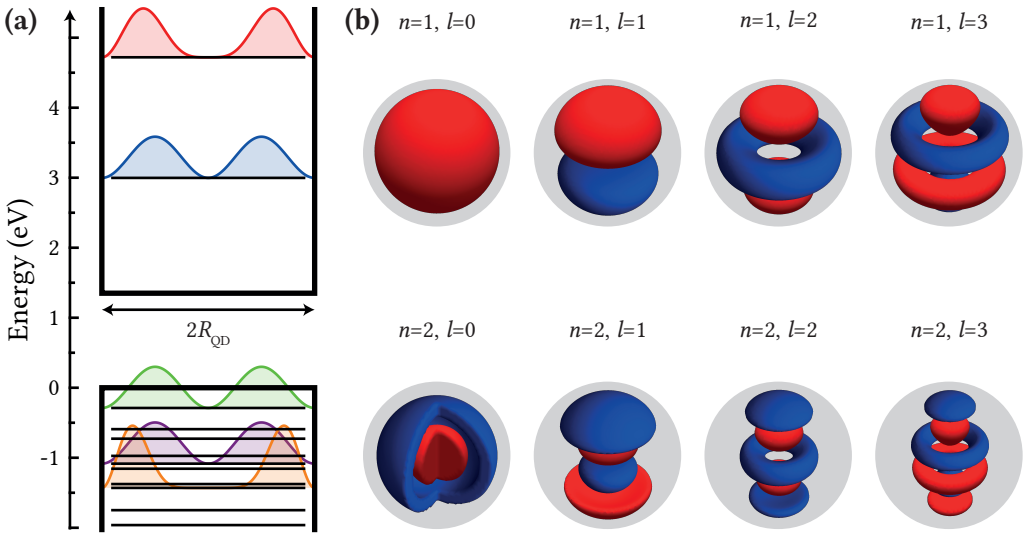

Figure 2.8: Spherical QD: Energies and Wave Functions. (a) Energy levels of electron and hole. The radial part of some wave functions ($r^2|R(r)|^2$) is shown for illustration (blue: $1s_e$, red: $1p_e$, green: $1s_{hh}$, purple: $1s_{lh}$, orange: $1d_{hh}$). **(b)** The full wave function $\Psi_{nl0}(r,\theta,\phi)$ of the first few quantum states. If the wave function exceeds a certain threshold to the positive or negative, it is shown by the red and blue regions, respectively.

Optically active transitions between these quantum states can be identified when analyzing the dipole matrix element (see Equation 2.8).[95] The wave function including the Bloch part at the band maximum reads $\Psi_{nlm}(r,\theta,\phi)\Phi_v(\boldsymbol{r})$. The dipole matrix element for a transition between VB and CB is thus given by Equation 2.29 and can be separated in the integration of the fast oscillating Bloch part and the integration of the envelope part.

$$\langle \Psi_{nlm}(\boldsymbol{r})\Phi_{CB}(\boldsymbol{r})\,|\,e\boldsymbol{r}\boldsymbol{E}\,|\,\Psi_{n'l'm'}(\boldsymbol{r})\Phi_{VB}(\boldsymbol{r})\rangle = \langle \Phi_{CB}(\boldsymbol{r})\,|\,e\boldsymbol{r}\boldsymbol{E}\,|\,\Phi_{VB}(\boldsymbol{r})\rangle\,\langle \Psi_{nlm}(\boldsymbol{r})|\Psi_{n'l'm'}(\boldsymbol{r})\rangle \quad (2.29)$$

The Bloch part equals the dipole matrix element of a bulk crystal (*e. g.*, it takes care that angular momentum is conserved during absorption or emission of a photon). The part with the envelope function, however, introduces new selection rules for possible interband transitions. Since the spherical harmonics are orthogonal to each other, only transitions between states, where l and m are not changing, show an overlap integral different from zero. Furthermore, it turns out that the radial wave functions are orthogonal as well: $\int j_l(k_{nl}r)\,j_l(k_{n'l}r)\,r^2dr \propto \delta_{nn'}$. Therefore, the only possible transitions are between electron and hole states with equal quantum numbers, while their oscillator strength is proportional to $(2l+1)$ due to the degeneracy with respect to the quantum number m.[92]

In reality, the electronic structure of QDs is more complex showing a fine structure of the energy levels (*e. g.*, mixing of hole bands, Coulomb interaction, non-spherical shape, splitting of states). Interestingly, it turns out that the lowest energetic transition is optically dark.[92] However, the energetic separation to the lowest bright transition is less than the thermal energy at room temperature. Hence, this energy level fine structure may be neglected at room

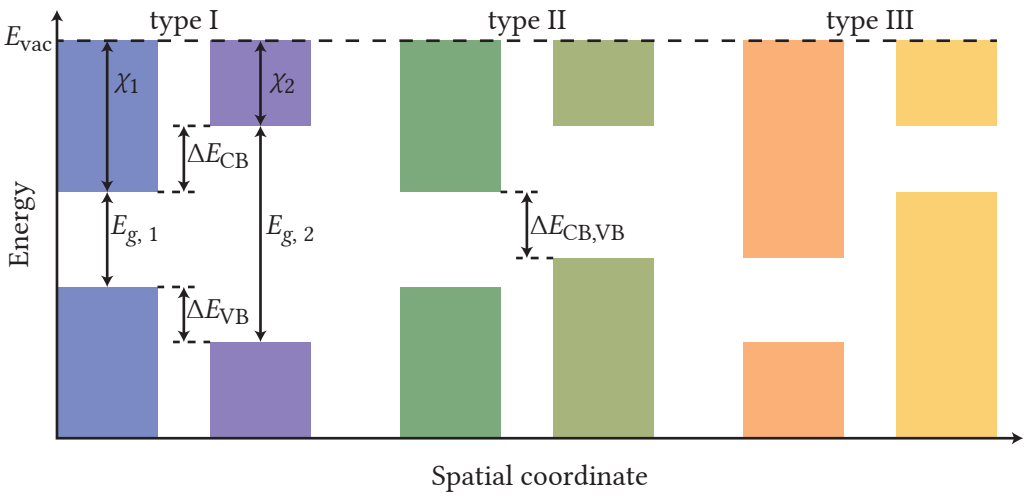

Figure 2.9: Semiconductor Heterostructures. Energy band alignment of type I, II, and III semiconductor heterostructures. Figure is adapted from Reference 96.

temperature. Since all measurements discussed within the scope of this thesis are conducted at room temperature, the model introduced above is already sufficient to interpret the results of the presented experiments.

When discussing core/shell QDs, the interface between semiconductors becomes important. Using the simplest model, it is sufficient to align the energy bands of both materials with respect to the vacuum energy level E_{vac} according to the respective electron affinity χ.[97] This leads to a step-like potential for electrons and holes. As shown in Figure 2.9, it can be distinguished between three different types of heterostructures depending on the band alignment. In the case of type I, the energetically higher VBM and the lower CBM are both in the same material showing the smaller band gap of the two semiconductors. Thus, electron and hole will localize there. This is the case for the core/shell QDs investigated in Chapter 4. A type II heterostructure shows a staggered lineup of the band maxima. Accordingly, electrons and holes will localize in different materials. Finally, a type III structure is present if the band gaps of both semiconductors do not overlap.[96]

2.2.2 Broadening of Optical Transitions

According to Equation 2.28, the confinement energy E_{nl} depends on R_{QD}^{-2} and therefore is strongly affected by the QD size. Since QDs obtained by colloidal chemistry show a certain size distribution, the transition energies observed in an ensemble are inhomogeneously broadened. Nevertheless, this is not the only reason for a spectral width of optical transitions due to the presence of fundamental homogeneous broadening mechanisms.

The emission from a single emitter at 0 K would show a full width at half maximum (FWHM) of $\Delta E = \gamma$. This is caused by the finite lifetime τ of the excited state due to Heisenberg's uncertainty principle. In the case of monoexponential recombination, the line shape would be Lorentzian according to a Fourier transformation.[98]

At elevated temperatures, additional broadening mechanisms affect the line shape. The most dominant one is due to charge carrier scattering with optical and acoustic phonons. The resulting FWHM $\Gamma(T)$ can be modeled according to Equation 2.30.[99]

$$\Gamma(T) = \Gamma_{\mathrm{inhom}} + \gamma + \sigma_{ac} T + \frac{\Gamma_{op}}{\exp\left(\frac{\hbar\omega_{op}}{k_{\mathrm{B}} T}\right) - 1} \tag{2.30}$$

In the case of acoustic phonons, the broadening is proportional to the temperature with a coupling constant σ_{ac}. The contribution from optical phonons is proportional to the population of an average phonon state with energy $\hbar\omega_{op}$ according to the Bose-Einstein statistics, with Γ_{op} being the coupling strength. It should be noted that in the case of large charge carrier densities, carrier-carrier scattering can influence the FWHM as well. However, this is not relevant for the experiments discussed within this thesis as the charge carrier density was kept low.

The aforementioned sample inhomogeneity (*e. g.*, varying crystal size, defects) results in a temperature-independent contribution Γ_{inhom}. This inhomogeneous broadening leads to a Gaussian line shape. The convolution of Gaussian and Lorentzian profiles results in a so-called Voigt function. However, this function depends on many free parameters, which is why a simple Gaussian function (see Equation 2.31) is used in most cases to analyze the FWHM of a certain transition.[98]

$$I_{\mathrm{Gaussian}}(E) = I_0 \exp\left[-4\ln(2)\left(\frac{E - E_0}{\Gamma}\right)^2\right] \tag{2.31}$$

To distinguish between the inhomogeneous and homogeneous broadening, either optical experiments on the single-particle level, which will be presented in Subsection 3.2.2, or four-wave mixing spectroscopy may be used.[100] The latter technique measures the loss of coherence (dephasing time T_2) of oscillating dipoles, which are initially excited in phase by the light field. According to Equation 2.32, the dephasing time can be related to the lifetime of

the excited state T_1 and scattering times T_i^*, which can be associated with various scattering mechanisms (*e. g.*, carrier-phonon and carrier-carrier scattering).

$$\frac{1}{T_2} = \frac{1}{2T_1} + \sum_i \frac{1}{T_i^*} \tag{2.32}$$

Since T_2 is inverse proportional to the homogeneous line width $\Gamma_{\text{hom}} = \frac{2\hbar}{T_2}$ of the respective optical transition, it is possible to measure Γ_{hom} without influences of the sample inhomogeneity.[92]

Typically, dephasing becomes faster if a charge carrier is excited with excess energy. This is caused by the increasing density of states within a band at higher energy, which facilitates scattering processes. Hence, homogeneous broadening exceeds inhomogeneous broadening for higher energetic transitions, whereas the inhomogeneous one mainly influences transitions in the vicinity of the optical band gap.

2.2.3 The Charge Carrier Relaxation Problem

The dephasing process mentioned in the previous section is only the first stage after photoexcitation of a semiconductor with an ultrashort laser pulse (typically $\leq$ 100 fs).[101] The excitation process generates a coherent population of free electron-hole pairs or excitons, depending on the chosen excitation energy. Due to scattering processes, the phase relation between the individual excited charge carriers becomes lost over time. This coherent regime typically has a maximum duration of a few hundred femtoseconds and can be seen as the time until the first collision.

Subsequently, scattering processes first lead to a thermal equilibrium among the charge carriers before a thermal equilibrium with the lattice is reached. Such processes typically take place on a time scale reaching several picoseconds and involve carrier-carrier as well as carrier-phonon scattering processes. During this stage, intervalley scattering may take place in indirect semiconductors. Finally, when all charge carriers relaxed to the vicinity of the band edge, recombination becomes the dominating process, which takes place on a time scale reaching several nanoseconds in the case of the materials investigated within this thesis.

There are multiple processes leading to carrier-phonon scattering.[46,92] On the one hand, there is the aforementioned polar Fröhlich coupling between electrons/holes and optical phonons. In this case, the electric field created by the vibrating ionic nuclei couples to the Coulomb field of the electron-hole pair. On the other hand, charge carriers may couple to acoustic phonons *via* a deformation potential or piezoelectric interactions. The deformation potential enables coupling to longitudinal acoustic (LA) phonons. The variations of the ion bond length induce a modulation of the band gap and of the exciton energy. Furthermore, the polar coupling arising from piezoelectric interactions leads to charge carrier scattering with

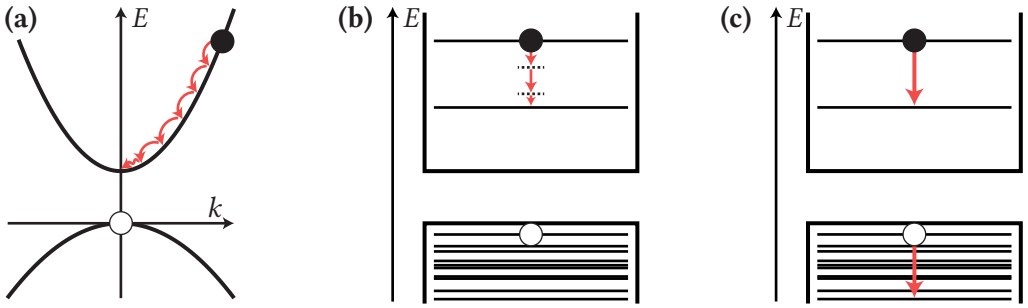

Figure 2.10: The Phonon Bottleneck. (a) In bulk semiconductors, charge carriers may relax *via* individual scattering events with phonons. For simplicity, only the relaxation of an electron is shown. **(b)** In QDs, charge carriers (especially electrons) have to overcome large energetic gaps in order to relax. Accordingly, an unlikely multi-phonon process is required, which leads to the so-called phonon bottleneck. Please note that the phonon energy associated with the arrows is exaggerated for better visualization. Hence, even more phonons need to be involved in reality. **(c)** This issue can be circumvented by an Auger-like process. The electron transfers its excess energy to the hole, which then will occupy a higher energetic state. The subsequent hole relaxation is less affected by the phonon bottleneck due to the higher density of available hole states.

transverse acoustic (TA) phonons. For all of these processes, it is possible that a phonon is either absorbed or emitted, while the temperature influences the probability for the respective event.

All of these processes must conserve energy and momentum. As can be seen in Figure 2.10a, there are always suitable phonons for scattering events available due to the continuous dispersion of energy bands in bulk semiconductors. These are predominantly LO phonons. Only if the excess energy of charge carriers with respect to the band edge is smaller than the LO phonon energy, scattering must involve acoustic phonons. In the case of QDs, momentum conservation is relaxed due to the quantum confinement. However, the large energetic separation between individual states leads to a problem. As sketched in Figure 2.10b, the energy of an individual phonon is not sufficient to overcome this energetic gap. Accordingly, a less likely multiple phonon emission process is required. Moreover, the number of final states, where the charge carrier may scatter to, is dramatically reduced in QDs compared to bulk semiconductors. Hence, scattering rates are expected to decrease according to Fermi's Golden Rule. This issue is known as the *phonon bottleneck*.

Interestingly, early QD structures showed only a low emission efficiency, which was attributed to the phonon bottleneck.[102] However, it was demonstrated that Auger-like processes circumvent the phonon bottleneck and, thus, lead to a quick charge carrier relaxation.[103] As shown in Figure 2.10c, the excess energy can be transferred between electron and hole. While this process may happen in both directions, it is much more likely that the electron transfers its excess energy to the hole. The reason is that the energetically close-lying hole levels offer more final states for the scattering event. Thus, the hole subsequently occupies an

even higher energetic state. Fortunately, the density of hole sates is large enough to allow for a quick subsequent hole relaxation.

In Chapter 4, the charge carrier relaxation in InP-based QDs will be analyzed in detail. So far, mainly cadmium-based QDs were subject of research. Hence, there are open questions if InP-based QDs show similar or different behavior. A focus will be on the exact relaxation times depending on the excess energy of charge carriers. Moreover, the charge carrier relaxation from a QD shell into the core will be analyzed. This topic is hardly discussed in the literature so far. Finally, the question if all charge carriers successfully relax to the band edge states will be investigated. The obtained insights may help to improve the efficiency of future LEDs harnessing such QDs as direct emitters.

Furthermore, the new field of DPs is the topic of Chapter 5. Especially the relaxation dynamics of charge carriers will be discussed. Since these NCs have lateral dimensions larger than the exciton Bohr radius, quantum confinement effects are not dominating, but the band structure plays an important role for the interpretation of the experimental observations. Interestingly, the indirect band structure gives rise to strongly varying effective masses of charge carriers during the relaxation process. In combination with the investigation of the intriguing excitonic properties of DPs, a consistent picture of the excited state dynamics will be derived.

3

Materials and Experimental Methods

Optical spectroscopy enables the investigation of physical processes within semiconductors that were discussed in the previous chapter. The following chapter will introduce several of the corresponding techniques. Steady-state spectroscopy reveals not only the basic optical properties but can also be used to characterize more complex processes like the relaxation efficiency of charge carriers. In the case of an ensemble of semiconductor NCs, inhomogeneous broadening of optical spectra is an undesired issue. Therefore, spectroscopic methods can be applied on the single-particle level in order to circumvent this problem. Finally, time-resolved PL and DT spectroscopy will be introduced as they allow to characterize the charge carrier dynamics. But first, the chemical syntheses of the used semiconductor NCs will be highlighted.

3.1 Synthesis of Semiconductor Quantum Dots

The ELQ-LED project and its objectives were already mentioned in Chapter 1. Our project partners, *Merck* and *Fraunhofer IAP*, synthesized the QDs used in my research. The synthesis of DP NCs, on the other hand, was done by my colleague Dr. Amrita Dey. Accordingly, this section will only give a brief description of the hot-injection method, which is used for the synthesis of both nanomaterials. Further details on the underlying chemical processes can be found in the referenced literature.

3.1.1 The Principle of the Hot-Injection Method

The experimental realization of the *hot-injection method* dates back to 1993 when Murray, Norris, and Bawendi introduced a high-temperature synthesis in organic solvents for cadmium chalcogenide NCs.[104] It appears that temporal separation of nucleation and growth processes is crucial for obtaining particles with a narrow size distribution.[105] To achieve this, one can distinguish between two strategies: heterogeneous and homogeneous nucleation. An example of the first one is *seeded growth*. Here, seed particles are formed and isolated. In a second step, they are injected in a solution containing suitable precursors and ligands, which allow for controlled growth. Homogeneous nucleation, on the other hand, limits itself. In this case, the precursors irreversibly form monomers, which subsequently aggregate in an equilibrium process to NCs of defined size. Accordingly, this method falls in the category of a *one-pot synthesis*.[106]

Hot-injection is to be understood literally. The reagents are rapidly injected in a hot solvent, whereby the concentration rises above a critical threshold leading to a nucleation burst. But this is quickly quenched as the supersaturation vanishes and the temperature decreases since the injected solution is cold. Now, the reaction medium can be heated again in a way that the remaining precursors lead to a controlled growth of the nuclei. Typical processes taking place at this stage are *size focusing*[107] and *Ostwald ripening*,[108] which narrow or broaden the size distribution, respectively. If desired, the obtained NCs can be transferred in a second reaction medium, where a shell material can be grown.[109] During all those steps ligand molecules are present in the solution. Specific head groups (*e. g.*, thiols or amines) allow them to attach at (preferential) sites of the NCs. This stabilizes the colloidal dispersion and can also give rise to a nonspherical geometry of the NCs.[106]

It should be mentioned that there exists also a second popular procedure for NC synthesis, the *heat-up method*. In this case, the reaction mixture is prepared at low temperature and then heated up until controlled nucleation starts. This slower process can lead to higher reproducibility, however, a challenging fine-tuning of the precursor reactivity is needed to prevent a broad size distribution of the final product.[110,111]

In the following two sections, this theoretical overview will be illustrated by the synthesis of $Cs_2AgBiBr_6$ DP NCs and InP-based core/shell QDs.

3.1.2 $Cs_2AgBiBr_6$ Double Perovskite Nanocrystals

The synthesis of $Cs_2AgBiBr_6$ DP NCs follows a slightly modified procedure reported by Creutz *et al.*[112] and is illustrated in Figure 3.1. First, 0.7 mmol cesium acetate (Cs(OAc), 99.9 % metal basis, *Alfa Aesar*), 0.5 mmol anhydrous silver acetate (Ag(OAc), 99 %, *Alfa Aesar*), and 0.5 mmol bismuth acetate ($Bi(OAc)_3$, 99.99 % trace metal basis, *Sigma-Aldrich*) are dissolved in a solution comprising 1.5 mL oleic acid (90 %, *Alfa Aesar*), 0.37 mL oleylamine (70 %, *Sigma-*

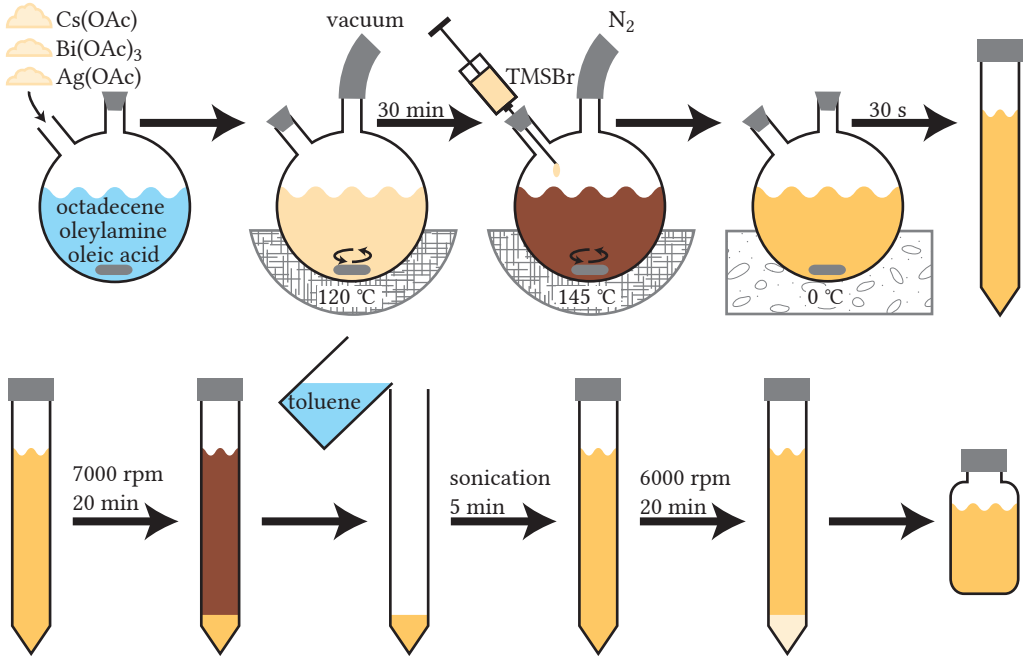

Figure 3.1: Synthesis of $Cs_2AgBiBr_6$ DP NCs. The hot-injection procedure is depicted in the top row, whereas the bottom row shows the purification process.

Aldrich), and 6 mL 1-octadecene (90 %, *Sigma-Aldrich*). Using a Schlenk line, this mixture is heated to 120 °C under vacuum for 30 min to remove residual gases and water from the precursors. During this drying process, the color of the reaction mixture changes from pale yellow to dark brown. Subsequently, a nitrogen atmosphere is applied and the solution temperature is increased to 145 °C. Now, 0.2 mL trimethylsilyl bromide (TMSBr, 97 %, *Sigma-Aldrich*) are swiftly injected under vigorous stirring, which induces a color change to yellow. Finally, the reaction is immediately quenched by applying an ice water bath for 30 s.

The obtained NCs must be purified by centrifugation to remove excess ligands and remaining precursors. In the first step, the reacted solution is centrifuged at 7000 rpm for 20 min. The obtained yellow sediments contain the majority of the NCs and the remaining precursors, whereas the excess ligands along with small seeds stay in the supernatant. Accordingly, the supernatant is discarded and the sediment is then redispersed in 10 mL toluene (99.5 %, *Carl Roth*) by sonication for 5 min. In the last step, the dispersion is centrifuged again at 6000 rpm for 20 min. Now, only the remaining precursors form the sediment, whereas the NCs stay in dispersion due to the different solvent. Thus, the supernatant is collected as the final product containing $Cs_2AgBiBr_6$ DP NCs.

The morphology of these NCs was characterized by a transmission electron microscope (TEM) operating at an accelerating voltage of 80–100 kV (JEOL JEM-1011). As can be seen in Figure 3.2a, the NCs are cubic in shape and of uniform size. An average edge length of (8.9 ± 0.2) nm was determined by analyzing 100 particles (see Figure 3.2b).

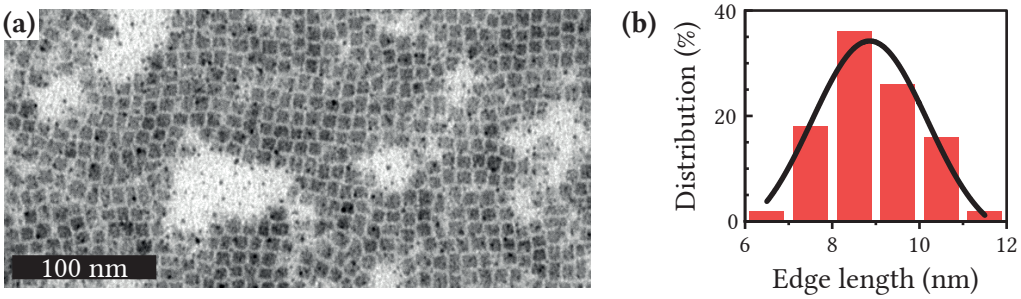

Figure 3.2: Morphology of $Cs_2AgBiBr_6$ DP NCs. (a) TEM image. **(b)** Edge length distribution (red bars) obtained from the analysis of 100 particles. A Gaussian fit (black line) gives (8.9 ± 0.2) nm for the average edge length.

3.1.3 InP Quantum Dots

Starting from the first report of colloidal InP QDs back in 1996,[113] the synthesis procedure constantly improved yielding NCs of increasing quality. Besides the classical *core-only* QDs, it is possible to grow a shell around the core leading to a *core/shell* structure. The shell serves the purpose of passivating surface defects and, thus, reducing nonradiative recombination channels. Especially ZnS and ZnSe have proven to be suitable shell materials although their lattice parameters are not perfectly matching with the core (see Table 3.1). This discrepancy can be reduced by creating a *gradient shell* or adding *multiple shells* of different materials.[106,114,115]

Table 3.1: Lattice Parameters.

	InP[87]	ZnS[116]	ZnSe[117]
a (Å)	5.869	5.4159	5.67

There are two established but very different chemical syntheses of InP QDs reported in the literature.[118] The first one uses tris(trimethylsilyl)phosphine as the phosphorus precursor and probably yields QDs with the best quality. However, the precursor is costly and a pyrophoric substance, which produces the highly toxic gas PH_3 in contact with air. Nevertheless, the *Samsung Advanced Institute of Technology* recently made great progress with this synthesis and the subsequent fabrication of LEDs. A detailed description of their synthesis protocol can be found in the corresponding publication.[119]

The *Fraunhofer IAP* used the same phosphorus precursor and they obtained InPZnS hybrid core-only QDs by modifying a previously reported synthesis protocol.[120] Their approach will be outlined in the following as an example of a QD synthesis. Indium acetate (1 mmol) and zinc octanoate (2 mmol) were heated to 150 °C under vacuum and stirred for 30 min. Then, the temperature was reduced to 120 °C under argon flow and 1-dodecanethiol (0.5 mmol), as the sulfur precursor, and acetic acid were injected. The mixture was stirred for 5 min before the temperature was reduced to 100 °C and tris(trimethylsilyl)phosphine (1 mmol) was rapidly injected. Then, the mixture was stirred for 10 min, heated to 300 °C, and kept at that

temperature for up to 30 min. Finally, the reaction mixture was cooled to room temperature and purified by centrifugation using different solvents (acetone and hexane). Interestingly, the amount of used acetic acid (0–5.25 mmol) allows tuning the mean diameter of the obtained QDs from 2.2 nm to 4.8 nm, which results in a varying strength of quantum confinement. Consequently, the emission wavelength varies as well (535–628 nm). Further details on these QDs can be found in the corresponding publication.[121]

The second synthesis variant is based on the less dangerous tris(dimethylamino)phosphine as the phosphorus precursor.[122] Interestingly, the QD growth process during this synthesis differs from the typical one. Here, nucleation and growth are not temporally separated but continuous nucleation takes place. A narrow final size distribution is achieved since smaller particles grow faster than larger ones.[123]

In the scope of my thesis, the focus lies on InP/ZnS and InP/ZnSe core/shell QDs, which were used as received from *Merck*. Since there are some patents pending, it is unfortunately not possible to report their exact synthesis procedure. The corresponding TEM images are shown in Figure 3.3 and the respective dimensions are listed in Table 3.2 as determined by *Merck*.

Table 3.2: QD Dimensions.

core		shell	
material	diameter	material	diameter
InP	3.4 nm	ZnS	8–10 nm
InP	3.0 nm	ZnSe	10.5–11 nm

The QDs are dispersed in toluene and the received solutions are highly concentrated having a mass content of 50 mg mL^{-1}, while the mass ratio between QDs and (excess) ligands is roughly 2:1. The mass of a single QD is $1.6 \cdot 10^{-21}$ kg, given the density of InP (4.79 g cm^{-3}) and ZnS (4.1 g cm^{-3}) and assuming a spherical shape. Hence, the density of QDs in the highly concentrated dispersion is approximately $2.2 \cdot 10^{16}$ cm^3.

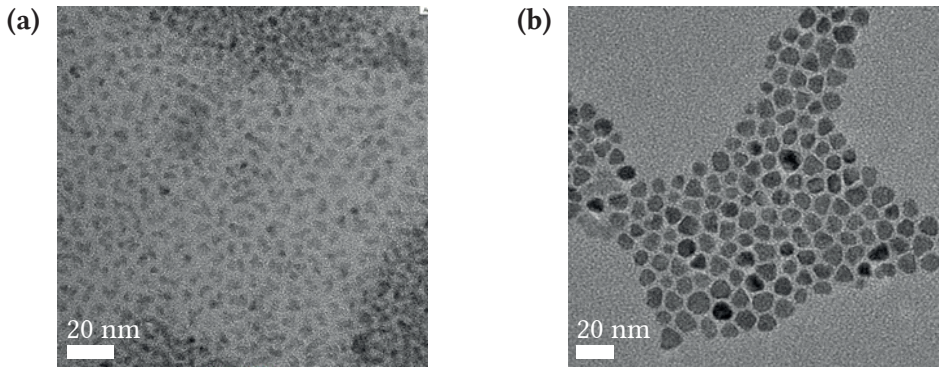

Figure 3.3: Morphology of InP-Based QDs. TEM images of **(a)** InP/ZnS and **(b)** InP/ZnSe QDs, respectively.

While the experimental setups are explained in the following sections, the general sample preparation is already described here. For measurements in solution, approximately 10 µL of the QD dispersion and 5–10 µL ligand (hexanethiol, 95 %, *Sigma-Aldrich*) are added to a cuvette containing toluene (2 mm or 1 cm optical path length and 3 mL or 600 µL volume, respectively). This yields an optical density of approximately 0.1 at the absorption onset. The additional ligands enhance the stability of the QDs, presumably by preventing detaching of the original ligands (see Section 4.1 for details).

By calculating the volume that is illuminated by a laser, it is possible to estimate the average number of generated electron-hole pairs on a single QD for a given laser pulse energy. In case of the DT measurements that will be discussed in Chapter 4, the excitation volume is 0.7 mm^3 and the maximum concentration of QDs is $8.5 \cdot 10^{14}$ cm^{-3}. Therefore, $6 \cdot 10^{11}$ QDs are located within the excitation volume. The highest used pulse energy of 255 nJ at 525 nm corresponds to $6.7 \cdot 10^{11}$ photons per pulse. In this case, 50 % of the photons are absorbed, which means that on average 0.6 electron-hole pairs are excited on a single QD. Assuming a Poisson distribution, more than one electron-hole pair is generated on only 10 % of the QDs. Since this scenario constitutes the most extreme case, effects due to multiple electron-hole pairs should be negligible for the experiments discussed in Chapter 4.

For the investigation of single QDs, the original dispersion was diluted by a factor of 10^6 in toluene (containing an equivalent concentration of hexanethiol as described above). The diluted dispersion was immediately spin-coated (100 µL, 5000 rpm) onto a 1 cm^2 silicon wafer in a static way. Thus, individual QDs are separated by a few microns and can be distinguished by optical microscopy.

3.2 Optical Spectroscopy of Semiconductor Quantum Dots

A powerful technique for the investigation of NCs is optical spectroscopy since it can yield a coherent picture of the photophysical processes taking place. Already simple experiments like steady-state absorption or PL spectroscopy can give a hint to more complex processes. Those can be studied in detail by employing time-resolved methods (*e. g.*, DT spectroscopy). A typical challenge in the investigation of NCs is their size distribution, which can lead to an inhomogeneous broadening of optical spectra. This issue can be circumvented by employing measurement techniques on the single-particle level. Combining all these methods, it is possible to specify the advantages and challenges which need to be taken under consideration for the development of applications based on a new material.

In the following section, the spectroscopic methods used in my research will be presented. The focus lies more on specific topics, which I encountered during my time as a PhD student, and less on general experimental details since these are well described in the literature.[124] It will be shown how to get an impression of the charge carrier relaxation efficiency using only steady-state spectroscopic methods. As mentioned before, it is desirable to investigate individual NCs. To this end, a µ-PL setup can be used, which was modified and improved during my research. Here, I want to give a guide to the key points, which need to be considered for building such an instrument. While this setup can resolve the PL decay, a modern streak camera enables the investigation of the PL signal with a much better time resolution of 1 ps. During my research, such a device was installed and I will give an overview of the working principle. Finally, DT spectroscopy is introduced as another important technique to study charge carrier relaxation processes in detail. In literature, the signals obtained from DT spectroscopy are presented following two different conventions: either as a change in transmission or in absorbance. As this may lead to confusion, I will compare both conventions.

3.2.1 A Simple Measure for the Charge Carrier Relaxation Efficiency

One of the most important photophysical characteristics of a material is the linear absorption spectrum. It must be distinguished between the absorption taking values between 0 % and 100 % and the absorbance, which is also called optical density (OD). When light with an intensity $I_0(\lambda)$ transmits through a sample, the intensity decreases to $I(\lambda)$ (see Figure 3.4a). This is caused by absorption $A(\lambda)$, reflection $R(\lambda)$, and scattering $S(\lambda)$. In many cases, it is justified to neglect the contributions from reflection and scattering compared to the dominating absorption. If not otherwise stated, this is always the case in the following. Thus, the transmission $T(\lambda)$ can be calculated according to the Lambert-Beer law, which states that the transmitted light intensity decreases exponentially with the sample thickness d (Equation 3.1). Therefore, the absorption coefficient $\alpha(\lambda)$ is the characteristic physical quantity. Please note

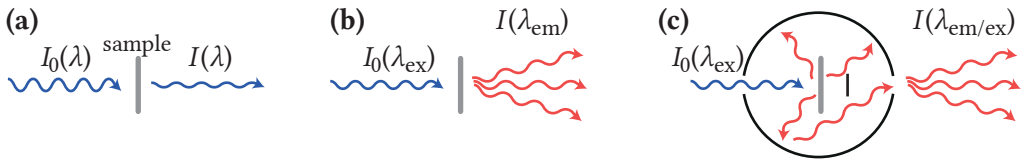

Figure 3.4: Measurement Scheme for Absorption, PL, and QY Determination. (a) Light with intensity $I_0(\lambda)$ is partially absorbed by a sample resulting in a transmitted intensity $I(\lambda)$. **(b)** A sample is excited by light with intensity $I_0(\lambda_{ex})$ yielding PL with a spectrum $I(\lambda_{em})$. The light can be emitted in all directions (not shown for simplicity). **(c)** A (blank) sample located in an integrating sphere is excited by light with intensity $I_0(\lambda_{ex})$. Emission and transmitted/scattered excitation light (not depicted) are reflected multiple times within the sphere until they leave it through a small hole. The direct way to the exit is blocked. The QY can be calculated using the intensity spectra $I(\lambda_{em/ex})$ obtained from the real and blank samples.

that the wavelength dependence of all quantities is not stated in the following equations to improve readability.

$$\frac{I}{I_0} = 1 - A - R - S \approx 1 - A = T = \mathrm{e}^{-\alpha d} \tag{3.1}$$

As can be seen in Figure 3.5, typical spectra do not show the absorption coefficient itself but $\mathrm{OD}(\lambda)$, which differs only by a constant factor of $d\log_{10}(\mathrm{e})$ as can be seen in Equation 3.2. Unfortunately, the definition of $\mathrm{OD}(\lambda)$ uses a basis 10 instead of the basis e, which appears in the Lambert-Beer law. Therefore, a decadic absorption coefficient $\alpha^*(\lambda)$ can be introduced to simplify the formulas. It should be noted that if a colloidal sample is in dispersion the absorption coefficient depends linearly on the sample concentration, with the molar attenuation coefficient being the corresponding proportionality constant. The absorption spectra presented in this thesis are measured using either a *Cary 60 UV-VIS* or a *Cary 5000 UV-Vis-NIR* spectrometer by *Agilent Technologies*.

$$\mathrm{OD} = -\log_{10}(T) \underset{\text{Equation 3.1}}{=} -\log_{10}\left(\mathrm{e}^{-\alpha d}\right) = \alpha d \log_{10}(\mathrm{e}) = \alpha^* d \tag{3.2}$$

If a sample absorbs a photon, an excited state is created, which can lead to emission as illustrated in Figure 3.4b. This phenomenon is called PL. Typically, a sample is excited with monochromatic light $I_0\,(\lambda_{ex})$ coming from a laser or the combination of a lamp with a monochromator. The emitted light $I(\lambda_{em})$ can be directed through another monochromator onto a photodetector. Thus, the PL intensity can be measured as a function of the emission wavelength (an example is shown by the black line in Figure 3.5). The ensemble PL spectra presented in this thesis were acquired using a *Fluorolog 3* by *Horiba* with a xenon lamp being the excitation source. Sometimes it is useful to analyze the PL intensity as a function of emission energy E_{em}. In this case, the reciprocal relation of wavelength and energy ($E = {}^{hc}/_{\lambda}$) must be considered by adjusting the intensity values according to Equation 3.3, with h and c being the Planck constant and speed of light, respectively.[125]

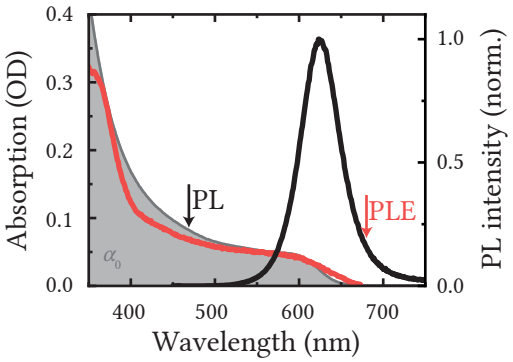

Figure 3.5: Linear Optical Spectroscopy. A typical absorption spectrum of InP/ZnS QDs dispersed in toluene is given by the gray area. The black line corresponds to the PL spectrum (λ_{ex} = 470 nm), whereas the red line shows a PLE spectrum (λ_{em} = 680 nm).

$$I(E_{em}) = I(\lambda_{em})\,\frac{hc}{E_{em}^2} \tag{3.3}$$

This measuring scheme can be reversed leading to photoluminescence excitation (PLE) spectroscopy. In this case, the PL intensity at a fixed emission wavelength is determined as a function of the excitation wavelength. Obviously, the emitted intensity $I(\lambda_{em})$ needs to be normalized by the (varying) excitation intensity $I_0\,(\lambda_{ex})$. A typical PLE spectrum is shown in Figure 3.5 by the red line. Interestingly, this method can quantify to which extend an absorbing state leads to emission.[46] To this end, it is needed to make a connection between OD and PLE spectra. Since the light intensity is proportional to the number of photons $I \propto N$, the Lambert-Beer law can be used to calculate the number of absorbed photons $N_{abs}\,(\lambda_{ex})$ according to Equation 3.4, while $\alpha(\lambda_{ex})\,d$ must be small enough to justify a Taylor expansion.

$$\frac{N}{N_0} = \frac{I}{I_0} = e^{-\alpha d} \overset{\text{Taylor, } \alpha d \ll 1}{\approx} 1 - \alpha d \quad \text{leads to} \quad N_{abs} = N_0 - N \approx \alpha d N_0 = \text{OD}\frac{N_0}{\log_{10}(e)} \tag{3.4}$$

Equation 3.1 — Equation 3.2

Every absorbed photon creates an electron-hole pair, which relaxes with a certain efficiency $\eta_{relax}\,(\lambda_{ex})$ to the emitting state. Now, the charge carriers can recombine radiatively with a probability η_{recomb}. Assuming that charge carriers 'forget' how they were excited during the relaxation processes, η_{recomb} is independent of the excitation wavelength. Taken all together, this means that the PLE intensity $I_{PLE}\,(\lambda_{ex})$, which is proportional to the number of emitted photons N_{em}, is given by Equation 3.5.

$$I_{PLE} \propto N_{em} = N_{abs} \cdot \eta_{relax} \cdot \eta_{recomb} = \text{OD} \cdot \eta_{relax} \cdot \eta_{recomb} \cdot \frac{N_0}{\log_{10}(e)} \tag{3.5}$$

Equation 3.4

This means that the charge carrier relaxation efficiency can be deduced from the difference between OD and PLE spectra. As can be seen in Figure 3.5, such a deviation is present in case of the investigated InP/ZnS QDs, which points to a reducing charge carrier relaxation efficiency with increasing excitation energy. This will be analyzed in detail in Section 4.4. It should be noted that care must be taken when comparing absorption and PLE spectra because PLE spectra might be influenced by effects, which are not considered above. These include varying reflection of the excitation light at the sample surface depending on wavelength, diffusion processes within the sample, and reabsorption of emitted light.[44] Furthermore, PLE spectroscopy can probe a subset of the sample if inhomogeneous broadening plays a role. For example, the PLE spectrum can be determined at an emission wavelength corresponding to the high energetic side of the PL peak. Thus, only a subset of the sample emitting at this wavelength is probed (*e. g.*, smaller crystals having a larger optical band gap due to enhanced quantum confinement). This technique is known as size-selective PLE.[46,126]

The product $\eta_{\mathrm{relax}}(\lambda_{\mathrm{ex}}) \cdot \eta_{\mathrm{recomb}}$ is known as quantum yield (QY) and equals the ratio of emitted to absorbed photons as can be seen from Equation 3.5. It is one of the most important quantities characterizing the radiative efficiency of materials. The QY as a function of excitation wavelength can be used as well to investigate the charge carrier relaxation efficiency. However, determining the QY is not trivial. One needs a trick to obtain values, which are equally proportional to the number of absorbed and emitted photons, while at the same time scattering, reflection, and the angular dependence of the emission need to be taken into account. There exist two popular methods for the QY determination: a comparative procedure based on dye molecules and a direct method using an integrating sphere, which is explained in the following paragraph.[127]

As illustrated by Figure 3.4c, a sample is placed and excited in the center of a sphere. The sample may be dispersed in a solvent or placed on a transparent substrate. It is even possible to investigate a powders if it is encapsulated between two glass plates.[128] The direct path from the excitation spot to the exit of the sphere is blocked. Accordingly, all reflected, scattered, and emitted light will be equally reflected multiple times within the sphere before it leaves. To prevent reflection losses, the interior is coated with a barium sulfate-based material (*e. g.*, Spectralon®) leading to efficient diffuse reflection. Thus, the signal measured at the exit will be proportional to all photons, which were present within the sphere, independent of the angular dependence of emission or scattering processes. However, it is crucial to correct for the wavelength-dependent reflectivity and detector sensitivity. Furthermore, the absorption of the sample at the excitation wavelength should be smaller than 20 % (OD $\leq$ 0.1) to minimize disturbing influences (*e. g.*, reabsorption), which would bias the following measurements. Now, one can acquire spectra showing either the emission signal EM_{sample} or the remaining intensity of the excitation light EX_{sample} under equal experimental conditions. Together with data obtained from a blank sample (*e. g.*, clean substrate or cuvette with pure solvent), the QY

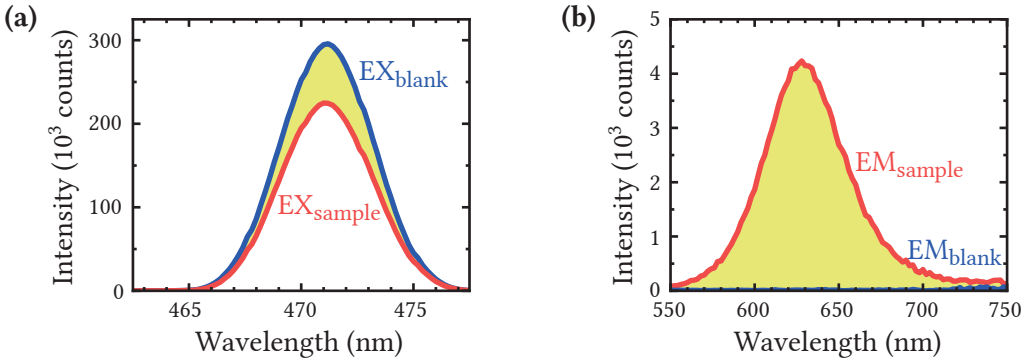

Figure 3.6: Determination of the PL QY. InP/ZnS QDs were dispersed in 3 mL toluene at a concentration corresponding to OD(470 nm) = 0.08. A small amount of ligands (10 µL hexanethiol) was added to improve the colloidal stability. A 3 mL-cuvette filled with the same amounts of toluene and hexanethiol served as the blank sample. The excitation wavelength is set to 470 nm. **(a)** Measurements covering the wavelength range of the excitation light. The highlighted area is proportional to the number of absorbed photons. **(b)** Measurements covering the wavelength range of the PL. The highlighted area is proportional to the number of emitted photons. As expected, the signal from the blank sample is close to zero since the solvent is not showing any PL. Now, the QY is given by the ratio of both highlighted areas, which is in this case 75 %.

can be calculated. A typical measurement is shown in Figure 3.6. The difference signal of the remaining excitation light is proportional to the absorbed photons, whereas the intensity change within the PL region is proportional to the emitted photons. Accordingly, the QY can be calculated using Equation 3.6.

$$\mathrm{QY} = \frac{N_{\mathrm{em}}}{N_{\mathrm{abs}}} = \frac{EM_{\mathrm{sample}} - EM_{\mathrm{blank}}}{EX_{\mathrm{blank}} - EX_{\mathrm{sample}}} \tag{3.6}$$

It should be noted that only an apparent PL QY can be measured when dealing with an ensemble of many NCs. The reason is that it is impossible to distinguish between the following two scenarios. On the one hand, a QY of 50 % will be measured if all individual NCs have this QY. On the other hand, a similar value would be obtained if half of the ensemble shows a perfect QY of 100 %, whereas the other half remains completely dark due to nonradiative recombination. Therefore, experiments on the single-particle level as presented in the next section are an important tool to characterize the heterogeneity of an NC ensemble.

3.2.2 How to Build a Setup for Single-Particle Spectroscopy

As mention in Subsection 3.1.1, colloidal NCs show a size distribution. This might affect the optical transition energies (*e. g.*, due to varying strength of quantum confinement) and, thus, lead to a broadening of optical ensemble spectra. A possible way to circumvent this issue is to apply the spectroscopic methods previously described on the single-particle level. In this section, a setup called *μ-PL* will be introduced. The name refers to its spatial resolution in the micrometer range. The focus of this section lies on the experimental realization of such a setup providing the key points, which need to be considered during construction.[129] The setup is capable of recording PL-images close to the optical diffraction limit, measuring PL and PLE spectra of individual emitters, and obtaining corresponding PL decay traces with nanosecond resolution. Furthermore, the sample is located in a cryostat allowing to work at temperatures down to 4 K. A Hanbury Brown–Twiss intensity interferometer can be used to characterize the photon statistics of the emitted light (*e. g.*, photon antibunching). It should be mentioned that this setup can easily be modified using polarizers and wave plates in order to characterize the PL anisotropy as well.[130,131] However, this is not discussed in this section since such measurements are not presented in this thesis.

To meet the requirements for the desired spectroscopic methods, a versatile excitation light source is needed. It should provide short laser pulses in a broad wavelength range at a variable repetition rate. The white-light laser (WLL) *SuperK EXTREME EXR-20* by *NKT Photonics* is a suitable option. It is based on a pulsed ytterbium-doped fiber laser (1064 nm), which is coupled into a photonic crystal fiber leading to supercontinuum generation (470–2400 nm), whereby the fundamental Gaussian mode is maintained.[132] An acousto-optic tunable filter within the *SuperK SELECT* unit can be used to choose a single wavelength as the final laser output (visible: 470–670 nm, infrared (IR): 690–1100 nm). Wavelengths in the ultraviolet (UV) region (330–480 nm) can be obtained using the *SuperK EXTEND-UV* unit, which is based on second-harmonic generation (SHG). Unfortunately, the beam quality slightly deteriorates in this case (*e. g.*, non-Gaussian beam profile). A built-in pulse picker can adjust the repetition rate within 0.15–78 MHz, which is favorable for time-correlated single photon counting (TCSPC) measurements as described later. The final laser pulses have a duration of 20–100 ps and a spectral width smaller than 12 nm, depending on the chosen wavelength. The laser power varies between 2–20 mW in the visible and IR range, while it decreases to only 30–130 μW in the UV. This laser system is shown as the first part of Figure 3.7, which illustrates the complete μ-PL setup.

The laser beam is directed through a movable neutral density gradient filter and on a photodiode (PD) power sensor, which can be flipped out of the beam path. Both components can be remotely controlled using a computer. This enables a quick and reproducible power adjustment during a measurement series. The laser beam is reflected from a dichroic mirror

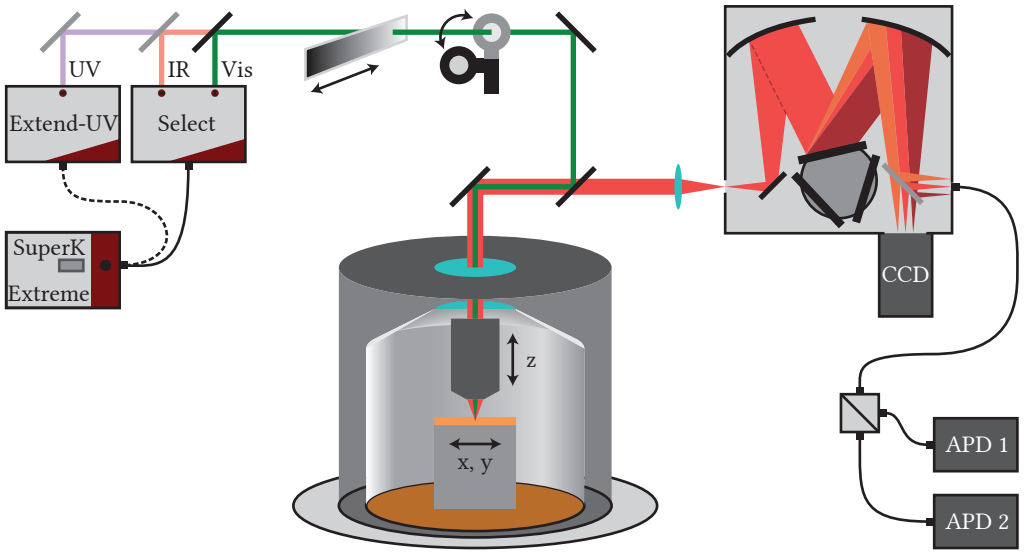

Figure 3.7: The µ-PL Setup. A *SuperK EXTREME EXR-20* WLL in combination with an *Extend-UV* or *Select* unit provides laser pulses with adjustable wavelength (330–1100 nm). The laser power can be controlled using a neutral density gradient filter on a linear stage in combination with a PD power sensor on a motorized flip mount. The laser beam is directed to an *attoDRY800* cryostat. After entering the vacuum chamber and the cold shield, the laser beam is focused on a diffraction-limited spot using an objective on a vertical linear stage. The sample is located on an x,y-stage, thus, allowing for a full 3D positioning control. The emission is collected by the same objective, separated from the laser beam using a dichroic mirror, and focused on the entrance slit of an *Acton SpectraPro 2300* imaging spectrograph. It is possible to record a PL image of the sample or to measure the PL spectrum of an individual spot using a CCD. A flip mirror can direct the beam to a second exit, which is connected to two APDs *via* a beamsplitter. Based on a TCSPC technique, it is possible to record the PL decay and the second order intensity correlation function of individual emitters.

and send to the head of an *attoDRY800* cryostat (*Attocube*), which controls the temperature of a sample in the range of 3.8–320 K. The sample is mounted on a stack of two linear translation stages, which enable a lateral movement of 6 mm with an accuracy of 200 nm. To ensure a good thermal coupling, silicon or sapphire substrates should be used and fixed to the cryostat using either vacuum grease (*Apiezon N*) or conductive silver lacquer (*Busch*). The laser beam is focused on the sample using an objective (*LT-APO/532-RAMAN/0.82*) by *Attocube* with an apochromatic range of 520–695 nm. Notably, it is located within the cryostat and mounted on a similar vertical translation stage. This enables a close working distance of 0.64 mm, which is needed to reach a large numerical aperture (NA) of 0.82. According to Equation 3.7, the NA characterizes a solid angle ϕ up to which emitted light can be captured, with n being the refractive index of the medium between objective and sample. Here, the medium is either air or vacuum, which results in $n = 1$. Obviously, it is advantageous to collect as many emitted photons as possible when looking at single NCs.

$$\mathrm{NA} = n \sin \phi \tag{3.7}$$

The collimated PL beam is separated from the scattered excitation light by the previously mentioned dichroic mirror and focused on the entrance slit of an *Acton SpectraPro 2300* spectrograph (*Princeton Instruments*). Details on the imaging process will follow later. Since the parabolic mirrors of the spectrograph are silver-coated, light must have a wavelength larger than ~400 nm to be efficiently transmitted. As shown in Figure 3.7, a turret can be used to change between different gratings and mirrors. If a mirror is chosen, the open entrance slit (12 mm × 8 mm) is simply imaged with a one-to-one ratio on the exit port, where a charge-coupled device (CCD) is mounted (*Pixis400*, *Princeton Instruments*). Thus, a PL image of the sample can be recorded. In order to adjust the size of the excited area, a lens with (long) focal length may be put in the excitation beam path in front of the dichroic mirror. Depending on the specific lens, this will slightly (de-)focus the excitation spot, while the sample stays in the focal plane of the objective.

In principle, such an imaging process can be done with a grating at zero order as well. However, the reflection efficiency is much worse compared to a real mirror. On the other hand, if a grating is chosen instead of the mirror, the light can be diffracted according to its wavelength and a PL spectrum can be recorded. In this case, the entrance slit should be closed to 10–100 µm. Accordingly, only emission from a small region on the substrate can enter the spectrograph. While the horizontal component of the detector now relates to wavelength, the vertical component still contains the lateral information. This means that if two emitters are by chance located on a vertical axis next to each other, it is possible to record the PL spectra of both emitters at the same time. It should be mentioned that the wavelength resolution $\Delta\lambda$ scales in theory with the number of illuminated grating lines N according to Equation 3.8, with m being the diffraction order. Accordingly, the focusing lens in front of the spectrograph should be chosen in such a way that the grating is fully illuminated. To meet this requirement, the lens must match the f-number ($f/\#$) of the spectrograph. It is given by Equation 3.9 for a lens with focal length f and diameter D of the collimated light beam.

$$\frac{\lambda}{\Delta\lambda} = m \cdot N \tag{3.8}$$

$$f/\# = \frac{f}{D} \tag{3.9}$$

The spectrograph has an f-number of 3.9 and the clear aperture of the objective is 4.7 mm. Accordingly, the lens should have a focal length of only ~2 cm. This would have two experimental disadvantages. Not only the alignment of such a lens is very sensitive, but also the optical aberrations become significant. Furthermore, the focal length of the lens directly affects the magnification of the objective-lens system and, thus, the spatial resolution.

Figure 3.8 illustrates the objective-lens system, while a simple lens replaces the objective to simplify the picture. As an example, two point-like particles emitting light at 600 nm are

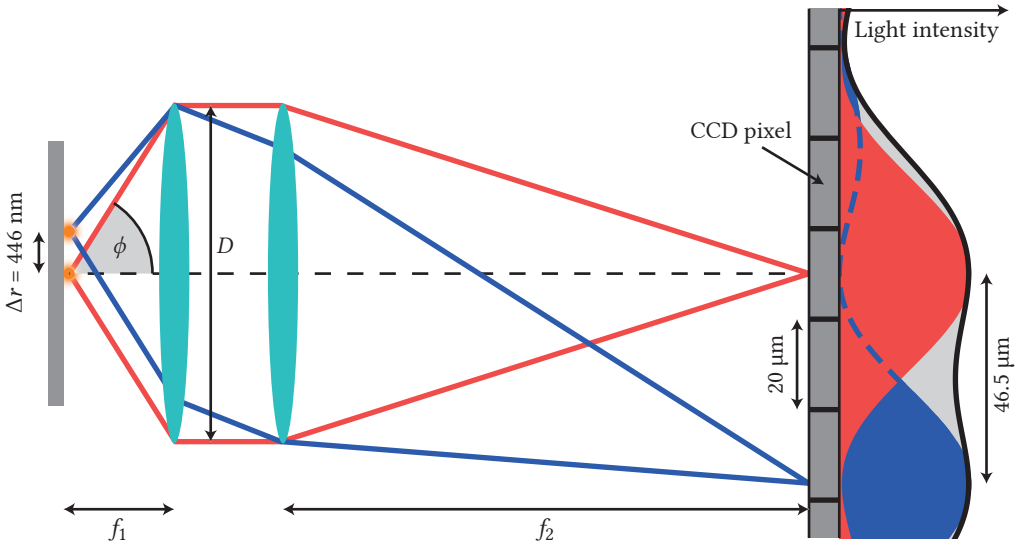

Figure 3.8: Spatial Resolution of the µ-PL Setup. Two point-like particles, separated by $\Delta r = 446$ nm on a substrate, emit light at 600 nm. A fraction of the emission is collimated by the first lens with focal length $f_1 = 2.88$ mm and diameter D. The light beam is then focused on a CCD with 20 µm-pixels by the second lens ($f_2 = 300$ mm). The red and blue lines indicating the light beams are calculated using ray transfer matrix analysis. The optical diffraction limit states that the light is not focused to a point-like spot, but an extended Airy disk. The light intensity profile of both particles is shown by the black line. According to the magnification of the lens system, the two intensity maxima are separated by 46.5 µm. This scenario exactly matches the Rayleigh criterion.

located on a substrate. The first emitter lies on the optical axis, whereas the second particle is slightly shifted. While the particles emit light in all directions, only a fraction is collected by the first lens according to its NA. The advantage of an objective compared to a simple lens is that it allows for a large NA combined with a small diameter of the collimated PL. Furthermore, it produces less optical aberrations since it consists of multiple lenses, which try to correct them. As a consequence, the working distance is typically shorter than the focal length. The collimated PL beam is then focused by the second lens on the spectrograph entrance slit, which is imaged one-to-one on the exit port. Accordingly, the CCD is directly shown in the focal plane and records the light intensity. Due to the optical diffraction limit, the point-like particles are imaged as extended diffraction patterns called *Airy disks*. The angular spatial resolution Δr of such a system is given by Equation 3.10 reflecting the Rayleigh criterion, which states that two point-like emitters are just distinguishable if the intensity maximum of the one diffraction pattern coincides with the first minimum of the other.

$$\Delta r = \frac{1.22 \cdot \lambda}{2 \cdot \mathrm{NA}} \tag{3.10}$$

The above-mentioned objective has an NA of 0.82 leading to a minimum resolvable distance of 446 nm at a wavelength of $\lambda = 600$ nm. Given this theoretical resolution limit, a closer look at the detection of the intensity profile makes sense. To apply the Rayleigh

criterion in practice, the intensity profile must be recorded with sufficient spatial resolution. Since a pixel of the CCD is a square of 20 µm edge length, the magnification of the diffraction pattern is crucial. A rule of thumb states that Δr should be magnified to cover 5–10 pixels to resolve the diffraction pattern with sufficient resolution. This would require a magnification of 220–440. The magnification of the objective-lens system is given by the focal length ratio of lens to objective. Thus, the focal length of the lens should be 65–130 cm, given an objective focal length of 2.88 mm.

The required focal length of at least 60 cm needed for optimal spatial resolution is in clear contradiction with the 2 cm needed for optimal wavelength resolution. As a trade-off, a lens with 30 cm focal length is used, which leads to a magnification of 104. Relating this to the size of the open slit, the field of view is 115 µm × 77 µm. While most of the laser is focused onto a small spot (~1 μm^2), there is still enough light intensity at a distance of a few tens of microns from the focal spot away allowing to record an extended PL image. However, Δr equals only 2.3 pixels (in other words, one pixel corresponds to 192 nm). Accordingly, it is difficult to distinguish the diffraction patterns if the Rayleigh criterion is exactly matched. To be realistic, the intensity maxima should be separated by at least 5 pixels to be distinguishable. Thus, the practical spatial resolution limit is only ~1 µm. Accordingly, NCs should be deposited on a substrate in a way that they are separated by a few micrometers (*e. g.*, by spin-coating). To check that the detected emission stems from single emitters and not from small clusters, the concentration of the NC dispersion used for spin-coating can be varied. The density of emitters on the substrate should change accordingly. Furthermore, *blinking* is a typical sign for single emitters as discussed later.

The used lens reduces not only the spatial resolution but has also the consequence that only ~7 % of the grating is illuminated. This seems to be a huge problem, but that is not the case. In reality, the wavelength resolution is not limited by the number of illuminated grating lines (Equation 3.8) but due to the spot size of the imaged slit, which is ~50 µm and corresponds to 2–3 pixels under ideal conditions. Thus, the real spectral resolution is more than an order of magnitude worse than the theoretical value. Therefore, it does not matter too much if the grating is not fully illuminated since the theoretical resolution will be still better than the device limited one.[133] Actually, if a better wavelength resolution is needed, a grating with 1200 lines mm^{-1} can be used instead of the usual 300 lines mm^{-1}, which increases the resolution again. The only drawback, in this case, is that the signal is spread over more pixels. Accordingly, the signal per pixel decreases and the detector noise becomes more significant. This demands longer integration times.

The spectrograph has a second exit port, which can be reached using a flip mirror. At this port, there is no CCD connected, but an optical multimode fiber by *AMS Technologies* with the maximum transmission in the range of 500–700 nm. Its refractive index has a step profile with a core and shell diameter of 105 µm and 125 µm, respectively. The fiber has an

NA of 0.22, which is larger than the NA of the lens in front of the spectrograph. Thus, all light focused on the fiber can be coupled in. The position of the fiber corresponds to the center pixel of the CCD. Accordingly, it is possible to couple either a specific wavelength into the fiber if a grating is used or all light from a small sample region if the mirror mode is chosen. The fiber is split into two equal arms by a non-polarizing broadband beamsplitter. Both fiber ends are connected to single-photon detectors based on avalanche photodiodes (APDs) for the wavelength range of 400–1060 nm (*SPCM-AQRH-16-FC* by *Excelitas Technologies*). They feature a very low dark count rate of only 25 cps, which enables the detection of weak signals from single emitters. Their timing resolution is 350 ps, which will affect the temporal resolution of the measurements discussed below.

This configuration allows for three types of experiments. First, by relating the arrival time of emitted photons to the timing of the laser pulses, it is possible to obtain PL decay traces. This method is called TCSPC and will be discussed in detail below.[134] Since only one APD is used in this case, the beamsplitter may be omitted if a sample shows only a weak emission. Nevertheless, the beamsplitter leads to an intensity interferometer known as Hanbury Brown–Twiss configuration, which enables the second experiment. By measuring the second-order correlation of the arriving photons, the photon statistics can be determined. In the case of single emitters, this may lead to a phenomenon known as *antibunching*.[135] It is possible to determine the biexciton QY from such a measurement.[136] Finally, it can be informative to simply look at the PL intensity of a single emitter over time. It may fluctuate between 'on/off'-states, which is known as *blinking*. A typical example is that a single emitter is occasionally charged, which leads to a high probability for nonradiative recombination due to an Auger process.[137]

TCSPC is based on the correlation of two signals as illustrated in Figure 3.9. The first one is given by a trigger corresponding to the repetition rate of the laser. This is represented by the vertical lines in panel (a). The second one is given by the detection of individual photons, which is shown by the green and orange dots representing photons from the laser and PL, respectively. Accordingly, two measurements are needed. During the first one, the central wavelength of the spectrograph is chosen to direct laser photons to the APD. The second one records the PL photons. When taking a closer look at the laser photons, it appears that they arrive with a slightly varying delay after the trigger. To characterize this delay, a timer always starts when the trigger pulse arrives from the laser and stops when a laser photon is detected. The obtained start/stop delays are plotted as a histogram with a bin width of 25 ps. If a second photon is detected after a certain laser trigger pulse, it would not yield a second start/stop delay. To minimize such events, the light hitting the APD should be attenuated as much that the count rate of detected photons is only 1 % of the laser repetition rate (rule of thumb). This start/stop technique gives a probability distribution for the detection of a photon after the laser trigger pulse arrived. Accordingly, the start/stop delay can be interpreted as a time axis.

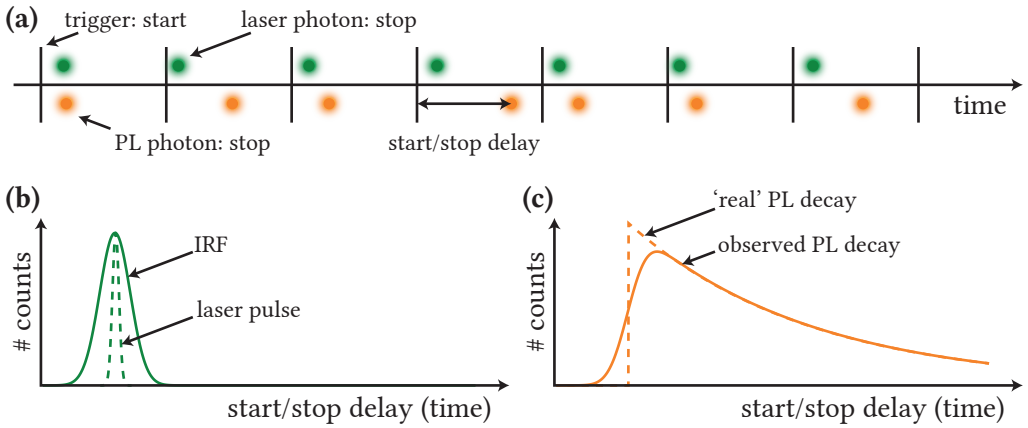

Figure 3.9: TCSPC and Time Resolution. **(a)** Sketch showing the detection of individual photons over time. The vertical lines correspond to the trigger signal from the laser. The green and orange dots refer to detection events of photons at the laser and PL wavelengths, respectively. The delay between the trigger and a detection event is called start/stop delay. **(b)** Histogram showing the distribution of start/stop delays in case of laser photons, which equals the IRF. It is broader than the pure laser pulse width. **(c)** A similar histogram for the case of PL photons, which resembles the PL decay. The observed trace deviates from the expected decay, especially during the signal rise.

The solid line in panel (b) sketches a typical result. There is a time offset due to different path lengths of the optical and electrical signals. Furthermore, the curve has a characteristic width of typical ~1 ns, which is much larger than expected given a laser pulse duration of less than 100 ps (dashed line). The solid line is a good estimation of the instrument response function (IRF), which is defined as the system's response to an infinitesimal short signal. Thus, it characterizes the time resolution of the system. It is worse than the laser pulse width due to additional factors affecting the timing (*e. g.*, APD resolution of 350 ps, jitter of laser trigger and detection system). The zero of the time axis is defined to be at the maximum of the IRF.

The orange dots representing the detection of PL photons are distributed over a larger time interval. This reflects the fact that the excited state of an emitter has a certain lifetime. The corresponding histogram is shown in panel (c) by the solid line. To capture the complete decay and to avoid measurement artifacts, the laser repetition rate must be adjusted in order to give the sample enough time to fully relax to the ground state before the next laser pulse arrives. In the case of monomolecular recombination of charge carriers after resonant excitation, the PL signal should rise as a step function and decay monoexponentially as shown by the dashed line. Due to the finite time resolution of the system, the obtained decay trace is given by a convolution of the real decay with the IRF. One should keep this in mind when investigating signals in the range of a few nanoseconds. In some cases, it might be reasonable to apply a reconvolution procedure to analyze such short-lived signals. Nevertheless, the limited time resolution is a small drawback of this versatile setup. In the next section, a streak camera is presented, which enables PL measurements with a time resolution of 1 ps using a sophisticated technique.

3.2.3 Time-Resolved Photoluminescence Spectroscopy: What a Modern Streak Camera Measurement Can Tell Us

PL measurements with high time resolution can resolve ultrafast processes within a sample. This could be the relaxation of charge carriers, which takes place on a time scale ranging from femto- to picoseconds. In the last section, TCSPC was introduced as a technique to record time-resolved PL signals. Nevertheless, due to a time resolution of only ~1 ns it is mainly capable of characterizing the PL decay. There are two other prominent techniques revealing the temporal evolution of PL signals. On the one hand, *fluorescence upconversion* can give a time resolution, which is only limited by the laser pulse width (~100 fs). However, its experimental realization is quite complex and it is not that sensitive for weak signals.[138] On the other hand, a modern *streak camera* can resolve the PL dynamics over a large spectral range with a time resolution of 1 ps. During my PhD, such an instrument (*Universal Streak Camera C10910*, *Hamamatsu*) was set up and this section will give an overview of the required laser system, the working principle of the streak camera, and some physical processes that can be observed with such a setup.

For the investigation of fast phenomena, the sample must be excited with laser pulses that are shorter than the process of interest. A *Mira Optima 900-F* (*Coherent*) can deliver suitable pulses with a temporal width of less than 200 fs. Its working principle is outlined in the following. Figure 3.10 shows the laser cavity with all relevant elements. The heart is a Ti:Al_2O_3 (Ti:sapphire) crystal, which is excited by a continuous wave (CW) pump laser (*Verdi G12*, *Coherent*, 532 nm, 12 W). The excited titanium atoms lead to PL in the range of 680–1100 nm.

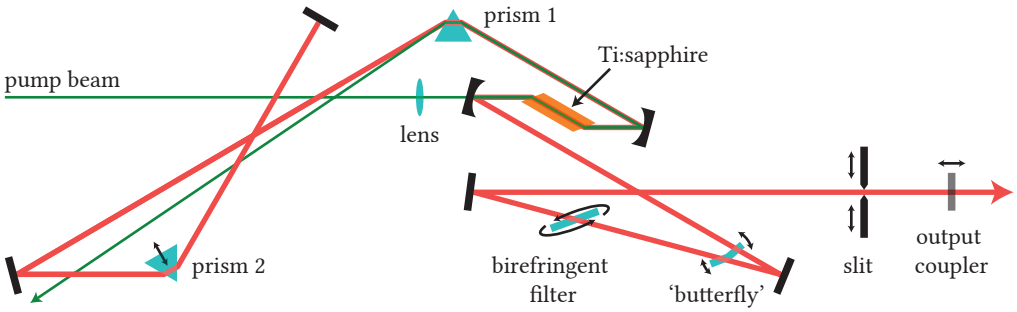

Figure 3.10: The *Mira Optima 900-F*. A *Verdi G12* is used as the pump laser (532 nm, 12 W). It is focused on a Ti:sapphire crystal, which leads to population inversion. The laser cavity is folded many times using high-reflective mirrors. The laser wavelength can be tuned in the range of 700–1020 nm using a BRF. A vibrating piece of glass (*butterfly*) induces small changes to the cavity, which lead to intensity fluctuations. Due to nonlinear self-focusing of the laser beam within the Ti:sapphire crystal, the laser beam narrows at high intensity. An adjustable slit can block all but this intense mode, which enables mode-locking in the range of 730–900 nm. This leads to laser pulses with a duration of less than 200 fs, while two prisms compensate the chirp introduced by various elements within the cavity. The laser beam exits the cavity through an output coupler. The cavity length corresponds to a repetition rate of 75.6 MHz, which can be slightly adjusted by translating the output coupler.

A fraction will travel along the optical axis of the cavity and will be back-reflected. By introducing a tunable birefringent filter (BRF), only light within a small wavelength range can efficiently travel in the cavity (obviously, the reflectance efficiency of the mirrors affects this as well). If the Ti:sapphire crystal is excited strong enough population inversion is reached (more titanium atoms are in the excited state than in the ground state). Thus, the reflected light is amplified due to stimulated emission when it passes through the crystal again. This leads to CW lasing at a certain wavelength (700–1020 nm), while the cavity length must equal to an integer multiple of the half-wavelength (longitudinal mode). In principle, there are many longitudinal modes possible within the range defined by the BRF. However, the mode that has initially the highest power by chance is amplified the most, while the other modes die out.

To achieve a pulsed laser operation, a kind of 'shutter' must be put into the cavity, which only allows intense pulses to transmit. In this case, the pulse would stimulate nearly all excited titanium atoms when it passes, which prevents the formation of a second pulse. There are various ways to realize such a 'shutter' (*e. g.*, optical modulators or organic dyes, which are only transparent for intense light). In case of the Mira, the 'shutter' is based on the *optical Kerr effect*. The refractive index of the Ti:sapphire crystal depends on the intensity of the light passing through. Due to the radial intensity profile of the laser beam, the crystal acts as a lens for intense light, which leads to a smaller beam diameter. By inserting a variable slit in the cavity, it is possible to block the broad CW beam, while an intense laser pulse is not affected. Obviously, a starting mechanism for this pulsed operation is needed.

A pulse can be interpreted as a superposition of many modes with a fixed phase relation. Therefore, the pulsed operation is also called mode-locked (ML). However, as mentioned before, only one mode is stable within the cavity (neglecting the effect of *spatial hole burning*, which may allow for a second mode). Nevertheless, rapid changes in the cavity length can lead to the presence of several modes with random phase at the same time, which causes strong power fluctuations. Accordingly, a vibrating piece of glass (*butterfly*) is put in the cavity, which slightly alters the optical path length. Now, if the light intensity is by chance high enough to activate the 'shutter' mechanism, a laser pulse builds up. Furthermore, a nonlinear process, called *self-phase modulation*, creates additional adjacent modes, which intensify the pulse even more. Accordingly, a short laser pulse has a considerable spectral width. As soon as ML operation is established, the butterfly is halted to stabilize the laser. It should be noted that the wavelength range, where ML operation is possible (730–900 nm), is considerably smaller than the range for CW lasing.

The last challenge is to keep the pulse short and stable. As the index of refraction is wavelength-dependent, the spectral parts of the pulse travel at different speeds, which leads to a temporal broadening known as *chirp*. Furthermore, since the refractive index of the crystal depends on the light intensity, which differs between pulse maximum and rising/falling edges,

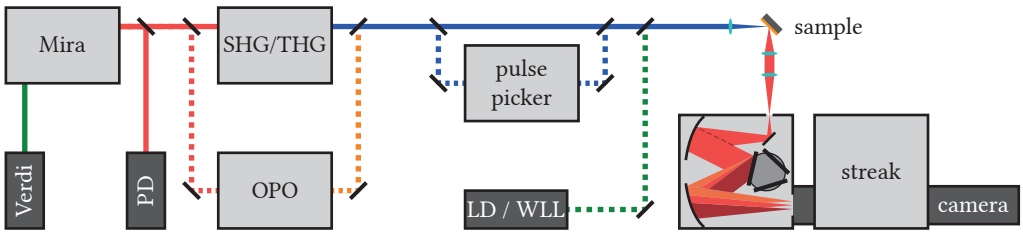

Figure 3.11: The Streak Setup. A *Mira Optima 900-F* is pumped by a *Verdi G12* and emits short laser pulses at a repetition rate of 75.6 MHz. Using a glass plate, a small fraction of the beam is deflected to a PD, which delivers trigger pulses needed for the streak operation. The output of the Mira can be converted to other wavelength ranges using SHG/THG processes or an OPO. If needed, the repetition rate can be reduced using a pulse picker. The laser beam is focused on a sample and the corresponding PL is collected and focused on the entrance slit of a spectrograph. Here, the light is horizontally separated according to its wavelength and sent to the streak main unit, which converts the arrival time of the photons in a certain vertical deflection. The resulting 2D image is recorded using a camera. If the streak is operated in the slow single sweep mode, it is also possible to use LDs or a WLL as the excitation source.

the pulse shape changes as well while passing through the crystal. These effects can be compensated by introducing two prisms in the cavity, which produce slightly different path lengths for different wavelengths. Thus, the relative phases of the modes forming the pulse stay constant after each cavity round trip. Accordingly, a steady-state is reached, which is known as a *soliton*. Always when the pulse hits the output coupler, a small fraction of the pulse exits the cavity. Thus, the cavity length determines the repetition rate of the laser (75.6 MHz), which can be slightly adjusted by translating the output coupler.

The wavelength range supported by the Mira is not sufficient for the excitation of typical samples. Accordingly, some processes are required to convert the wavelength to other parts of the spectrum. The combination of them on an optical table is shown in Figure 3.11. The easiest way is to use SHG or third-harmonic generation (THG) provided by the *Harmonics* unit (*Coherent*). In this case, the laser beam is focused on a BaB_2O_4 (BBO) crystal. By adjusting the angle of the crystal, phase-matching is achieved leading to SHG. Optionally, the time delay between the remaining fundamental and new SHG pulse resulting from the dispersion within the crystal is reduced to zero using a prism pair. Furthermore, a tunable wave plate can be used to match the linear polarization of fundamental and SHG pulses. Thus, the fundamental and SHG pulses can interact in a second nonlinear crystal leading to THG, while phase-matching is again achieved by adjusting the angle of the crystal.

Alternatively, an optical parametric oscillator (OPO) can cover large wavelength ranges in the IR and visible spectrum harnessing nonlinear optical processes. Since the OPO is not used for the measurements presented in this thesis, only a quick overview of its working principle is given in the following. In short, it is based on collinear, noncritically phase-matched parametric interaction in $KTiOPO_4$ (KTP) or $CsTiOAsO_4$ (CTA) crystals. This means that the photons coming from the Mira are converted within a birefringent crystal in two lower

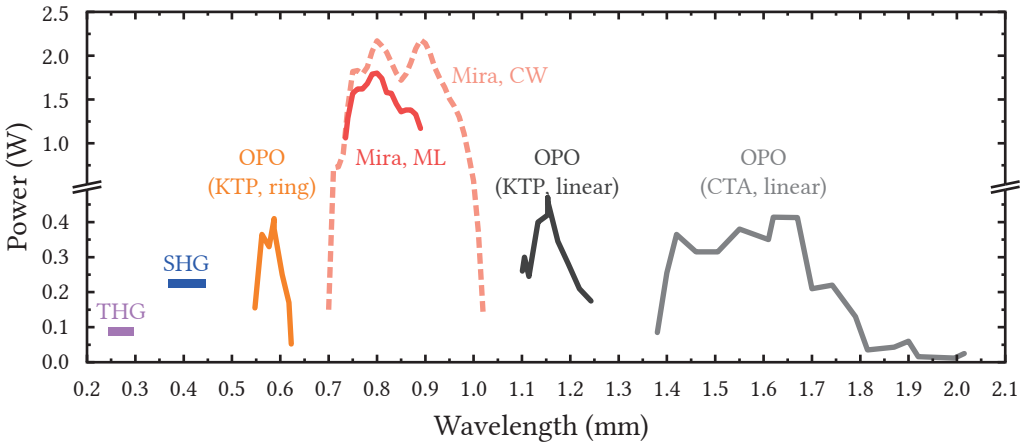

Figure 3.12: Available Laser Wavelength and Power at the Streak Setup. The *Mira Optima 900-F* enables CW lasing from 700 nm to 1020 nm, whereas ML operation is only possible in the range of 735–895 nm. Wavelengths in the UV can be reached by SHG and THG processes (exact power not determined). Using an OPO with a KTP or CTA crystal, the IR region can be reached. If the OPO is operated in a ring configuration, where an SHG process takes place in a second beam waist, visible wavelengths in the range of 545–620 nm can be obtained.

energetic photons called signal and idler, while energy and momentum conservation is given. The refractive index mismatch at the three wavelengths can be minimized harnessing the birefringence of the crystal. Accordingly, the pulses have the same speed and stay in phase leading to an efficient conversion. The term *noncritical* refers to the fact that the propagation of light is along the optic axis of the crystal, which makes the process insensitive to small alignment deviations. One has to distinguish between an OPO and an optical parametric amplifier (OPA). In the latter case, only one pulse is present in the crystal at any given time. In the case of an OPO, signal or idler are confined within a cavity and its length is adjusted in a way that the oscillating pulse is synchronized with the repetition rate of the Mira. Accordingly, the next laser pulse from the Mira enters the crystal simultaneously with the previously generated signal pulse, which leads to *optical gain*. The possible signal wavelengths are in the IR ranges of 1100–1240 nm and 1380–2015 nm for KTP and CTA crystals, respectively. Furthermore, in case of the KTP crystal, a ring configuration of the cavity allows for a second beam waist, where the IR signal can be converted to the visible range (545–620 nm) using highly efficient intracavity SHG. For this, a LiB_3O_5 (LBO) crystal is used and phase-matching is achieved by tuning its temperature. The available power for all possible wavelength ranges is shown in Figure 3.12.

In some cases, it may be useful to reduce the repetition rate, with which the sample is excited. As indicated in Figure 3.11, this can be done using a pulse picker based on an acousto-optic modulator (*PulseSelect*, *APE*). In this case, the laser beam is focused on a SiO_2 quartz crystal, which is mounted on a piezoelectric transducer. By applying an oscillating electric field, the crystal starts vibrating, which generates a standing sound wave within the crystal. The corresponding modulation of the refractive index acts as a 3D optical grating.

Accordingly, individual pulses can be deflected by a certain amount (first diffraction order) if the electric field is applied at an appropriate time. Thus, specific pulses are separated from the other ones, which will be blocked. Accordingly, the pulse repetition rate can be reduced (up to a factor of 260 000).

A streak allows also for the measurement of slow processes where less time resolution is required. In this case, it is possible to use laser diodes (LDs) by *Hamamatsu* providing 375 nm, 465 nm, 510 nm, and 655 nm or the WLL presented before as an excitation source.

Whatever excitation source is used, the light is focused on a sample in a thin cuvette or on a substrate and the PL is collected and focused on the entrance slit of a spectrograph (*SpectraPro HRS-300*, *Princeton Instruments*) using two achromatic lenses as shown in Figure 3.11. It should be noted that these lenses may introduce a significant chirp to the signal, which needs to be considered when analyzing the final data. The spectrograph horizontally separates the PL photons according to their wavelength and the light enters the streak camera, which is described in detail in the following.

The different components of a streak camera are illustrated in Figure 3.13. Light is focused on a horizontal slit, which is imaged on a photocathode by a lens system. There might be already some information stored in the horizontal direction (*e. g.*, the light wavelength by employing a spectrograph, or a real spatial coordinate if an object is imaged directly on the slit, which enables the recording of an ultra-slow-motion video).[139] At the photocathode, 10–20 % of the incident photons will generate single electrons due to the photoelectric effect. Using a charged mesh (7–15 kV), they are accelerated and fly horizontally through the evacuated streak tube. However, due to the presence of a capacitor they can be deflected vertically. By applying a time-dependent voltage, it is possible that the electrons are deflected by a certain amount depending on their arrival time. This effect will be discussed in detail later. Actually, there exists also a similar horizontal capacitor (not shown), whose purpose will

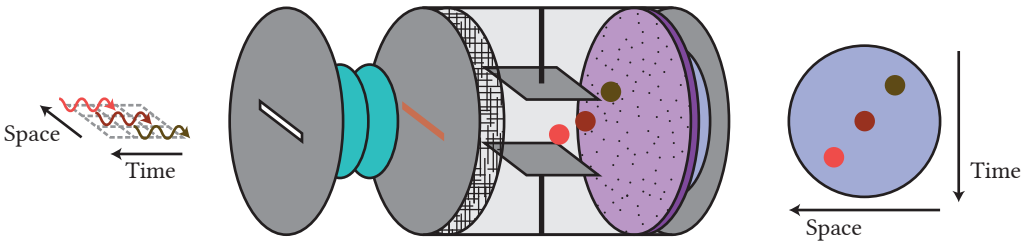

Figure 3.13: Illustration of a Streak Camera. Photons are focused on a variable horizontal slit. A lens system (light blue) images the slit on a photocathode (orange). Here, a photon may generate an electron, which is accelerated by a charged mesh. If no voltage is applied to the vertical capacitor, the electrons horizontally travel through the evacuated streak tube. By applying a time-dependent voltage, the electrons are deflected by a certain amount depending on their arrival time. There exists also a horizontal capacitor, which is not shown for simplicity. A charged MCP (purple) is used to multiply the electrons. Now, they hit on a phosphorous screen (blue), which is imaged using a camera. Thus, the vertical axis of the image can be related to a time axis.

be discussed below as well. Finally, the electrons will hit the tilted tubes of a multi-channel plate (MCP), which is charged by 400–900 V. This has two purposes. First, a single electron will be multiplied due to the avalanche effect by a factor of up to 10^4. Second, the MCP blocks remaining photons, which were not absorbed by the photocathode. Directly behind the MCP, the electrons will hit on a phosphorous screen, which thus emits photons. These are detected using a camera (*ORCA Flash 4.0 V3, Hamamatsu*). The obtained image still contains the horizontal information as in the beginning, while the vertical component can now be related to a time axis. This also explains the name *streak*, since the photons are streaked over the detector with time. Notably, this technique works in principle on a *single-shot* basis. This means that the emission originating from a single excitation event may yield a useful signal. Summing over many excitation cycles just improves the statistics. This is in contrast to TCSPC, where only the histogram acquired over many cycles contains meaningful information. A single start/stop delay is useless.

Nevertheless, it is disadvantageous to take the streak camera image as obtained due to the following problem. On the one hand, a single electron is not multiplied by an exact factor within the MCP. On the other hand, a certain number of electrons will not always generate the same amount of photons at the phosphorous screen. Thus, an electron generated by a single photon can lead to a (strongly) varying signal at the camera. To compensate for this issue, the raw data are analyzed in order to count individual incoming photons. To this end, it is necessary to attenuate the signal in such a way that only individual spots appear on a single camera image. The centers of these spots are determined and a photon count is increased by one for the corresponding pixels. Accordingly, this procedure is called *photon counting*. It circumvents not only the problem mentioned above but also removes nearly all detector noise. Accordingly, the signal to noise ratio of the final measurement, consisting of a sum of many frames, is purely given by the photon counting statistics $\left(\Delta N = \sqrt{N}\right)$.

Now, as the general working principle of a streak camera has been presented, the focus lies on the different operation modes named single sweep, synchroscan, and shift-blanking. In the case of *single sweep*, an LD at a low repetition rate (≤ 4 MHz) is used as the excitation source. When it emits a laser pulse, an electric trigger signal is sent to the streak with a certain delay in order to match the arrival of the first PL photons. Figure 3.14 visualizes what is then happening in the capacitor section of the streak tube. Initially, a constant voltage is applied to the vertical capacitor, which deflects the electron beam to the top of the phosphorous screen. When the trigger pulse arrives, the voltage linearly decreases until it corresponds to an electron deflection to the bottom of the phosphorous screen. Depending on the slope of this voltage ramp, the length of the measurable time window can be adjusted between 1 ns and 1 ms. Now, the voltage must be reset, allowing the streak to wait for the next trigger pulse. However, some photons may still arrive at the streak after the voltage sweep has finished. If the vertical voltage is now simply increased again, these photons would yield an artifact

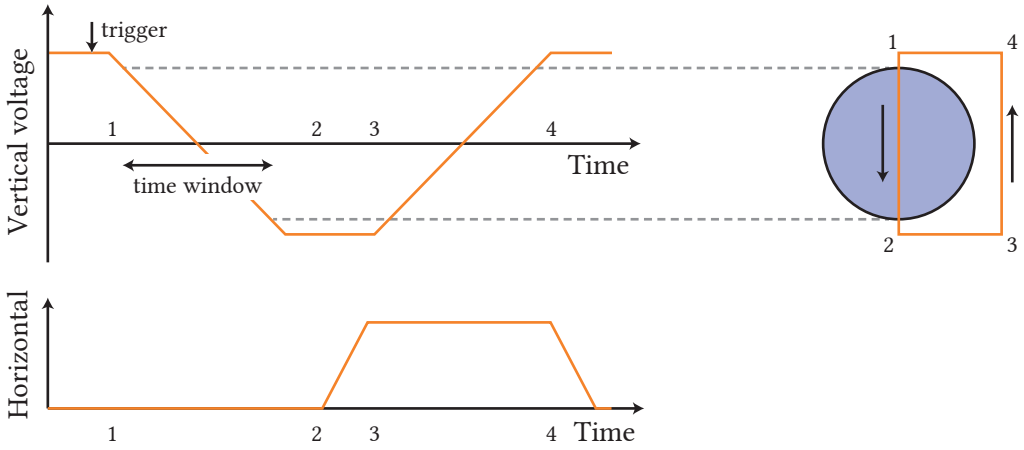

Figure 3.14: Streak Operation: Single Sweep. The time-dependent voltage applied to the vertical (horizontal) capacitor is shown in the top (bottom) panel. The trace of a continuous electron beam on the phosphorous screen is sketched on the right-hand side.

in the image. This is known as the *back-sweep problem*. In order to circumvent it, a second capacitor is needed, which is horizontally oriented. It can deflect the electron beam to the side of the phosphorous screen during the vertical back-sweep. The time resolution of such a measurement is roughly given by 0.8 % of the used time window. In case of the shortest time window, the trigger jitter affects the time resolution. This can be minimized using a cable delay instead of an electrical delay unit. In this case, the maximum time resolution reaches 20 ps for a time window of 1 ns, which is actually shorter than the pulse width of the used LDs (~50–100 ps).

To improve the time resolution further, the streak operation needs to change from a slow 'sweep on demand' to a fast and continuous sweep mode, which is synchronized with the repetition rate of the used laser. Accordingly, this mode is called *synchroscan*. In this case, the laser system based on the Mira is used as the excitation source. Directly behind the laser exit, a glass plate directs a small fraction of photons to a fast PD, which generates precise trigger pulses. Within the streak, an electric resonant circuit is synchronized with this trigger pulses and generates a sinusoidal voltage, which is applied to the vertical capacitor. Similar to the single sweep-mode, the electron beam will be deflected over the phosphorous screen (see Figure 3.15). Using different voltage amplitudes, the observable time window can be adjusted (70 ps, 200 ps, 600 ps, 1200 ps, and 2200 ps). Obviously, a correction factor compensating for the nonlinearity of the sine is needed. Again, a certain delay can be added to the incoming trigger pulse to position the signal of the first arriving photons in the top region of the phosphorous screen. Now, the time resolution can reach less than a picosecond in case of the shortest time window. Unfortunately, it is not possible to solve the back-sweep problem using the horizontal capacitor, since the electronics is too slow. This means, that if there are still photons arriving after ~6 ns, they will yield an erroneous signal as well. In case of the shortest time window, their signal may be assumed to be constant and, thus, simply

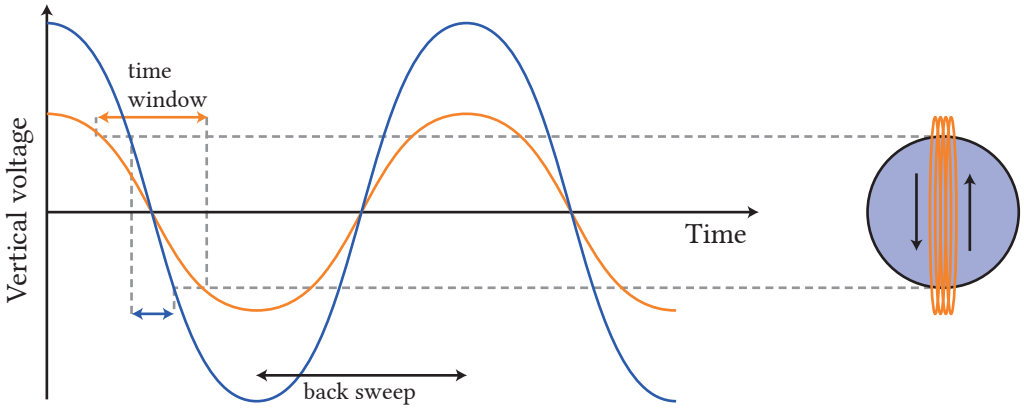

Figure 3.15: Streak Operation: Synchroscan. The time-dependent voltage applied to the vertical capacitor is shown for two different amplitudes, which result in different measurement time windows. The trace of a continuous electron beam on the phosphorous screen is sketched on the right-hand side.

subtracted. However, this is not always the case, but fortunately, there is a solution to this problem.

The *shift-blanking* mode of the streak camera can be used to solve the back-sweep problem of the synchroscan mode. Here, a pulse picker reduces the repetition rate of the laser pulses as much ($\leq$ 10 kHz) that the electronic controlling the horizontal capacitor is fast enough to shift the electron beam in time to the side of the phosphorous screen. This process is visualized in Figure 3.16. The vertical capacitor behaves as in the synchroscan mode. When a laser pulse arrives, the electron beam streaks once over the phosphorous screen and is then quickly shifted to the side by the horizontal capacitor. Now, it sweeps up and down for several microseconds before it slowly moves back to reach the initial position in time when the next laser pulse arrives. This procedure solves not only the back-sweep problem but also has the

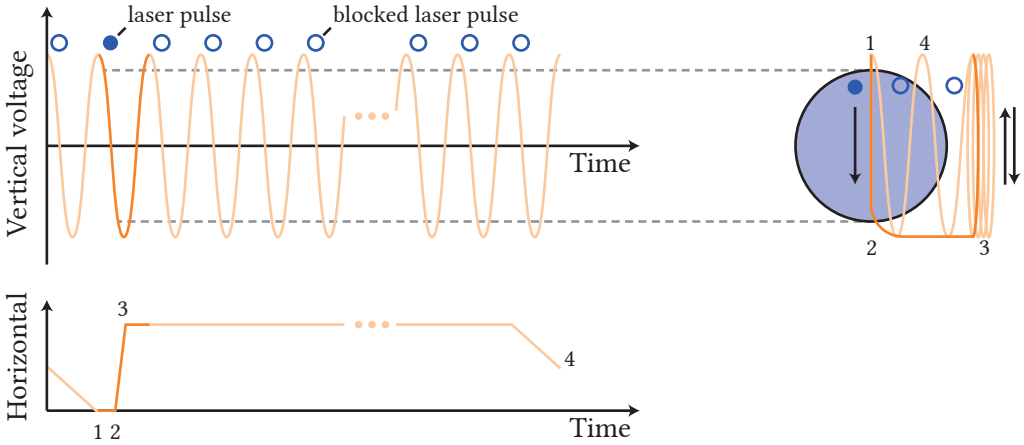

Figure 3.16: Streak Operation: Shift Blanking. The time-dependent voltage applied to the vertical (horizontal) capacitor is shown in the top (bottom) panel. The trace of a continuous electron beam on the phosphorous screen is sketched on the right-hand side. The blue spots indicate when a (blocked) laser pulse would arrive.

advantage that the sample has fully relaxed to the ground state before it is excited the next time. This can also be an issue in the normal synchroscan mode, which is why it might be reasonable to use the pulse picker in this case as well, but not reducing the repetition rate as much.

The time resolution can reach 1 ps in case of synchroscan or shift-blanking and is only limited by the laser pulse width (~50–100 ps) in case of the single sweep mode. This is a great improvement compared to the 1 ns resolution obtained by TCSPC measurements. Nevertheless, the time resolution may be affected by several factors, when using the shortest time window. Under unfavorable circumstances, the time resolution can deteriorate to several picoseconds. Some critical factors are:

- The spectrograph stretches the signal due to varying path lengths. Hence, the grating is intentionally not fully illuminated.
- The width of the horizontal entrance slit should be small (10–20 µm), since it is imaged onto the CCD. Otherwise, the signal is broadened along the time axis.
- The signal might be stretched if the sample is excited at multiple points (*e. g.*, in a cuvette) and if the imaging process onto the spectrograph slit is not perfect.
- The lens systems, which image the horizontal slit on the photocathode and the phosphorous screen on the camera, need to be optimized.

The final result of all these measurement procedures is a 2D map showing the PL intensity as a function of emission wavelength and time. Such data can yield versatile information about physical processes. Some of them will be highlighted in the following. Based on the physics of optical transitions presented in Subsection 2.1.2, a requirement for the emission of a photon is that both, electron *and* hole, are present at the states involved in the respective transition. This can be characterized by the Fermi distributions $f_{e/h}(\lambda)$ of electron and hole, which give the normalized occupation number of states involved in a transition with wavelength λ. Accordingly, the PL signal is proportional to the product of the Fermi distributions of electron and hole (see Equation 3.11). The proportionality constant is influenced by the presence of nonradiative recombination channels and can even be zero if the transition is optically inactive.

$$\mathrm{PL} \propto f_e \cdot f_h \tag{3.11}$$

If charge carriers are excited with excess energy, they will typically relax to the band edge, while $f_{e/h}(\lambda)$ changes during this process. Such relaxation processes can take up to several picoseconds. Accordingly, a quickly vanishing high energetic emission may be observed initially. Furthermore, the main PL signal stemming from the band gap transition will rise

with a certain delay. This is also observable if the high energetic transitions are optically inactive. Thus, one can investigate the charge carrier relaxation dynamics as a function of the initial excess energy. This effect can be observed for DPs and will be discussed in Section 5.2.

It is difficult to distinguish energetically close-lying transitions in steady-state PL spectra. However, their time-resolved signals may show distinct decay characteristics (*e. g.*, lifetime or shape), which can be identified using streak images. A typical example is given by the exciton, biexciton, and trion transitions.[140]

As mentioned before, nonradiative recombination of charge carriers can influence the signal. In the case of monomolecular recombination, the PL decays with a rate k_{PL} that comprises two components due to radiative (k_{r}) and nonradiative (k_{nr}) processes, whereby $k_{\mathrm{PL}} = k_{\mathrm{r}} + k_{\mathrm{nr}}$. The number of emission events with respect to all recombination events is thus given by $\frac{k_{\mathrm{r}}}{k_{\mathrm{PL}}}$. Actually, the number of absorption processes equals the number of all recombination processes due to particle conservation. Consequently, this ratio can be identified as the QY according to Equation 3.6. Thus, it is possible to determine the radiative and nonradiative rates using the QY and the observed PL decay rate k_{PL} as stated in Equation 3.12. It should be noted that PL, radiative, and nonradiative lifetimes can be defined as the inverse of the respective rates.

$$k_{\mathrm{r}} = k_{\mathrm{PL}} \cdot \mathrm{QY} \qquad k_{\mathrm{nr}} = k_{\mathrm{PL}} \cdot (1 - \mathrm{QY}) \tag{3.12}$$

Typically, it is impossible to differentiate between different types of energy transfer mechanisms using only steady-state spectroscopy (*e. g.*, PLE). Therefore, time-resolved PL spectroscopy is a prominent tool for the investigation of such processes. A simple reabsorption event, for example, would just lead to feeding of the acceptor's excited state population, thus prolonging its decay. Förster resonance energy transfer (FRET), on the other hand, introduces an additional 'decay channel' for the donor's excited state population. Therefore, the PL lifetime of the donor reduces in addition to the prolonged decay of the acceptor.[141]

Last but not least, it should be mentioned that time-resolved PL spectroscopy is even able to characterize some mechanical properties of colloidal NCs. For example, if the sample is dispersed in a solvent, it undergoes Brownian rotational diffusion. A linearly polarized laser may lead to a biased excitation of NCs depending on the current direction of their transition dipole moments. Consequently, the emission is initially polarized in the same plane. However, the orientation of the transition dipole moments becomes arbitrary again due to diffusion. If the relevant period of time is comparable to the PL lifetime, an effect is observable using appropriate polarizers and the Brownian rotational diffusion constant can be determined.[131]

As already stated, the PL signal is proportional to the *product* of the Fermi distributions of electron and hole. As a consequence, it is difficult to distinguish between them. This challenge can be simplified using DT spectroscopy, which yields a signal that is proportional to the *sum* of both Fermi distributions (under certain circumstances). This technique will be discussed in the following section.

3.2.4 Differential Transmission Spectroscopy: A Comparison of $\Delta T/T_0$ with ΔOD

DT spectroscopy is a pump/probe technique. A pump laser pulse excites a sample before a second laser pulse probes the current state. The transmitted intensity of the second pulse is recorded as a function of the time delay between both pulses. Since the presence of excited charge carriers affects the transmission of a sample, this simple idea leads to a well-established measurement scheme, which enables the investigation of the charge carrier dynamics taking place. For my research, I used a custom-built *Transient Absorption Spectrometer* by *Newport*. A detailed description of the setup with all modifications can be found in the PhD thesis of my colleague Bernhard Bohn.[132]

As mentioned before, the transmitted intensity of the probe pulse is the quantity of interest. By relating this value to the initial intensity of the probe beam, it is possible to calculate the transmission or absorption of the sample in the excited state. This leads to two quantities that are frequently used in literature. First, the change in transmission relative to the transmission of the ground state: $\Delta T/T_0(\lambda)$. Second, the change in optical density: $\Delta\mathrm{OD}(\lambda)$. While this section starts with a brief explanation of the experimental setup, both conventions are described and compared in the second part.

As discussed in the previous sections, charge carrier relaxation takes place on a femto- to picosecond time scale. Accordingly, short laser pulses are needed to investigate such processes. Here, a *Libra-HE+* amplifier system by *Coherent* provides 800 nm-laser pulses with a duration of approximately 100 fs at a repetition rate of 1 kHz. Using a laser beamsplitter, two beams are created, while the timing between individual pulses of the two beams can be controlled.

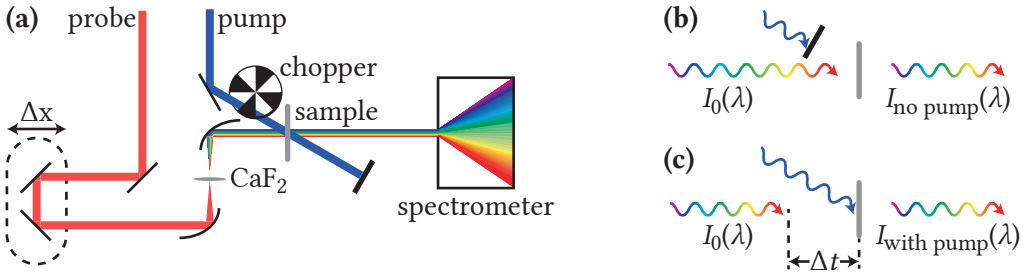

Figure 3.17: Illustration of DT Spectroscopy. (a) The pump beam (blue) is directed through a chopper wheel, which blocks every second laser pulse, onto the sample. The fundamental beam of the *Libra-HE+ amplifier* (red) is focused on a CaF_2 crystal to generate a white-light spectrum $I_0(\lambda)$. This is centered on the excitation spot given by the pump beam, while the beam diameter is smaller. The transmitted intensity profile is detected using a spectrometer. A translation stage (Δx) generates a controlled time delay between the pump and probe laser pulses. **(b)** If the pump beam is blocked by the chopper, the transmission of the ground-state can be calculated using the transmitted intensity $I_{\text{no pump}}(\lambda)$. **(c)** If the pump beam is not blocked, the sample will be excited. Now, the transmission of the excited state can be obtained using $I_{\text{with pump}}(\lambda)$. Generally, the result depends on the pump wavelength, the pump intensity, and the time delay Δt between pump and probe pulses.

The first beam serves as the pump. Obviously, its wavelength must be adjusted to enable the desired excitation process. This can be done using either SHG in a BBO crystal or an OPA (*OPerA Solo*, built by *Light Conversion* and distributed by *Coherent*).[142] The first method leads to laser pulses with rather low intensity fluctuations from pulse to pulse. However, the wavelength is fixed to 400 nm. The second option can be used to generate wavelengths in the range of 190 nm up to 12 µm, but with slightly larger intensity fluctuations, which will affect the signal in the end. As illustrated in Figure 3.17a, the pump beam shown in blue is focused onto the sample (on a substrate or in a thin cuvette). Before, it passes through a chopper wheel, which is synchronized to the laser repetition rate, to block every second pulse. Thus, the transmitted intensity of the probe pulse can be recorded for both cases, ground and excited state of the sample.

Focusing on the probe part of the setup, a crucial step is to control the time delay between pump and probe pulses. For this, a retroreflector mirror is mounted on a translation stage, which enables a variation of the probe beam path length. Up to now, the probe beam, sketched by the red line, still has a wavelength of 800 nm. It would be possible to adjust this wavelength similar to the pump beam and measure the sample transmission at a fixed wavelength. However, it is much more favorable to record a complete transmission spectrum at once. To generate the needed white-light spectrum, the probe beam is focused on a CaF_2 crystal. The dynamic interplay of several nonlinear effects (mainly self-phase modulation) leads to a huge spectral broadening of the laser pulse.[143] There are also other crystals allowing for a white-light generation (*e. g.*, $Y_3Al_5O_{12}$ (YAG) or sapphire), however, CaF_2 leads to a spectrum reaching far into the UV region, which is advantageous for the investigated samples. Unfortunately, CaF_2 is prone to photodamage. Accordingly, the crystal is mounted on a translation stage, which moves the crystal in plane. It should be noted, that parabolic mirrors are used to focus and collimate the probe beam. This is done to avoid a large chirp of the laser beam arising from the wavelength-dependent speed of light in matter (*e. g.*, a lens), which would cause a delay of shorter probe wavelengths. The white-light beam is directed onto the excitation spot given by the pump beam. Importantly, the beam diameter of the probe is smaller than the one of the pump beam ($d_{\mathrm{pump}} = 650\,\mu\mathrm{m}$, determined by an *SP928 Beam Profiling Camera*, *Ophir Spiricon Europe GmbH*). This ensures that the probed sample volume is uniformly excited. The transmitted probe beam is sent to a spectrometer, which can record the wavelength-dependent intensity. Interestingly, it is possible to calculate both, $\Delta T/T_0(\lambda)$ and $\Delta\mathrm{OD}(\lambda)$, without the knowledge of the probe beam intensity $I_0(\lambda)$ in front of the sample (as discussed below). Nevertheless, the recorded intensity spectra are divided by $I_0(\lambda)$, which is measured in a separate detection path (not shown in Figure 3.17a), to reduce noise arising from power fluctuations in the white-light spectrum.

Figure 3.17, b and c, show a magnification of the sample region depending on the chopper position. Since there is always some chirp in the probe beam (*e. g.*, the white-light needs to

travel out of the CaF_2 crystal), this effect is illustrated by the color gradient. The transmitted intensity of the probe beam is termed $I_{\text{no pump}}(\lambda)$ or $I_{\text{with pump}}(\lambda)$ depending on the respective chopper position. Both intensity spectra are saved together with the current time delay Δt between pump and probe pulses. Now, $^{\Delta T}/_{T_0}(\lambda)$ and $\Delta\text{OD}(\lambda)$ can be calculated according to Equations 3.13 and 3.14, respectively. Here and in all following equations, the zero subscripts refer to the case of a blocked pump beam.

$$\frac{\Delta T}{T_0} = \frac{T - T_0}{T_0} = \frac{\frac{I_{\text{with pump}}}{I_0} - \frac{I_{\text{no pump}}}{I_0}}{\frac{I_{\text{no pump}}}{I_0}} = \frac{I_{\text{with pump}}}{I_{\text{no pump}}} - 1 \tag{3.13}$$

$$\begin{aligned}\Delta\text{OD} = \text{OD} - \text{OD}_0 &= -\log_{10}(T) - \left(-\log_{10}(T_0)\right) = \\ &= \log_{10}\left(\frac{T_0}{T}\right) = \log_{10}\left(\frac{\frac{I_{\text{no pump}}}{I_0}}{\frac{I_{\text{with pump}}}{I_0}}\right) = \log_{10}\left(\frac{I_{\text{no pump}}}{I_{\text{with pump}}}\right)\end{aligned} \tag{3.14}$$

Now, the big question is how to interpret these signals. Typically, the dominant effect is phase space filling, which will also be the case for the measurements discussed in this thesis. Nevertheless, one should always bear in mind that there are many other effects possible (*e. g.*, excited state absorption, band gap renormalization, optical Stark effect, carrier induced Stark effect, transition broadening, ...).[101,144–154] Phase space filling may decrease the absorption coefficient of a certain transition as some of the final states are already occupied or some of the initial states are not filled. On the other hand, stimulated emission enters stage due to the presence of excited charge carriers. When neglecting all other aforementioned effects possibly influencing the signal, $^{\Delta T}/_{T_0}(\lambda)$ and $\Delta\text{OD}(\lambda)$ can be related to the Fermi distributions $f_{\text{e/h}}(\lambda)$ of electrons and holes, respectively.

If the sample is in an excited state, the intensity decreases not only according to the Lambert-Beer law but also increases exponentially due to stimulated emission as can be seen in Equation 3.15.

$$\frac{I_{\text{no pump}}}{I_0} = \mathrm{e}^{-\alpha_0 d} \qquad \frac{I_{\text{with pump}}}{I_0} = \mathrm{e}^{-(\alpha - e)d} \tag{3.15}$$

Here, $e(\lambda)$ characterizes stimulated emission and $\alpha(\lambda)$ determines the absorption of the excited state. Both quantities can be related to $\alpha_0(\lambda)$ using the Fermi distributions $f_{\text{e/h}}(\lambda)$ of electrons and holes, respectively. As discussed in Subsection 3.2.3, the Fermi distributions take values between 0 and 1 depending on the presence of electrons or holes at states participating in transitions with wavelength λ. A certain transition absorbs less if final states are already occupied *or* initial states are empty. This is a crucial difference compared to the interpretation of PL signals, which require the presence of both, electrons *and* holes, at a certain transition.

Accordingly, phase space filling leads to $\alpha(\lambda) = \alpha_0(\lambda)\big(1 - f_\mathrm{e}(\lambda)\big)\big(1 - f_\mathrm{h}(\lambda)\big)$. On the other hand, stimulated emission is only possible if electron *and* hole are present, which yields $e(\lambda) = \alpha_0(\lambda) f_\mathrm{e}(\lambda) f_\mathrm{h}(\lambda)$. Comparing the scenarios with and without the pump beam exciting the sample, an effective change of the absorption coefficient $\Delta\alpha(\lambda)$ can be defined according to Equation 3.16.

$$\Delta\alpha = (\alpha - e) - \alpha_0 = \big(\alpha_0(1 - f_\mathrm{e})(1 - f_\mathrm{h}) - \alpha_0 f_\mathrm{e} f_\mathrm{h}\big) - \alpha_0 = -\alpha_0\,(f_\mathrm{e} + f_\mathrm{h}) \tag{3.16}$$

As a last step, $\Delta T/T_0(\lambda)$ and $\Delta\mathrm{OD}(\lambda)$ can be related to $\Delta\alpha(\lambda)$ according to Equations 3.17 and 3.18, respectively.

$$\begin{aligned}\frac{\Delta T}{T_0} = \frac{T - T_0}{T_0} = \frac{(1 - A) - (1 - A_0)}{1 - A_0} &\overset{\text{Eq. 3.15}}{=} \frac{\mathrm{e}^{-(\alpha - e)d} - \mathrm{e}^{-\alpha_0 d}}{\mathrm{e}^{-\alpha_0 d}} = \frac{\mathrm{e}^{-(\alpha - e)d}}{\mathrm{e}^{-\alpha_0 d}} - 1 \overset{\text{Eq. 3.16}}{=} \\ &= \mathrm{e}^{-\Delta\alpha d} - 1 \overset{\text{Taylor, } \Delta\alpha d \ll 1}{=} \Big(1 - \Delta\alpha d + \mathcal{O}\big((\Delta\alpha d)^2\big)\Big) - 1 \approx -\Delta\alpha d \overset{\text{Eq. 3.16}}{=} \alpha_0 d\,(f_\mathrm{e} + f_\mathrm{h})\end{aligned} \tag{3.17}$$

$$\begin{aligned}\Delta\mathrm{OD} = \mathrm{OD} - \mathrm{OD}_0 &\overset{\text{Eq. 3.2}}{=} (\alpha - e) d \log_{10}(\mathrm{e}) - \alpha_0 d \log_{10}(\mathrm{e}) \overset{\text{Eq. 3.16}}{=} \\ &= \Delta\alpha d \log_{10}(\mathrm{e}) \overset{\text{Eq. 3.16}}{=} -\alpha_0 d\,(f_\mathrm{e} + f_\mathrm{h}) \log_{10}(\mathrm{e}) \overset{\text{Eq. 3.2}}{=} -\mathrm{OD}_0\,(f_\mathrm{e} + f_\mathrm{h})\end{aligned} \tag{3.18}$$

In both cases, it turns out that the signal is proportional to the *sum* of the Fermi distributions of electrons and holes, but with a different sign. In the case of $\Delta T/T_0(\lambda)$, a Taylor expansion must be used. Accordingly, the relation holds only for small $\Delta\alpha d$, which equals $\Delta\mathrm{OD} \ll \log_{10}(\mathrm{e}) \approx 0.43$. The fact that the DT signal due to phase space filling is proportional to the *sum* of both Fermi distributions is a further important difference compared to the interpretation of PL signals, which are proportional to the *product* of the same.

To summarize all these considerations, both conventions are equally applicable to investigate the excited state transmission. $\Delta\mathrm{OD}(\lambda)$ has the advantages that no Taylor series is needed to find a simple connection to the Fermi distributions and that its value can be directly compared to the OD spectrum. However, talking of absorption might be misleading since an excited state may result in stimulated emission, which is a different physical process compared to absorption. Therefore, $\Delta T/T_0(\lambda)$ is in terms of nomenclature closer to the measured quantity. Furthermore, in the case of quantitative analysis, it is always possible to use an

exact relation to the Fermi distributions if the assumption needed for the Taylor series is not valid. Accordingly, I will stick to $^{\Delta T}/_{T_0}(\lambda)$ in this thesis.

4

InP Quantum Dots: Fast Electron and Slow Hole Relaxation

In order to replace cadmium-based colloidal QDs in LEDs, InP-based core/shell QDs are a promising candidate, whereby the shell plays a crucial role in enhancing the radiative efficiency through surface passivation.[11,12] Nevertheless, besides the need for bright and stable QDs, their energetic structure must be taken into account when designing an LED. Depending on the energetic alignment of charge transport and injection layers with respect to the QDs, charge carriers may initially possess excess energy compared to the emitting transition. Thus, a relaxation process is needed before the desired emission is possible. As this process takes time (*e. g.*, due to the phonon bottleneck issue discussed in Subsection 2.2.3), competing nonradiative processes may become significant, thus reducing the radiative efficiency of the device. Accordingly, a fundamental understanding of the charge carrier relaxation in colloidal QDs is needed. While there are reports focusing on core-only QDs comprising cadmium[155–159] or InP,[160–163] the influence of a shell material is hardly discussed in the literature.

The following chapter is mainly based on Reference 164 and will present the charge carrier relaxation dynamics in InP-based core/shell colloidal QDs. The focus is hereby on the exact relaxation time scales as a function of the initial excess energy of electrons and holes. Furthermore, the question if actually all charge carriers eventually arrive at the states leading to emission is investigated. But first, the general optical performance of these QDs will be discussed.

4.1 What is the Performance?

During my research, two kinds of core/shell colloidal QDs were investigated: InP/ZnS and InP/ZnSe. The synthesis was optimized to reach a high PL QY in the red spectral region and is described in Subsection 3.1.3. The QDs have core and shell diameters of approximately 3 nm and 10 nm, respectively (see Table 3.2). As the exciton Bohr radius in InP is 9.6 nm, it can be expected that the quantum size effect plays a crucial role.[71] Figure 4.1 displays the absorption (gray area) and PL spectra (black line) of (a) InP/ZnS and (b) InP/ZnSe QDs. For both samples, the absorption spectra show an onset at approximately 600–650 nm and a continuously increasing signal toward shorter wavelengths. Furthermore, the absorption spectrum of InP/ZnSe QDs shows a constant offset, which is attributed to scattering caused by the presence of larger particles (*e. g.*, precursors) in the dispersion. The band gap energy of bulk InP is 1.35 eV, which corresponds to a wavelength of 920 nm.[47] The correspondingly large blueshift of the absorption onset observed for the QDs (~300 nm) can be explained by the quantum size effect (see Subsection 2.1.4). The strongly increasing absorption toward 350 nm (InP/ZnS QDs) and 450 nm (InP/ZnSe QDs) can be related to transitions involving the shell material since the band gap energy of bulk ZnS is 3.54 eV (350 nm)[48] and the one of ZnSe is 2.67 eV (464 nm).[49]

The emission maxima of both samples are located at 627 nm (InP/ZnS QDs) and 631 nm (InP/ZnSe QDs). The PL FWHM is 58 nm and 44 nm, respectively. These values are slightly larger compared to cadmium-based QDs emitting in a similar spectral range, which show an FWHM of ~30 nm.[165] Interestingly, the PL signals of individual InP/ZnS QDs, displayed in Figure 4.2, show a significantly smaller FWHM of only (28 ± 11) nm (mean value determined by the analysis of 16 spectra) compared to the 58 nm obtained from the ensemble PL spectrum. At the same time, the positions of the PL maxima slightly vary, which leads to an inhomogeneous broadening of ensemble spectra. The main reason for the varying peak

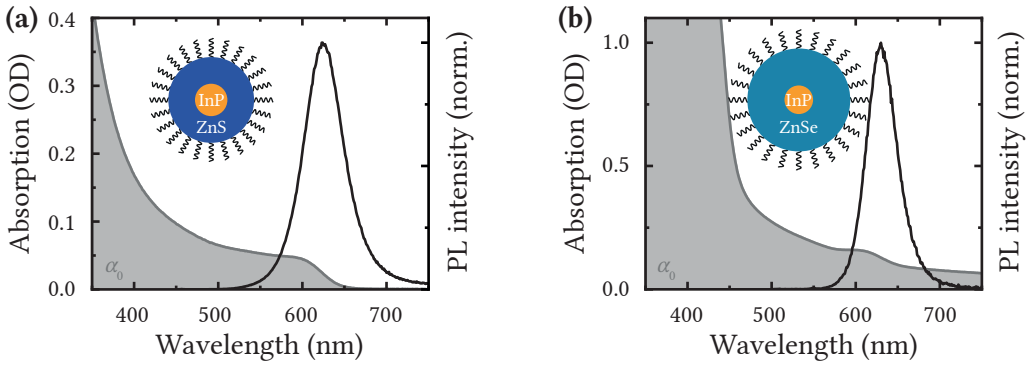

Figure 4.1: InP/ZnS and InP/ZnSe Core/Shell QDs. The absorption (gray area) and PL spectra (black line, λ_{ex} = 470 nm) of **(a)** InP/ZnS and **(b)** InP/ZnSe core/shell QDs dispersed in toluene.

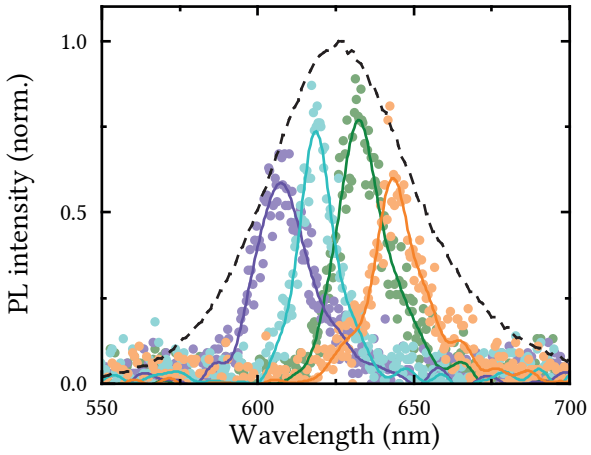

Figure 4.2: PL of Single InP/ZnS QDs. Representative PL spectra of individual QDs (dots correspond to raw data, solid lines to fitted functions obtained by a smoothing filter). The ensemble spectrum is given for reference by the black dashed line.

position is probably the size distribution of the colloidal QDs, which alters the degree of quantum confinement. Hence, roughly half of the observed FWHM of the whole QD ensemble is caused by inhomogeneous broadening. Thus, an optimized chemical synthesis yielding QDs with a sharper size distribution could further narrow the ensemble emission bandwidth. Accordingly, these QDs could show a similar FWHM as their cadmium-based counterparts.

A closer look at the absorption spectra leads to some confusion since such a continuous absorption is typically observed for higher-dimensional systems. In the case of zero-dimensional QDs, continuous absorption should give way to individual peaks as the energy levels and the corresponding transitions become discrete due to the confinement in all three dimensions. To understand this apparent discrepancy, the energetic structure of these QDs will be calculated in the following within the effective mass model introduced in Subsection 2.2.1.

The model of an infinite spherical potential well was used to describe electron and hole states within a core-only QD. This model can be extended by introducing a step in the radial potential $V(r)$ accounting for the shell material (see Equation 4.1).[166]

$$V(r) = \begin{cases} 0 & \text{for } r \leq R_{\text{core}} \\ V_{\text{shell}} & \text{for } R_{\text{core}} < r \leq R_{\text{shell}} \\ \infty & \text{for } R_{\text{shell}} < r \end{cases} \tag{4.1}$$

The height of the potential step (V_{shell}) depends on the energy band alignment between the core and shell materials. InP/ZnS and InP/ZnSe represent a type I semiconductor heterostructure (see Figure 2.9a) and the VB offsets ΔE_{VB} amount to 1.1 eV and 0.57 eV for ZnS and ZnSe, respectively.[97] Using the band gap energies, the CB offsets ΔE_{CB} can be calculated (1.09 eV for ZnS and 0.75 eV for ZnSe). Accordingly, the potential step has a similar height in VB and

CB for both heterostructures. Thus, electron and hole are expected to localize within the core region.

$$r^2R''(r) + 2rR'(r) + \left(\frac{2m^*r^2}{\hbar^2}E - l(l+1)\right)R(r) = 0 \qquad \text{for } r \leq R_{\text{core}} \tag{4.2a}$$

$$r^2R''(r) + 2rR'(r) + \left(\frac{2m^*r^2}{\hbar^2}\big(E - V_{\text{shell}}\big) - l(l+1)\right)R(r) = 0 \qquad \text{for } R_{\text{core}} < r \leq R_{\text{shell}} \tag{4.2b}$$

Using such a step-like potential, the radial part of the Schrödinger equation is given by Equation 4.2 in analogy to Subsection 2.2.1. Similar to the core-only QD, the wave function must be finite at the origin $\big(R(0\,\text{nm}) \neq \infty\big)$ and vanish at the border of the QD $\big(R(R_{\text{shell}}) = 0\big)$. Furthermore, the wave function should be continuous at the core/shell interface and the slopes coming from either side must match according to Equation 4.3 taking into account that the effective masses differ between core and shell materials.[166]

$$\lim_{r \nearrow R_{\text{core}}} \frac{R'(r)}{m_{\text{core}}} = \lim_{r \searrow R_{\text{core}}} \frac{R'(r)}{m_{\text{shell}}} \tag{4.3}$$

Obeying these boundary conditions, the energies and wave functions of the respective quantum states can be calculated. In contrast to the core-only QD calculation in Subsection 2.2.1, $R(r)$ is this time given by a superposition of both spherical Bessel functions. Furthermore, possible energy values can only be determined numerically, which was done using *Wolfram Mathematica 11*.

Figure 4.3 shows the energy level diagram for (a) InP/ZnS and (b) InP/ZnSe QDs along with some radial wave functions ($r^2|R(r)|^2$). The effective masses of charge carriers used for the calculations are given in Table 2.2. Based on Table 3.2, the used QD dimensions equal the average values obtained by analyzing TEM images (InP/ZnS QDs: $R_{\text{core}} = 1.7\,\text{nm}$, $R_{\text{shell}} = 4.5\,\text{nm}$ and InP/ZnSe QDs: $R_{\text{core}} = 1.5\,\text{nm}$, $R_{\text{shell}} = 5.4\,\text{nm}$). For the calculation of the soh states, the potential step was reduced by 0.108 eV accounting for the splitting energy, which arises from the spin-orbit coupling.[47]

The density of hole levels is much higher compared to the one of the electrons. This has already been observed for the core-only QDs and can be explained by the higher hole effective mass and the valence band degeneracy. Furthermore, the density of energy levels increases significantly as soon as energies corresponding to the shell material are reached, especially for the hole. In fact, there are just two electron levels that can be seen as core states in case of the InP/ZnS QD: The wave function of the $1s_e$ state is clearly confined to the core region, whereas the one of the $1p_e$ state indicates that the electron is mainly located at the interface between core and shell. The corresponding energy is close to the bulk CB of the ZnS shell, yet it is slightly below it. In case of the InP/ZnSe QD, the only electron state within the core is $1s_e$.

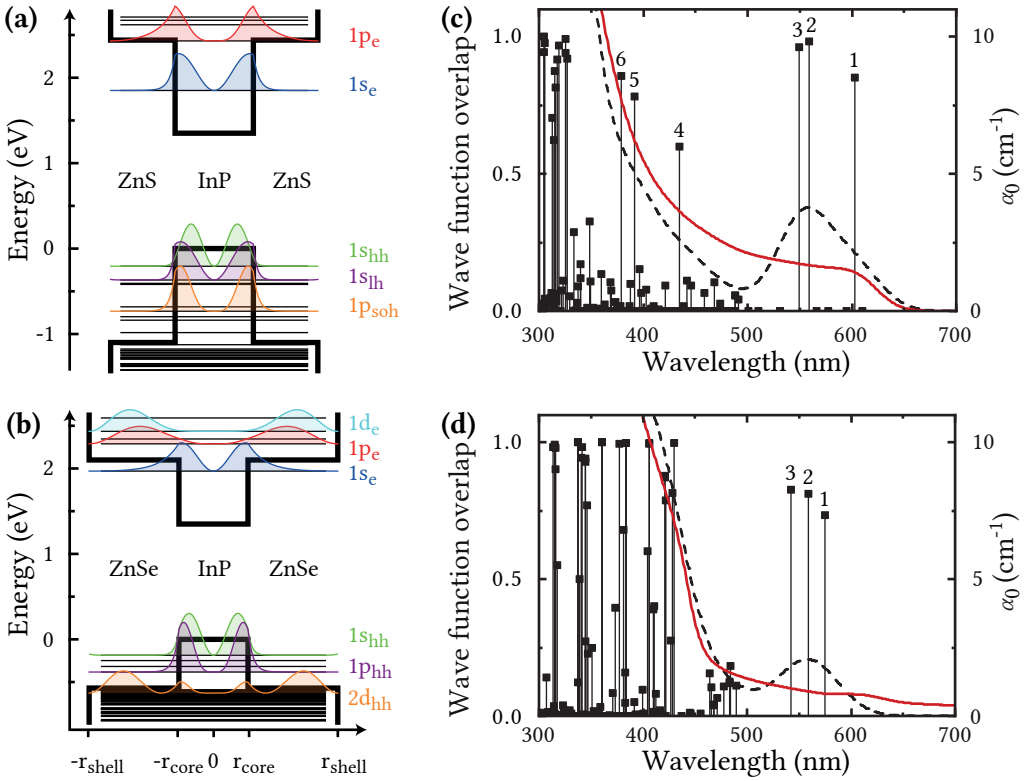

Figure 4.3: Energy Levels of Core/Shell QDs. Energy level diagram of **(a)** InP/ZnS and **(b)** InP/ZnSe QDs obtained by the effective mass model with some wave functions ($r^2|R(r)|^2$) depicted. Calculated wave function overlap ($r^2|\langle R_{nlm}(r)|R_{n'lm}(r)\rangle|^2$) for optically allowed transitions in **(c)** InP/ZnS and **(d)** InP/ZnSe QDs. The most prominent transitions below the band gap of the respective shell material are (1) $1s_e - 1s_{hh}$, (2) $1s_e - 1s_{lh}$, (3) $1s_e - 1s_{soh}$, (4) $1p_e - 1p_{hh}$, (5) $1p_e - 1p_{soh}$, and (6) $1p_e - 1p_{lh}$. For better visualization, each transition was broadened with a Gaussian profile of 25 nm width, which results in the dashed line. The red solid line corresponds to the measured linear absorption coefficient for reference.

To identify possible optical transitions, the wave function overlap between electron and hole states becomes important (see Equation 2.29). This leads to the selection rules introduced in Subsection 2.2.1. For the core-only QD, all quantum numbers (n, l, and m) had to be constant during an optical transition. For the core/shell QD, however, it turns out that these selection rules are a little bit more relaxed. Namely, radial wave functions with different principal quantum number n are no longer orthogonal. Accordingly, Δn can take any integer value, but the wave function overlap strongly reduces for large Δn. Nevertheless, there are many possible optical transitions. The corresponding wave function overlap of them ($r^2|\langle R_{nlm}(r)|R_{n'lm}(r)\rangle|^2$) is shown in Figure 4.3 by the length of the vertical lines (panel (c) represents InP/ZnS and panel (d) InP/ZnSe QDs). At long wavelengths, a few transitions are dominating. At short wavelengths, on the other hand, there are many transitions, which involve states within the shell.

The wave function overlap is proportional to the absorption strength of the respective optical transition according to Fermi's Golden Rule (see Equation 2.8).[95] Furthermore, each

transition has a certain FWHM. In reality, this broadening is very complex and depends on many factors (see Subsection 2.2.2). Nevertheless, a general trend is that higher energetic transitions become broader due to quicker dephasing. For simplicity, a constant broadening on a wavelength axis, which corresponds to an increasing energetic broadening toward shorter wavelengths, will be used in the following. This procedure might be justified given the simplicity of the model in general. Thus, each transition has been broadened by a Gaussian of 25 nm and the sum of all transitions is shown by the dashed line in Figure 4.3c, d. The respective absorption spectrum is given by the red line for reference. While there are some deviations at long wavelengths, both curves match surprisingly well given the simplicity of the model. The remaining deviations between calculation and experiment could probably be decreased if a more detailed model were used (*e. g.*, by including effects due to valence band mixing, pair states, or deviations from spherical symmetry),[92] but this goes beyond the scope of this thesis. In summary, the measured continuous absorption of the QD ensemble can be understood as a consequence of the energetically closely spaced hole levels in combination with large linewidth broadening.

Besides PL peak position and FWHM, the PL QY is an important quantity characterizing the applicability of a material as a light emitter in an LED. To quantify the QY, the QD dispersion must be diluted such that OD(λ_{ex}) = 0.1, in order to minimize disturbing influences (*e. g.*, reabsorption). The QYs of InP/ZnS and InP/ZnSe QDs are 65 % and 40 %, respectively, directly after the dilution process. However, the QY immediately starts to decrease significantly. This trend is shown in Figure 4.4 by the black dots for InP/ZnS QDs. After three days, the QY is only 23 %. In the case of InP/ZnSe QDs, a similar trend can be observed and the QY decreases to 25 % after three days (not shown).

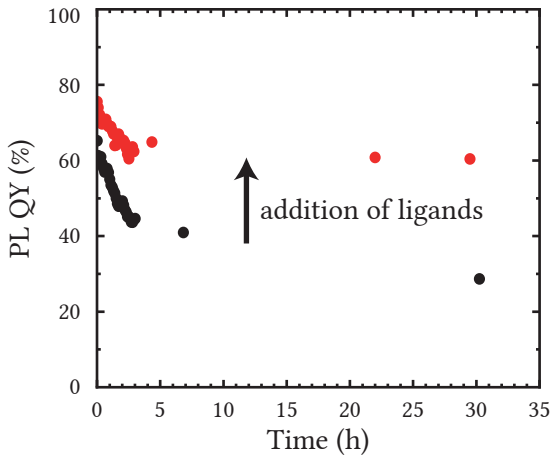

Figure 4.4: Addition of Ligands Enhances the PL QY of InP/ZnS QDs. The PL QY of a QD dispersion was measured as a function of time (black dots). The sample was excited at 470 nm and the concentration of QDs corresponds to OD(470 nm) = 0.1 (cuvette with 1 cm optical path length). If additional ligands (10 µL hexanethiol) were added during the dilution of the highly concentrated QD dispersion, the QY is enhanced and decreases less with time (red dots).

A similar trend has been reported for CdSe QDs and was attributed to surface ligand loss during the dilution process. Interestingly, the emission intensity could be enhanced again if certain ligands were added after some time.[167] Based on this observation, a small amount of ligand molecules (hexanethiol) was added during the dilution process of the QD dispersion investigated here. The effect is shown by the red dots in Figure 4.4. Now, the PL QY of InP/ZnS QDs is initially even 75 % and decreases only slightly within the first few hours until it stabilizes at 60 %.

In a dispersion containing QDs, ligands will attach and detach from the QD surface until an equilibrium is reached.[167] If this dispersion is diluted, the equilibrium will shift toward a scenario where fewer ligands are attached on the surface. Hence, surface defects appear and nonradiative recombination is facilitated, which leads to a lower QY. If ligands are added during the dilution process, the equilibrium shifts less and more ligands stay on the surface. Accordingly, the QY remains high. For all measurements presented in this chapter, ligands were added to the QD dispersion during dilution and the respective measurements were conducted after the QY has stabilized.

Radiative and nonradiative recombination processes determine the lifetime of excited charge carriers. Hence, it is a further important step regarding optoelectronic applications to characterize them. For example, in the case of a long radiative lifetime, unintended processes may impair the efficiency of devices based on these QDs. In order to quantify these recombination processes, the time-resolved PL intensity was recorded after nonresonant photoexcitation at 470 nm. The corresponding signal is shown in Figure 4.5 for (a) InP/ZnS and (b) InP/ZnSe QDs. In both cases, the PL intensity decays over several nanoseconds. The increased noise in the case of InP/ZnSe QDs is caused by the lower PL QY of 36 % compared to 60 % in the case of InP/ZnS QDs. If the data are visualized on a logarithmic y-axis (see

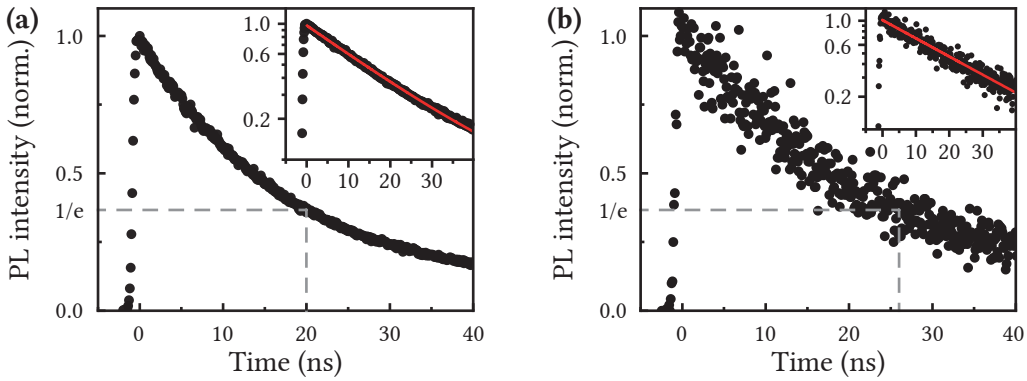

Figure 4.5: PL Decay of QDs in Solution. The concentration of **(a)** InP/ZnS and **(b)** InP/ZnSe QDs in toluene corresponds to OD(470 nm) = 0.08 − 0.09. The sample was excited by a 470 nm LD (900 kHz, 10.5 µW and 21 µW, respectively). The signals were obtained at the emission maximum (620–630 nm). The main panel shows the data on a linear scale, whereas the inset has a logarithmic y-axis. A monoexponential fit of the decay (red line) yields a PL lifetime (1/e-value) of 20 ns for InP/ZnS and 26 ns for InP/ZnSe QDs.

inset), the decay looks linear. This indicates monomolecular recombination of electron-hole pairs, which is expected for zero-dimensional systems. The decay can be reproduced by a monoexponential function (red line) and the corresponding PL lifetimes (1/e-value) are 20 ns for InP/ZnS and 26 ns for InP/ZnSe QDs. (Non-)radiative lifetimes and rates can be calculated using the QY according to Equation 3.12 and are summarized in Table 4.1.

Table 4.1: (Non-)radiative Lifetimes and Rates of InP-Based QDs.

	QY (%)	τ_{PL} (ns)	τ_r (ns)	τ_{nr} (ns)	k_{PL} (ns^{-1})	k_r (ns^{-1})	k_{nr} (ns^{-1})
InP/ZnS	60	20	33	50	0.050	0.030	0.020
InP/ZnSe	36	26	72	41	0.038	0.014	0.025

The radiative lifetime of InP/ZnSe QDs is larger compared to the one of InP/ZnS QDs. This might be caused by the smaller wave function overlap of the relevant sates ($1s_e$, $1s_{hh}$) in the case of InP/ZnSe QDs (see Figure 4.3), which results in a lower transition rate according to Fermi's Golden Rule (Equation 2.8). These findings illustrate that InP/ZnS QDs might be the better candidate for LED applications since the shorter radiative lifetime may reduce the influence of nonradiative processes. Furthermore, InP/ZnS QDs show the higher PL QY.

The time-resolved PL signals discussed above resemble the ensemble average. Since they can be reproduced by a monoexponential function, it is likely that most of the QDs behave in the same way. If there were strong differences between individual QDs a multi-exponential behavior would be expected. Nevertheless, in order to analyze the effect of the

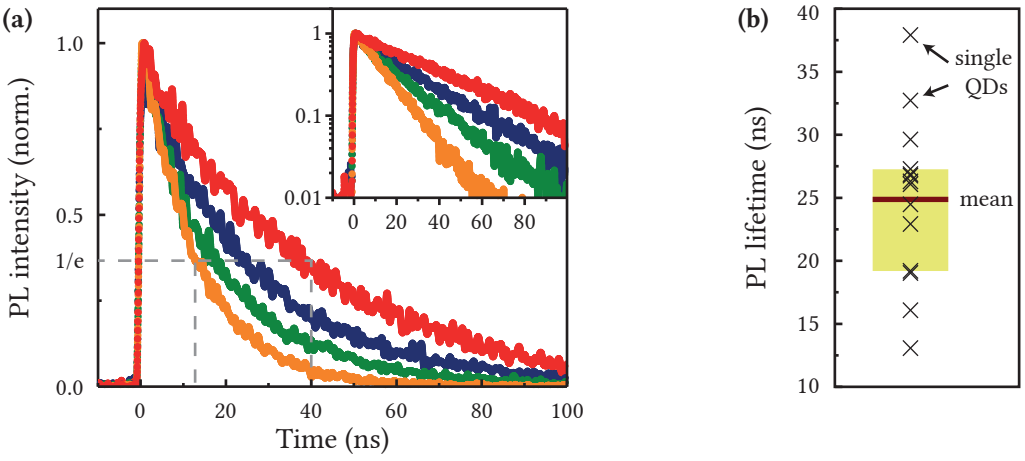

Figure 4.6: PL Decay of Individual InP/ZnS QDs. (a) Single QDs on a silicon substrate were excited at 480 nm (6.49 MHz). The PL decay was recorded without spectral resolution. The shown data represent the full range of observed decay shapes. The main panel shows the data on a linear scale, whereas the inset has a logarithmic y-axis. All QDs show a monoexponential decay. Since the raw data are very noisy, a smoothing filter was applied (low pass Fourier filter), which did not affect the decay shape. **(b)** The PL lifetimes (1/e-value) of 14 QDs obtained by a monoexponential fit are shown as a box plot: The crosses correspond to individual QDs, the average lifetime is (25 ± 7) ns (brown line), and the central range containing 50 % of the data points is highlighted in yellow.

aforementioned sample inhomogeneity in detail, the PL decays of 14 single InP/ZnS QDs were recorded. Figure 4.6a displays the full range of observed signals, which show some variation in the decay time. The crosses in Figure 4.6b correspond to the PL lifetimes (1/e-value) of all investigated QDs. As marked by the brown line, the average lifetime is (25 ± 7) ns, which is only slightly longer compared to the 20 ns of the ensemble measurement. Furthermore, the central range containing 50 % of the data points, which is highlighted in yellow, agrees with the ensemble measurement as well. While most of the QDs show a PL decay comparable to the ensemble signal, the PL decay of some QDs is clearly quicker or slower. Interestingly, all QDs show a monomolecular recombination process. This can be seen in the inset of Figure 4.6a, which has a logarithmic y-axis. Accordingly, the varying lifetimes could thus be a consequence of different contributions from (non-)radiative processes. Since the number of defects may vary from QD to QD, some of them might be more or less prone to nonradiative recombination. Nevertheless, the effect of the sample inhomogeneity on the recombination dynamics is limited as most of the QDs behave in the same way.

4.2 Electron or Hole – Who is Faster?

The general optical performance of InP-based colloidal QDs has been characterized in the previous section. Now, the charge carrier relaxation will be investigated in detail using DT spectroscopy, which is a versatile tool for this purpose (see Subsection 3.2.4 for further details). As the interpretation of DT spectra can be quite complex, InP/ZnS QDs are excited at the optical band gap (λ_{ex} = 600 nm) in the first step. In this case, no significant charge carrier dynamics is expected besides recombination, which will simplify the interpretation of the obtained DT signals. The pump pulse energy is set to allow for, at maximum, only one excited electron–hole pair on each QD in order to avoid multi-carrier effects (*e. g.*, Auger process). To this end, the number of QDs in the excitation volume and the number of absorbed photons were estimated (see Subsection 3.1.3 for details). The obtained DT signal is shown in Figure 4.7 for pump-probe time delays up to 100 fs. A spectrum showing two positive peaks uniformly rises. The main peak is located at 600 nm, which matches the onset of the absorption spectrum shown by the gray area. The second smaller peak appears at shorter wavelengths around 540 nm.

A positive DT signal means that the transmission at the respective wavelength has increased. This can be explained by state filling since the presence of excited charge carriers reduces the number of available initial/final states for optical transitions and, thus, enhances the transmission. Accordingly, state filling is expected to be the dominant mechanism causing the DT signal. This assignment is also in agreement with former reports on cadmium-based QDs.[155,168] It should be noted that the term *state filling* is preferred compared to the typically used term *phase space filling* as it emphasizes the discrete nature of the energetic structure of

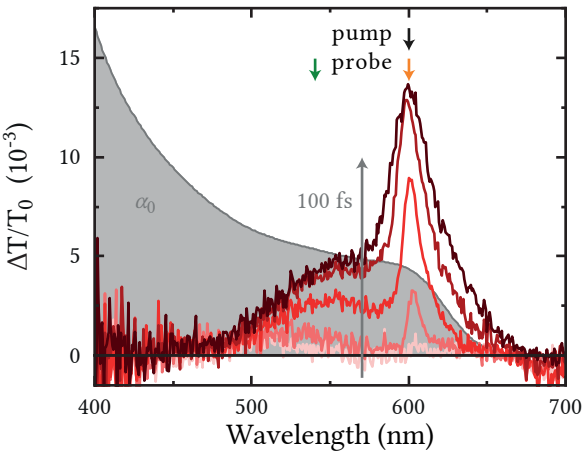

Figure 4.7: Resonant Excitation of InP/ZnS QDs. Temporal evolution of the DT spectrum after photoexcitation at 600 nm (pulse energy 200 nJ). The gray area corresponds to the linear absorption spectrum as reference. The QDs were dispersed in toluene in a cuvette with an optical path length of 2 mm at a concentration that equals an OD of 0.3 at the absorption onset.

QDs. Since the change in the transmission is only weak ($\frac{\Delta T}{T_0} \ll 1$), the signal is interpreted to be directly proportional to the sum of the Fermi distributions at the electron and hole states relevant for the respective transition (see Equation 3.17). It should be noted that the Fermi distribution refers to the average value of the QD ensemble, a certain state of an individual QD is either occupied or not.

As shown in Figure 4.8a, the DT spectrum can be reproduced by two Gaussian peaks, which are located at 540 nm and 600 nm, respectively. The corresponding energetic distance of 230 meV matches perfectly with the energetic gap between the $1s_{hh}$ and the next energetically higher lying $1s_{lh}$ and $1s_{soh}$ states based on the calculation in the previous section. These higher energetic hole states are located at nearly the same energy and, for convenience, are referred to as $1s_{lh/soh}$ in the following.

Based on the considerations above, both DT signals are related to the transitions shown in Figure 4.8b. The main peak at 600 nm (orange) is assigned to the $1s_e - 1s_{hh}$ transition, which is named *transition I* in the following. The signal is caused by state filling, where probably both charge carriers, electron and hole, contribute, as they have been resonantly excited to the respective states.

The weaker signal at 540 nm (green) is attributed to the $1s_e - 1s_{lh/soh}$ transition, which is named *transition II* in the following. Notably, the higher energetic $1s_{lh/soh}$ state has not been populated during excitation. Furthermore, it is unlikely that a hole, which was excited to the $1s_{hh}$ state, thermally occupies this state since the thermal energy at room temperature is much less than the energetic spacing of both states ($k_B T = 25\,\text{meV} \ll 230\,\text{meV}$). Thus, the

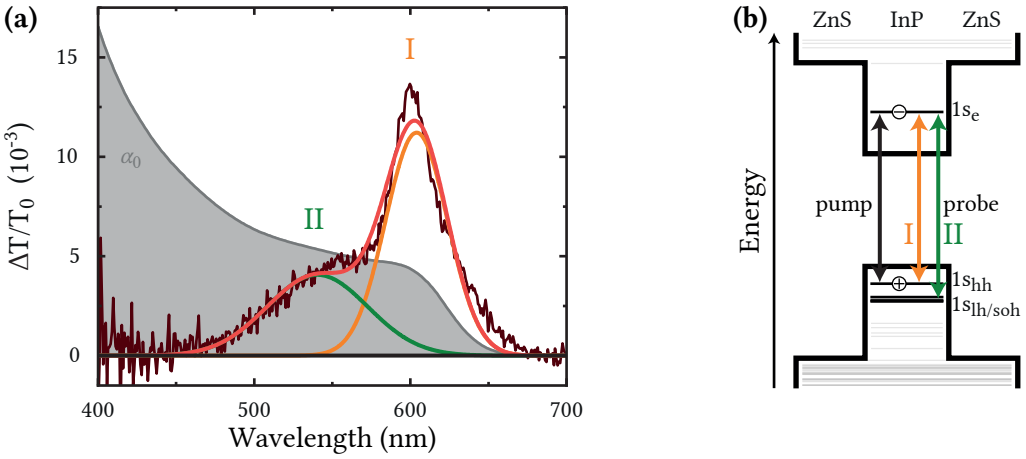

Figure 4.8: Interpretation of the DT Spectrum. **(a)** The brown curve is the same as in Figure 4.7 at a pump-probe delay of 100 fs. The spectrum can be reproduced by the sum of two Gaussian peaks located at 540 nm (green) and 604 nm (orange) with an FWHM of 76 nm (green) and 47 nm (orange). The red line shows the sum of both peaks. **(b)** After resonant excitation (black arrow), electron and hole occupy the $1s_e$ and $1s_{hh}$ states, respectively. The DT signal at 600 nm (orange peak) is attributed to state filling of the $1s_e - 1s_{hh}$ transition (orange arrow) by both charge carriers. The higher energetic signal at 540 nm (green peak) is associated with partial state filling by the electron of the $1s_e - 1s_{lh/soh}$ transition (green arrow).

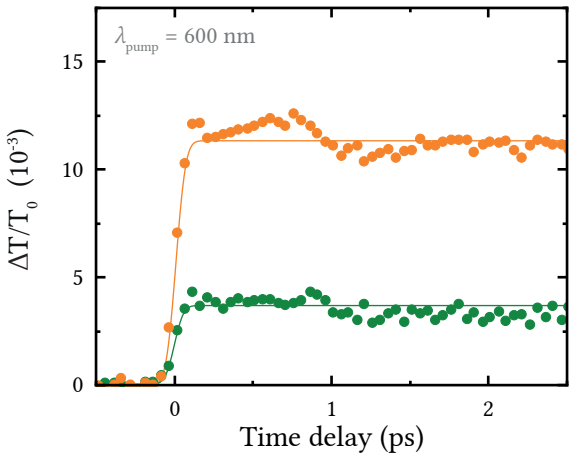

Figure 4.9: Step-Like Signal after Resonant Excitation. The sample was excited at 600 nm (see Figure 4.7). The temporal evolution of the DT signals at probe wavelengths of 540 nm (green dots) and 600 nm (orange dots) shows a step-like behavior. The solid lines are a fit to the data (see main text).

hole cannot contribute to the state filling of transition II and only the electron occupies a state relevant for this transition ($1s_e$). Accordingly, the DT signal is interpreted as *partial* state filling caused by the electron.

The DT signal at both transitions is shown in Figure 4.9 as a function of the time delay between the pump and probe laser pulses. A maximum is reached within ~200 fs and both signals remain roughly constant afterwards. Since the recombination of charge carriers takes place on a much longer time scale compared to the depicted picosecond range, it makes sense that both signals remain constant after the initial rise. Therefore, effects due to the recombination of charge carriers can be neglected. The very short rise time of these step-like signals can be related to the laser pulse width of $\tau_{\text{laser}} = 80$ fs. The temporal overlap of pump and probe laser pulses yields an IRF given by Equation 4.4, where $\Delta t = \sqrt{2}\tau_{\text{laser}}$.

$$\text{IRF}(t) = \sqrt{\frac{4\ln(2)}{\pi \Delta t^2}} \exp\left(-4\ln(2)\frac{t^2}{\Delta t^2}\right) \tag{4.4}$$

Thus, both signals can be reproduced (solid lines) using the convolution of a step function with IRF(t) as stated in Equation 4.5, where $\Theta(t)$ is 0 for negative t and 1 for positive t. The obtained width $\Delta t = (110 \pm 20)$ fs matches with the expected time resolution of the experimental setup ($\Delta t = \sqrt{2}\tau_{\text{laser}} = 113$ fs). This instrument-related effect is taken into account for all further time scales.

$$f_{\text{step}}(t) = A\Theta(t) * \text{IRF}(t) = \int_{-\infty}^{\infty} A\Theta(T)\,\text{IRF}(t-T)\,dT \tag{4.5}$$

In the following, electron and hole will initially receive excess energy with respect to the energetically lowest states by exciting the QDs at shorter wavelengths. Hence, it is possible to investigate the electron and hole relaxation dynamics by analyzing how the DT signal

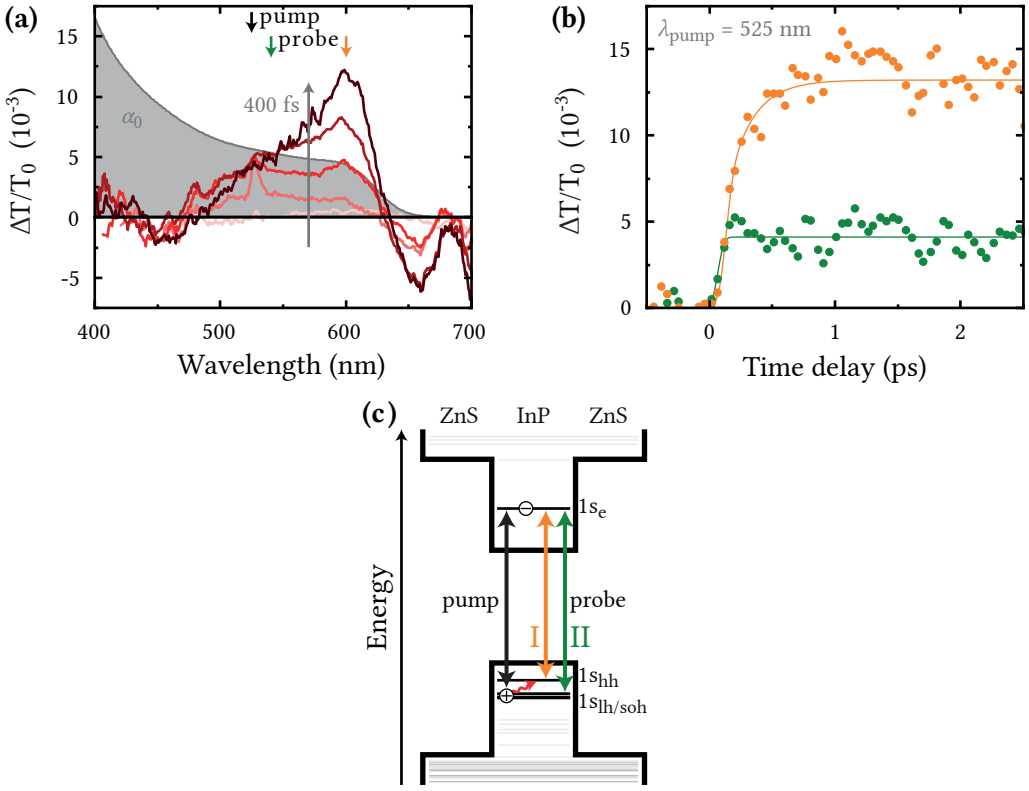

Figure 4.10: Observation of Hole Relaxation. (a) Temporal evolution of the DT spectrum after photoexcitation of InP/ZnS QDs at 525 nm (pulse energy 225 nJ). The gray area corresponds to the linear absorption spectrum for reference. The QDs were dispersed in toluene in a cuvette with an optical path length of 2 mm at a concentration that equals an OD of 0.3 at the absorption onset. **(b)** Dynamics at probe wavelengths of 540 nm (green dots) and 600 nm (orange dots). The solid lines are a fit to the data (see main text). **(c)** After photoexcitation (black arrow), electron and hole occupy the $1s_e$ and $1s_{lh/soh}$ states, respectively. Hence, the hole will relax to the $1s_{hh}$ state (red wavy arrow), which leads to the gradually increasing signal observed in panel (b).

builds up over time. First, the QDs are excited by a laser at 525 nm to pump transition II. Thus, the hole receives a small amount of excess energy with respect to the $1s_{hh}$ state, whereas the electron still occupies the $1s_e$ state. To ensure that only transition II and not the lower energetic transition I is excited, the pump wavelength is intentionally slightly blueshifted compared to the maximum of transition II at 540 nm, but well within its FWHM. The observed rise of the DT signal is shown in Figure 4.10a for a pump-probe time delay of up to 400 fs. As before, the spectrum shows both transitions I and II. However, the temporal evolution of the spectra is different compared to the resonant excitation of the transition I discussed before. The DT signals at the probe wavelengths corresponding to the transitions I and II are shown in Figure 4.10b as a function of the time delay between the pump and probe laser pulses. The signal of the resonantly excited transition II (green dots) resembles the same step-like rise as observed before. The signal of transition I, on the other hand, shows a different trend as it rises now gradually (orange dots). As illustrated in Figure 4.10c by the red arrow, this can be explained by the holes that were initially excited to the $1s_{lh/soh}$ state and subsequently

relax to the $1s_{hh}$ state, which leads to a gradually increasing state filling (on average over all QDs) causing the signal at transition I. The subsequent evolution of both signals appears to be nearly constant, as it has already been observed for the resonant excitation of transition I. It should be noted that the contribution of holes to the state filling at transition I, which is observed here, was questioned for a long time in case of cadmium-based QDs, since the hole might also occupy close-lying but optically dark states.[155] However, a recent publication on cadmium-based QDs shows that the hole indeed contributes to the signal.[169]

As discussed above, the signal at transition I looks as expected for the intended hole relaxation process. However, one might predict a decreasing signal at transition II after the initial rise due to holes leaving the $1s_{lh/soh}$ state, which should reduce the state filling. Interestingly, such a feature is not observed. This can be explained by the small energetic spacing and degeneracy of the higher energetic hole states. Their close proximity allows for a distribution of the hole occupation probability over adjacent states. Some of them are even involved in an optically dark transition with the $1s_e$ state. Therefore, the state filling contribution of the hole to the signal at transition II is strongly reduced or even negligible, although the hole is resonantly excited to the respective state.[170] Consequently, the signal at transition II (green) is a direct measure of the electron population of the $1s_e$ state.

In contrast to transition II, the signal at transition I (orange dots) stems from both charge carriers: the electrons, which are resonantly excited to the $1s_e$ state, and the holes that relax to the $1s_{hh}$ state with time. Thus, the rise of this signal can be modeled by Equation 4.6, which corresponds to the sum of a step function (representing the resonantly excited electrons) and an exponentially rising function (corresponding to the arriving holes).

$$f_{\text{biexp. rise}}(t) = A\Theta(t)\left[B + (1-B)\left(1 - \mathrm{e}^{-\frac{t}{\tau}}\right)\right] * \mathrm{IRF}(t) \tag{4.6}$$

The free parameters of this model are the rise time τ of the monoexponential function and the relative contribution B of electron and hole to the signal. It appears that a 50:50 ratio ($B = 0.5$) leads to the best reproduction of the experimental data (orange solid line in Figure 4.10b). Using this value, a rise time of (200 ± 50) fs can be deduced. Thus, this time scale can be ascribed to the hole relaxation time from the $1s_{lh/soh}$ to the $1s_{hh}$ state, as illustrated by the red arrow in Figure 4.10c. This is an extremely fast process, given that an energetic spacing of the two levels of 230 meV, which is more than five times the energy of an LO phonon in bulk InP (43 meV),[161] should result in a phonon bottleneck (see Subsection 2.2.3). Apparently, the closely spaced optically inactive hole levels still permit rapid relaxation.

Since electron and hole contribute differently to the DT signals at both transitions, it is possible to differentiate between them. With this ability, a scenario where both charge carriers initially receive excess energy will be investigated in the following. To this end, the QDs are excited by a laser at 400 nm. As sketched in Figure 4.11a by the black arrow, this

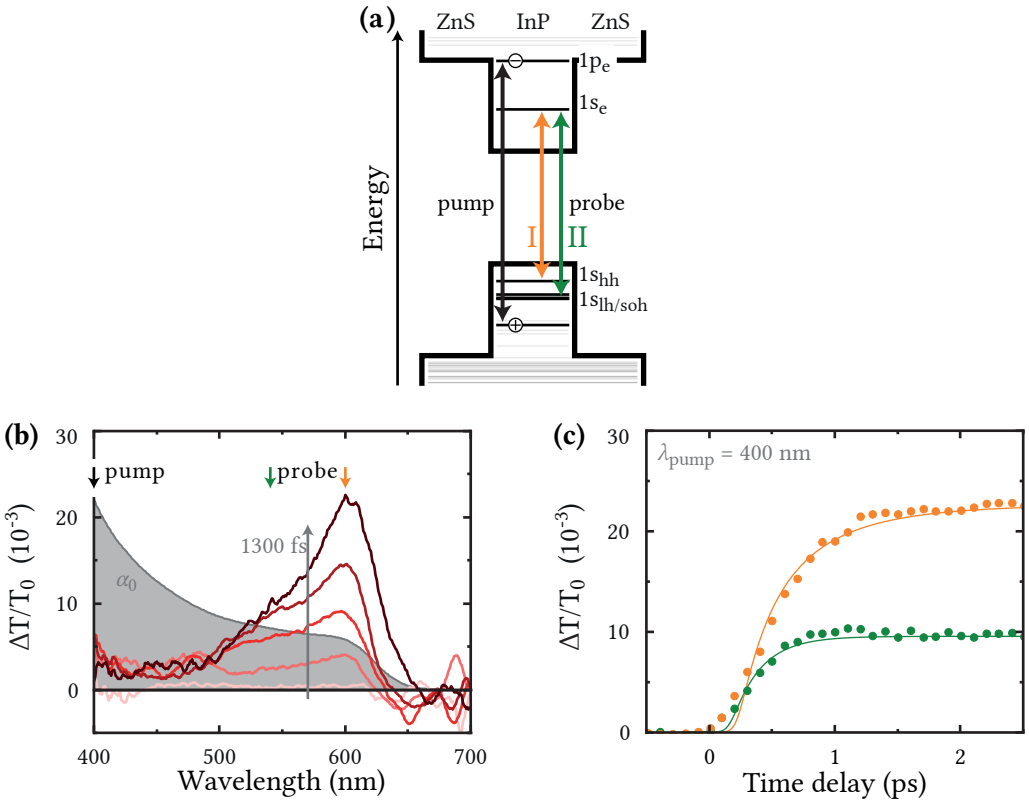

Figure 4.11: Fast Electron Relaxation. **(a)** Schematic illustration of the relevant electronic transitions. **(b)** Temporal evolution of the DT spectrum after photoexcitation of InP/ZnS QDs at 400 nm (pulse energy 145 nJ). The gray area corresponds to the linear absorption spectrum as reference. The QDs were dispersed in toluene in a cuvette with an optical path length of 2 mm at a concentration that equals an OD of 0.22 at the absorption onset. **(c)** Dynamics at probe wavelengths of 540 nm (green dots) and 600 nm (orange dots). The solid lines are a fit to the data (see main text).

corresponds to a transition between the second electron state ($1p_e$) and one of the higher energetic hole states (*e. g.*, $1p_{lh}$ or $1p_{soh}$). During excitation, roughly 1 eV of excess energy is delivered to the excited electron–hole pair with respect to transition I. Comparing this value with the excess energy of the previous scenario (230 meV), a much slower relaxation is this time expected, especially for the electron owing to a suspected strong phonon bottleneck. The observed DT spectra are shown in Figure 4.11b for a pump-probe time delay up to 1300 fs. While the spectra resemble the known shape, the rise of the signal takes indeed significantly longer compared to the scenarios discussed before. Figure 4.11c shows the temporal evolution of the signal at both probe wavelengths, which correspond to transitions I and II. Both signals show a considerably longer rise time compared to the previous cases.

As before, the signal at transition II (green dots) can be related to the electron population of the $1s_e$ state. Using Equation 4.7, it can be reproduced by an exponentially rising function

(green solid line) representing the electron arrival.

$$f_{\text{exp. rise}}(t) = A\Theta(t)\left(1 - \mathrm{e}^{-\frac{t}{\tau}}\right) * \mathrm{IRF}(t) \tag{4.7}$$

Hence, the corresponding time scale of (230 ± 20) fs can be related to the electron relaxation time from the $1p_{\mathrm{e}}$ to the $1s_{\mathrm{e}}$ state. As the energetic gap between the electron states is roughly 580 meV, a strong phonon bottleneck was expected. Therefore, this fast time scale is a counterintuitive and surprising result. Actually, the electron relaxation time is comparable to the hole relaxation time observed in the previous scenario. In that case, phonon scattering could explain the observed fast relaxation. Here, however, with no additional states between the two electron levels, phonon scattering should be strongly impeded. This apparent conflict will be discussed in detail in the next section. But before that, a closer look at the signal of transition I (orange dots) should be taken.

The signal at transition I is caused by the increasing state filling due to the arrival of both charge carriers. Accordingly, it can be modeled by a biexponential function (Equation 4.8) representing the arrival of electron and hole, respectively.

$$f_{\text{biexp. rise}}(t) = A\Theta(t)\left[B\left(1 - \mathrm{e}^{-\frac{t}{\tau_1}}\right) + (1-B)\left(1 - \mathrm{e}^{-\frac{t}{\tau_2}}\right)\right] * \mathrm{IRF}(t) \tag{4.8}$$

As already determined, the time scale of the electron relaxation can be fixed to a value of 230 fs. Based on this, the data can be well reproduced (orange solid line). The ratio of electron and hole contribution to the signal does not affect the result strongly. Consequently, as before, this ratio is fixed to 50:50. Thus, the hole relaxation time is found to be (600 ± 40) fs, which is three times longer than the hole relaxation from $1s_{\mathrm{lh/soh}}$ to $1s_{\mathrm{hh}}$ observed in the previous scenario and significantly longer than the electron relaxation discussed above. Accordingly, the surprising conclusion is that the electron relaxes faster than the hole despite the large energetic gap between the corresponding electron levels. An explanation for this intriguing observation will be given in the following section.

4.3 Auger Speeds Up the Electron

It has already been proposed for cadmium-based QDs that electron-hole scattering is an efficient Auger-like process.[103] During such an event, the electron transfers its excess energy to the hole, which thus occupies an even higher energetic state as sketched in Figure 4.12 by the brown arrows. Notably, no third particle participates in the scattering process, which would be the case for a typical Auger process. While the scattering process could also take place in favor of a hole relaxation, it is much more likely that the electron relaxes. This is caused by the larger number of final states to which the hole might scatter, in contrast to

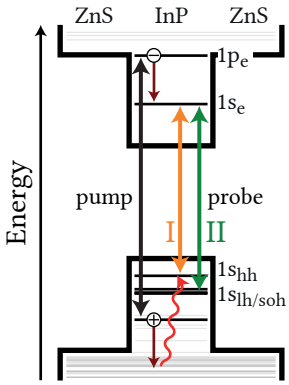

Figure 4.12: Auger-Like Process Leading to Fast Electron Relaxation. Schematic illustration of the Auger-like electron–hole scattering event as straight brown arrows and the subsequent hole relaxation by phonon scattering as a red wavy arrow.

the few higher energetic electron levels above the $1p_e$ state which still show a significant energetic spacing. This mechanism explains the rapid relaxation of the electron from the $1p_e$ to the $1s_e$ state even though the energetic gap between the states is large. The hole, on the other hand, has now to dissipate an even larger amount of excess energy by phonon scattering as the only scattering process available (shown by the red wavy arrow). Thus, its relaxation takes longer.

So far, both charge carriers were always excited to states energetically within the QD core. As a next step, the relaxation of charge carriers from the shell into the core will be investigated. In the case of InP/ZnS QDs, more than 3.54 eV are required to excite an electron hole-pair within the ZnS shell. This requires a laser wavelength of ≤ 350 nm. While the used OPA can deliver such wavelengths, the white-light generated within the CaF_2 crystal and serving as the probe beam has no significant intensity at such short wavelengths. Hence, InP/ZnSe QDs are used for the following experiment, since a laser wavelength of 400 nm is sufficient to excite an electron-hole pair within the ZnSe shell.

The obtained DT signal is more complex than the one of the scenarios discussed before. It is shown in Figure 4.13a as a color map for a pump-probe time delay up to 10 ps. Two strong positive signals can be observed. The first one appears at the optical band gap and can, thus, be identified with the known transition I. The second signal is located at shorter wavelengths. Within 1–2 ps after photoexcitation, this signal shifts from 400 nm to 450 nm and an intensity maximum is reached after ~400 fs. This observation is comparable to the signal caused by the relaxation of excited charge carriers down to the band gap of a bulk material.[171] As can be seen in Figure 4.13d, the hole levels with energies corresponding to the shell are very dense, which leads to this bulk-like behavior. Subsequently, this signal stays at 450 nm and slowly decays, whereas the signal at 600 nm increases in intensity. The signal at 450 nm can be related to (partial) state filling of the energetically lowest transition within the ZnSe shell. This transition is sketched in Figure 4.13d by the blue arrow and termed *transition III* in the

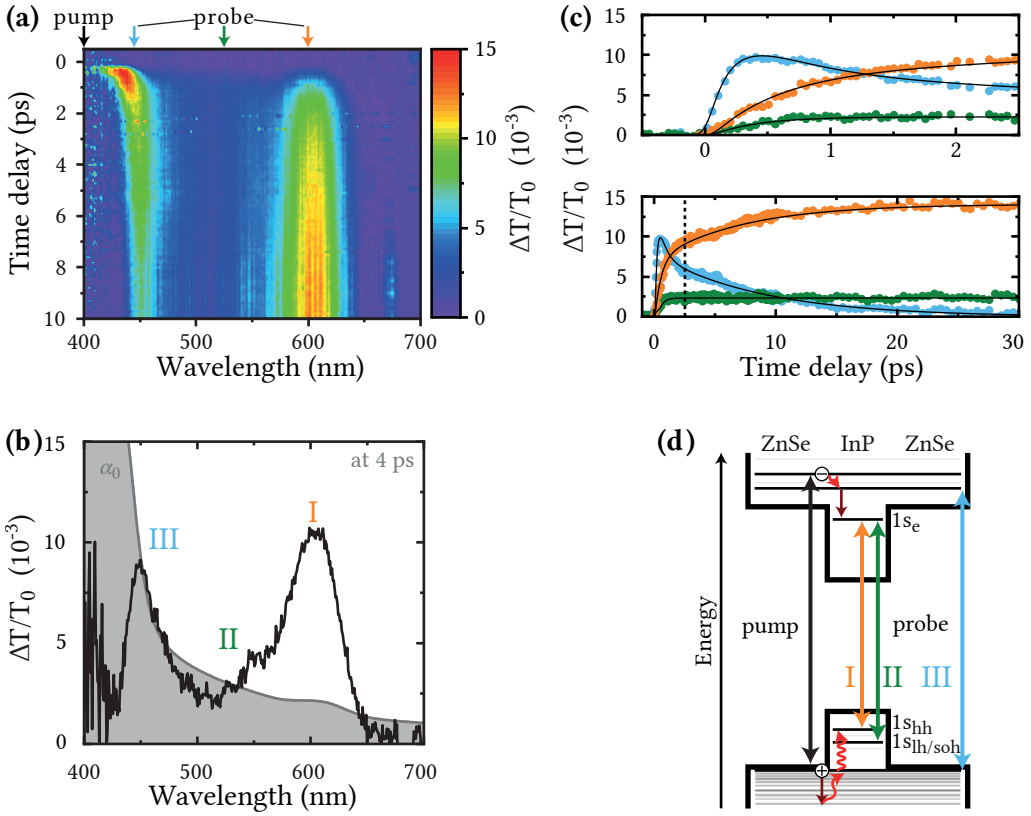

Figure 4.13: Charge Carrier Relaxation from Shell to Core. **(a)** Color map showing the temporal evolution of the DT spectrum after photoexcitation of InP/ZnSe QDs at 400 nm (pulse energy 50 nJ). The QDs were dispersed in toluene in a cuvette with an optical path length of 2 mm at a concentration that equals an OD of 0.1 at the absorption onset. **(b)** A representative DT spectrum taken from panel (a) at a time delay of 4 ps between the pump and probe laser pulses. The gray area corresponds to the linear absorption spectrum as reference. **(c)** Dynamics at probe wavelengths of 450 nm (blue dots), 525 nm (green dots), and 600 nm (orange dots). The solid lines are a fit to the data (see main text). **(d)** Schematic illustration of the relevant electronic transitions, the Auger-like electron–hole scattering event as straight brown arrows, and the hole relaxation by phonon scattering as a red wavy arrow.

following. Figure 4.13b shows a representative DT spectrum corresponding to a pump-probe time delay of 4 ps. Besides the signals at 450 nm and 600 nm, a broad shoulder in between can be identified (525 nm). As sketched in Figure 4.13d, this signal can be related to the known transition II involving a higher energetic hole state and the lowest electron state.

The dynamics at these three probe wavelengths are shown in Figure 4.13c. Similar to the InP/ZnS QDs discussed before, the recombination of charge carriers in InP/ZnSe QDs takes place on a nanosecond time scale and should not influence the fast relaxation dynamics discussed here. The signal at transition II (green) rises within the first picosecond and then stays constant. As this signal is only caused by the presence of electrons on the $1s_e$ state, this signal can again be modeled by an exponential function (Equation 4.7) representing the arrival of electrons at the $1s_e$ state, which yields an electron relaxation time of (370 ± 40) fs. This time scale is longer compared to the electron relaxation time of 230 fs obtained for the

InP/ZnS QDs discussed before. Interestingly, the energetic difference of the involved electron levels is smaller in InP/ZnSe QDs (420 meV compared to 580 meV in InP/ZnS QDs). As before, the signal of transition I (orange) reflects both, electron and hole arrival at the $1s_e$ and $1s_{hh}$ states. As can be seen by the solid line in panel (c), the signal can be again well reproduced by a biexponential function, where both components contribute equally (Equation 4.8). The obtained rise times are (520 ± 40) fs and (7.1 ± 0.3) ps. The 520 fs rise time is in reasonable agreement with the 370 fs obtained from the analysis of transition II and, therefore, explained by the electron relaxation. The remaining 7.1 ps can thus be related to the hole relaxation time, which appears to be an order of magnitude slower compared to the hole relaxation in the InP/ZnS QDs investigated previously. Finally, as shown by the blue dots in Figure 4.13c, the signal of transition III rises more or less instantaneously and then decays on two time scales to zero. This can be ascribed to the disappearance of electrons and holes from the shell states involved in the respective transition, which results in a reduced state filling. A biexponential fit (solid line) yields (510 ± 140) fs and (8.8 ± 0.3) ps using Equation 4.9. Again both components contribute equally.

$$f_{\text{biexp. decay}}(t) = A\Theta(t)\left(B\mathrm{e}^{-\frac{t}{\tau_1}} + (1-B)\,\mathrm{e}^{-\frac{t}{\tau_2}}\right) * \mathrm{IRF}(t) \tag{4.9}$$

These time scales are in good agreement with the ones of electron and hole relaxation obtained by the previous analysis of transitions I and II. Thus, the interpretation of the various signals is consistent and reveals two distinct time scales for the electron and hole relaxation from the shell into the core within InP/ZnSe QDs. In case of the electron, the analysis of the DT signals at the three probe wavelengths resulted in relaxation times of 370 fs, 520 fs, and 510 fs, respectively, which yields an average value of 470 fs. In case of the hole relaxation, the analysis of the DT signals at transitions I nd III resulted in much longer relaxation times of 7.1 ps and 8.8 ps, respectively, which yields an average value of 8 ps.

Again, the electron relaxes much faster than the hole, which can be explained by the Auger-like scattering mechanism as before. This is indicated by the brown arrow in Figure 4.13d. However, the relaxation time scales of both charge carriers are significantly longer compared to the previous case of InP/ZnS QDs, while the initial excess energy is comparable. In order to understand the longer relaxation time scales, a closer look at the energetic structure of the QDs is needed. In case of InP/ZnS QDs, the excited electron and hole still occupied states related to the core, whereas, for the InP/ZnSe QDs, the excited charge carriers occupied states that are associated with the shell. Accordingly, a large part of the spatial probability distribution characterized by the wave function lies outside the core material (see Figure 4.3b). Therefore, the wave function overlap with states in the core is strongly reduced, and according to Fermi's Golden Rule, this leads to a slower relaxation.

4.4 Auger Scenario and Hole Trapping Explains Quantum Yield

Up to know, only the dynamics of the DT signal was analyzed, which revealed the charge carrier relaxation time scales as a function of the initial excess energy. However, further insight can be obtained when focusing on the spectral shape of the DT signal after the charge carrier relaxation took place. Specifically, the ratio of the DT signals at transitions I and II can be used to characterize the relaxation efficiency of charge carriers as described in the following.

Based on the findings in the previous sections, the signal of transition I is proportional to the Fermi distribution of both, electron (f_{1s_e}) and hole ($f_{1s_{hh}}$), whereas the signal of transition II is simply proportional to the state filling by the electron (f_{1s_e}). Accordingly, the above-mentioned ratio can be represented according to Equation 4.10.

$$\frac{\frac{\Delta T}{T_0}(600\,\mathrm{nm})}{\frac{\Delta T}{T_0}(540\,\mathrm{nm})} = \frac{f_{1s_e} + f_{1s_{hh}}}{f_{1s_e}} = 1 + \frac{f_{1s_{hh}}}{f_{1s_e}} \tag{4.10}$$

Assuming that fewer electrons (on average over all QDs) arrive at the $1s_e$ state, f_{1s_e} decreases and therefore the ratio increases. On the other hand, if fewer holes relax to the $1s_{hh}$ state, $f_{1s_{hh}}$ reduces and thus the ratio decreases. Hence, variations of this ratio for different excitation scenarios can hint toward a varying charge carrier relaxation efficiency.

Indeed, small variations of this ratio can be observed when comparing the different excitation scenarios of InP/ZnS QDs discussed in the previous sections. In case of the resonant excitation at 600 nm, the ratio of the signals corresponding to transitions I and II is 3 (see Figure 4.9). This is still the case for the excitation with slight excess energy at 525 nm (see Figure 4.10b). However, for the excitation with the pump laser set to 400 nm, the ratio decreases to 2.5 (see Figure 4.11c). Accordingly, the ratio decreases with increasing excess energy, which means that fewer holes arrive at the $1s_{hh}$ state.

The decreasing hole relaxation efficiency with increasing excess energy can be explained by a hole trapping process. As sketched in Figure 4.14, the hole occupies a high energetic state directly after the Auger-like process took place. Since the subsequent relaxation takes time due to the phonon bottleneck, the hole may become trapped on a defect state (indicated by the blue arrow). Since the hole relaxation from the $1s_{lh/soh}$ to the $1s_{hh}$ state is not affected, these traps may lie energetically above the $1s_{lh/soh}$ state. The trap states might be caused by an imperfect core/shell interface or dangling bonds on the surface of the QD. Possibly, the hole leaves the trap state after some time, thus, eventually arriving at the $1s_{hh}$ state. This may also explain the long hole relaxation times obtained in the previous sections. However, trapped

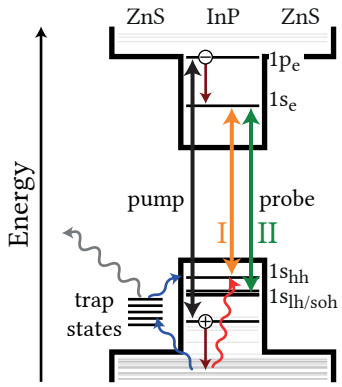

Figure 4.14: Trapping of Holes. Schematic illustration of the Auger-like electron–hole scattering event by the straight brown arrows, the hole relaxation by phonon scattering marked by a red wavy arrow, the hole (de-)trapping process indicated by the blue wavy arrows, and nonradiative recombination by a gray wavy arrow.

charge carriers are prone to nonradiative recombination, which is a competing process (gray arrow). Thus, the trapping process can lead to non-emitting QDs.

This in turn implies that less emission of the QD ensemble is expected if they are excited with large excess energy. Indeed, the PL QY decreases significantly for excitation wavelengths shorter than 500 nm, as can be seen in Figure 4.15. This is in good agreement with the decreasing relaxation efficiency of holes for increasing excess energy, which was deduced from the DT measurements.

As discussed in Subsection 3.2.1, a simple measure for the relaxation efficiency of charge carriers can be obtained by comparing absorption and PLE spectra. According to Equation 3.5, the ratio of the PLE intensity with respect to the OD is proportional to the PL QY. This is, in turn, given by the product of the excitation wavelength-dependent charge carrier relaxation efficiency $\eta_{\mathrm{relax}}(\lambda_{\mathrm{ex}})$ and the constant recombination efficiency η_{recomb} of charge carriers at

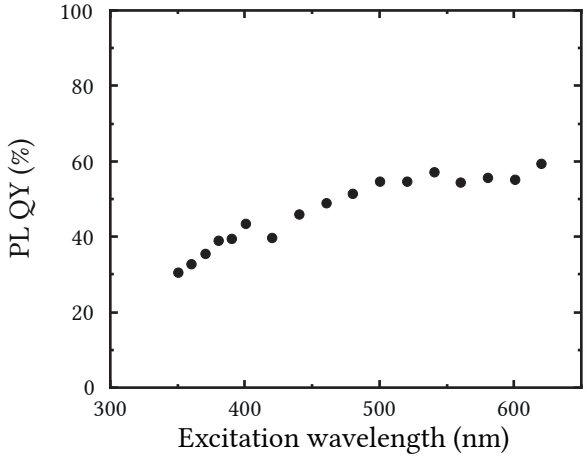

Figure 4.15: Reducing PL QY with Increasing Excess Energy. The PL QY of InP/ZnS QDs in toluene as a function of the excitation wavelength. For each measurement, the concentration of QDs was adjusted to yield $\mathrm{OD}(\lambda_{\mathrm{ex}}) = 0.1$.

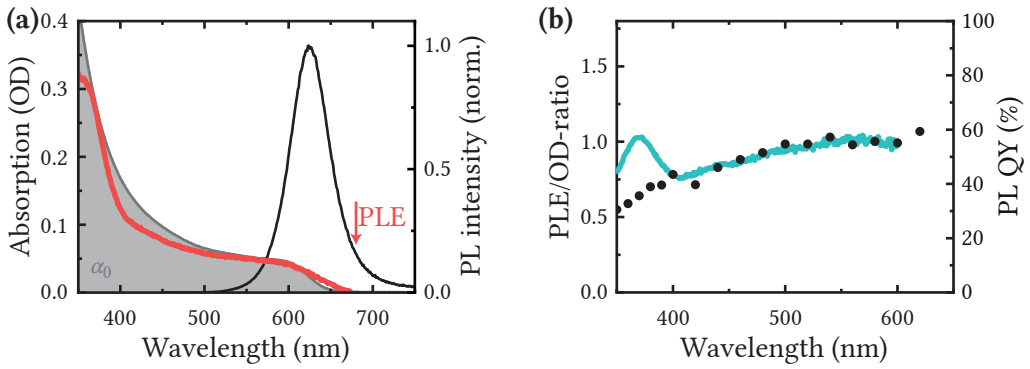

Figure 4.16: PLE, Absorption and the Relaxation Efficiency. (a) The absorption spectrum of InP/ZnS QDs dispersed in toluene is given by the gray area. The black line corresponds to the PL spectrum (λ_{ex} = 470 nm), whereas the red line shows the PLE spectrum (λ_{em} = 680 nm). **(b)** The ratio between PLE and absorption is shown by the blue line. It is proportional to the PL QY in the wavelength range from 400 nm to 600 nm (black dots).

the emitting transition. It should be noted that this procedure does not allow to distinguish between electrons and holes. Furthermore, it does not give an absolute value, but only a relative trend of the relaxation efficiency of charge carriers as a function of the excitation wavelength. Nevertheless, this method is applied in the following to check for consistency with the previous results.

Figure 4.16a shows again the absorption and PL spectrum of InP/ZnS QDs (gray area and black line, respectively) along with the PLE spectrum obtained at an emission wavelength of 680 nm, which was normalized to match the absorption onset. The PLE spectrum resembles the absorption spectrum very well. However, there are small deviations at wavelengths shorter than 500 nm. The ratio of the PLE signal with respect to the OD is shown in Figure 4.16b by the blue line and is a measure of the charge carrier relaxation efficiency. For reference, the PL QY is shown by the black dots. Notably, both data sets match perfectly in the wavelength range of 400–600 nm. Only for shorter wavelengths, they differ significantly. The deviations might be related to the sample inhomogeneity since the QY measurement and the absorption spectrum represent the whole QD ensemble, whereas the PLE spectrum corresponds to a subset of QDs emitting at the specific wavelength. Nevertheless, this procedure shows the consistency of the data and allows to characterize the charge carrier relaxation efficiency for excitation wavelengths of 400–600 nm. This quantity is constant above 500 nm and decreases by roughly 25 % toward 400 nm.

In summary, these results may be helpful for the fabrication of future LEDs harnessing QDs as direct light emitters. They demonstrate that it is crucial to inject charge carriers energetically close to the states leading to emission. To this end, the energetic alignment of charge transport and injection layers should be optimized. Thus, a slow hole relaxation leading to trapping can be circumvented and high radiative efficiency can be reached.

5

$Cs_2AgBiBr_6$ Double Perovskite: Interplay of Bound Excitons and Intervalley Scattering

In this chapter, $Cs_2AgBiBr_6$ NCs are investigated as one of the potential alternatives to the established lead-based perovskites. They are a member of the new group of DPs.[29,172–177] Interestingly, $Cs_2AgBiBr_6$ has an indirect band gap, which gives rise to substantially different properties compared to lead-based perovskites.[112,178] Up to now, DPs have been mainly used as UV and X-ray detectors harnessing a long charge carrier diffusion length and a large band gap.[179–181] Consequently, the dynamics of long-living charge carriers received most of the attention so far, while there is a lack of understanding of the early timescale.[182] However, the knowledge about the initial charge carrier dynamics after photoexcitation is of utmost importance for complete utilization and subsequent development of optoelectronic applications based on DPs. Accordingly, the initial relaxation dynamics of charge carriers will be investigated in this chapter.

The presented results are mainly based on Reference 183. It will be shown that directly after photoexcitation hole trapping leads to the formation of defect-related bound excitons at the direct band gap transition. Furthermore, the transfer of direct to indirect bound excitons will be investigated. Finally, the general prospects in terms of applications that utilize this material will be discussed.

5.1 Unexpected High Exciton Binding Energy due to Large Effective Masses

The synthesis of cubic $Cs_2AgBiBr_6$ DP NCs with an average edge length of (8.9 ± 0.2) nm has already been presented in Subsection 3.1.2. It should be noted that the size of these NCs is larger than the estimated exciton Bohr radius of 3 nm (see Table 2.3). Accordingly, strong quantum confinement effects as they have been observed in the previous chapter are not expected this time. For all following experiments, these NCs have been dispersed in toluene. The linear absorption spectrum of such a dispersion is shown in Figure 5.1 by the gray area. A strong peak at 430 nm (2.88 eV) dominates the absorption onset. Toward shorter wavelengths, the absorption strength continuously increases. Interestingly, this strong absorption peak was not observed in all previous reports on $Cs_2AgBiBr_6$ DPs.[29] If it was observed, it was simply attributed to excitons without further explanation.[173] It should be noted that this would correspond to a surprisingly large exciton binding energy of several hundreds of meV compared to the few meV observed for conventional bulk-like perovskites. Actually, there is a discussion in the literature about the reason for this strong absorption peak, which was observed for several kinds of DPs. In the case of $Cs_2AgInCl_6$ showing a direct band gap, for example, this feature is assigned to self-trapped excitons that originate from a distortion of the $AgCl_6$ octahedron in the excited state.[184] A similar explanation involving polarons is proposed for defect halide perovskites (*e. g.*, $Cs_3Bi_2I_9$). Nevertheless, the origin of the strong absorption peak in case of the herein investigated $Cs_2AgBiBr_6$ DP NCs is not clear. In the following, it will be shown that the electronic band structure plays a crucial role in order

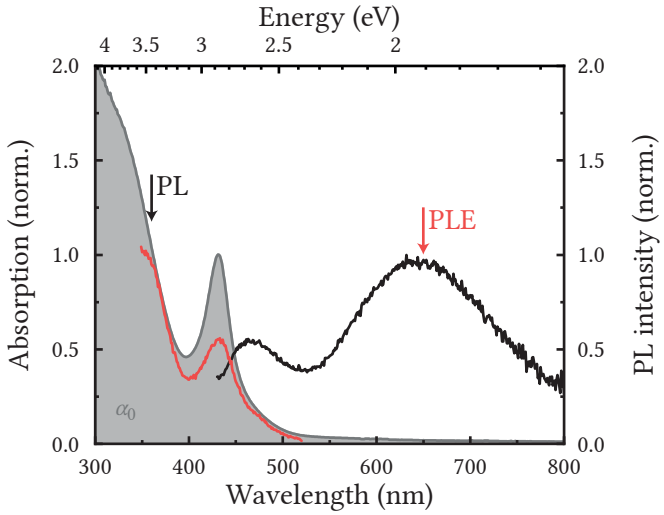

Figure 5.1: Linear Spectroscopy of $Cs_2AgBiBr_6$ DP NCs. The normalized absorption spectrum of NCs dispersed in toluene is depicted as the gray area. The PL spectrum is shown by the black line ($\lambda_{ex} = 365$ nm) and the PLE spectrum detected at $\lambda_{em} = 650$ nm is given by the red line.

to understand the optical properties of $Cs_2AgBiBr_6$ DP. Furthermore, it will be possible to explain the strong absorption peak by defect-related direct bound excitons.

The electronic band structure of $Cs_2AgBiBr_6$ DP obtained by a DFT calculation is depicted in Figure 5.2.[29] Obviously, the effective mass of charge carriers is highly anisotropic, especially at the X point, which corresponds to the direct band gap (see Figure 2.1.2 for details). While the CB around the X point is relatively flat (especially toward the W point) leading to a very large effective mass of electrons, the VB shows a strong dispersion at the X point. This results in a low effective mass of holes ($0.14\,m_e$ in the $X \rightarrow \Gamma$ direction).[29] Thus, according to Equation 2.13, the reduced mass of an electron-hole pair is low as well despite the large electron effective mass. However, a small reduced mass should result in a low exciton binding energy based on Equation 2.15, which is in strong contrast to the observation of a pronounced exciton-like feature in the absorption spectrum.

Halide DPs possess intrinsic defects, and the most important and easily formed stable shallow defects are Ag^+ vacancies. These shallow defects act as hole acceptors leading to the localization of holes. A localized state, however, corresponds to a flat level in the electronic band structure. This is depicted as the brown horizontal line in Figure 5.2. Hence, the trapped holes will possess an infinite effective mass. Now, as both charge carriers have a large effective mass, the reduced mass of an electron-hole pair is huge as well. Thus, an electron can form an exciton with a hole that is bound to a trap state. Due to the huge reduced mass, such a bound exciton has a large binding energy. Furthermore, while the exciton is bound to the trap state, it still extends over many unit cells of the crystal. Thus, the exciton shows a *giant*

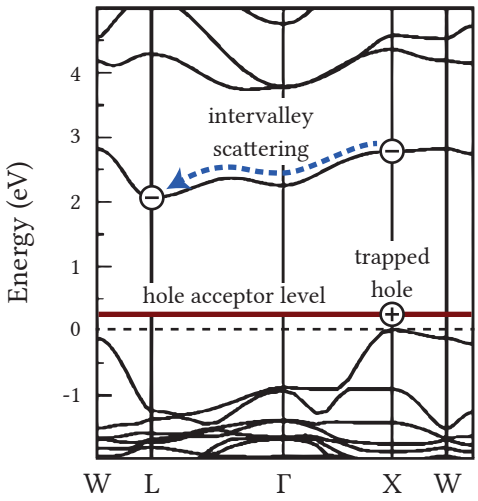

Figure 5.2: Band Structure of $Cs_2AgBiBr_6$ DP: Intervalley Scattering and Trapped Holes. The indirect band structure leads to intervalley scattering of electrons from the X to the L point (blue arrow). Holes may localize due to trap states (*e. g.*, Ag^+ vacancies), which causes an infinite effective hole mass. This hole acceptor level is depicted as the brown horizontal line. The band structure shown here and in the following figures is adapted with permission from Reference 29. Copyright 2016 American Chemical Society.

oscillator strength, which can explain the strong absorption peak at 430 nm. Very recently, theoretical calculations showed that the first absorption peak in $Cs_2AgBiBr_6$ and $Cs_2In_2X_6$ is consistent with bound excitons using ground- and excited-state *ab initio* methods.[185]

The bound excitons discussed above rely on the presence of Ag^+ vacancies, which serve as shallow hole acceptor states and may introduce some disorder in the crystal. Therefore, it should be noted that a disordered arrangement of the Ag^+ and Bi^{3+} ions may tune the band gap from indirect to pseudodirect at the Γ point.[186] Nevertheless, in order to achieve such strong disorder, synthesis temperatures beyond 3000 K are required, which is far more than the 140 °C (413 K) used in the present synthesis. Furthermore, it has been shown that Ag^+ vacancies form spontaneously during synthesis, in contrast to deep acceptor defects like Bi^{3+} vacancies or Ag_{Bi} antisites.[187] Thus, the existence of bound excitons seems reasonable, whereas a general change of the electronic band structure due to a disordered crystal lattice is unlikely.

The $Cs_2AgBiBr_6$ DP NCs show only a very weak emission given by the black line in Figure 5.1. In fact, the PL QY is below the resolution limit of the experimental setup ($\ll 5\,\%$). The PL spectrum shows two peaks. The main one is very broad and centered at 650 nm (1.91 eV). Notably, this signal is redshifted by 1 eV compared to the excitonic absorption peak. Furthermore, a high energetic but less intense signal can be observed at 460 nm (2.7 eV) close to the excitonic absorption peak. Such a high energetic emission has already been reported for $Cs_2AgBiBr_6$ single crystals[179] and Na-doped $Cs_2AgInCl_6$ DPs.[184] However, the origin of the emission has not been discussed yet. Actually, if charge carriers are excited at the X point, intervalley scattering should lead to a quick electron relaxation toward the L point. This is indicated by the blue arrow in Figure 5.2. Hence, a noticeable emission from the direct transition at the X point seems unlikely. Nevertheless, the high exciton binding energy leads to a short radiative lifetime of direct bound excitons. Thus, the lifetime is comparable to the time scale of intervalley scattering, which will be discussed in the following section. Therefore, the high energetic emission from defect-related direct bound excitons is still observable.

As mentioned above, the electrons will scatter toward the CBM at the L point. Since the holes remain trapped, the bound excitons at the X point will transform into indirect ones. Furthermore, the dispersion of the CB at the L point is larger compared to the X point, which leads to a decreasing effective mass of electrons. Accordingly, the reduced mass of the electron-hole pair decreases as well. Thus, the indirect bound excitons show a smaller binding energy and may even dissociate at room temperature. Therefore, the main emission signal at 650 nm is attributed to the recombination of indirect bound excitons and free electrons with trapped holes.

The PLE spectrum obtained at an emission wavelength of 650 nm corresponding to the recombination of indirect bound excitons is shown in Figure 5.1 by the red line. It follows the absorption spectrum qualitatively, but the excitonic peak is less prominent compared to

the continuum absorption. Hence, a lower relaxation efficiency of direct to indirect bound excitons is expected compared to the one of free electron-hole pairs. This agrees with the interpretation that some direct bound excitons recombine before intervalley scattering takes place. It should be noted that the PLE spectrum of $Cs_2AgBiBr_6$ single crystals strongly deviates from the spectrum observed here. An additional peak appears in the PLE spectrum at roughly 500 nm (2.5 eV) and is attributed to color centers.[188]

5.2 Transfer of Direct to Indirect Defect-Related Bound Excitons

The observed signals from steady-state linear spectroscopy have been consistently explained by defect-related excitons. In this section, the process of intervalley scattering that leads to the formation of indirect bound excitons will be investigated using time-resolved PL spectroscopy.

Figure 5.3a shows the time-resolved emission from $Cs_2AgBiBr_6$ DP NCs as a color map. The crystals have been excited using a laser wavelength of 375 nm (3.31 eV), which corresponds to continuum transitions. Directly after photoexcitation, a spectrally broad signal starting from 400 nm (3.1 eV) with a maximum at ~430 nm (2.88 eV) can be observed. As described in

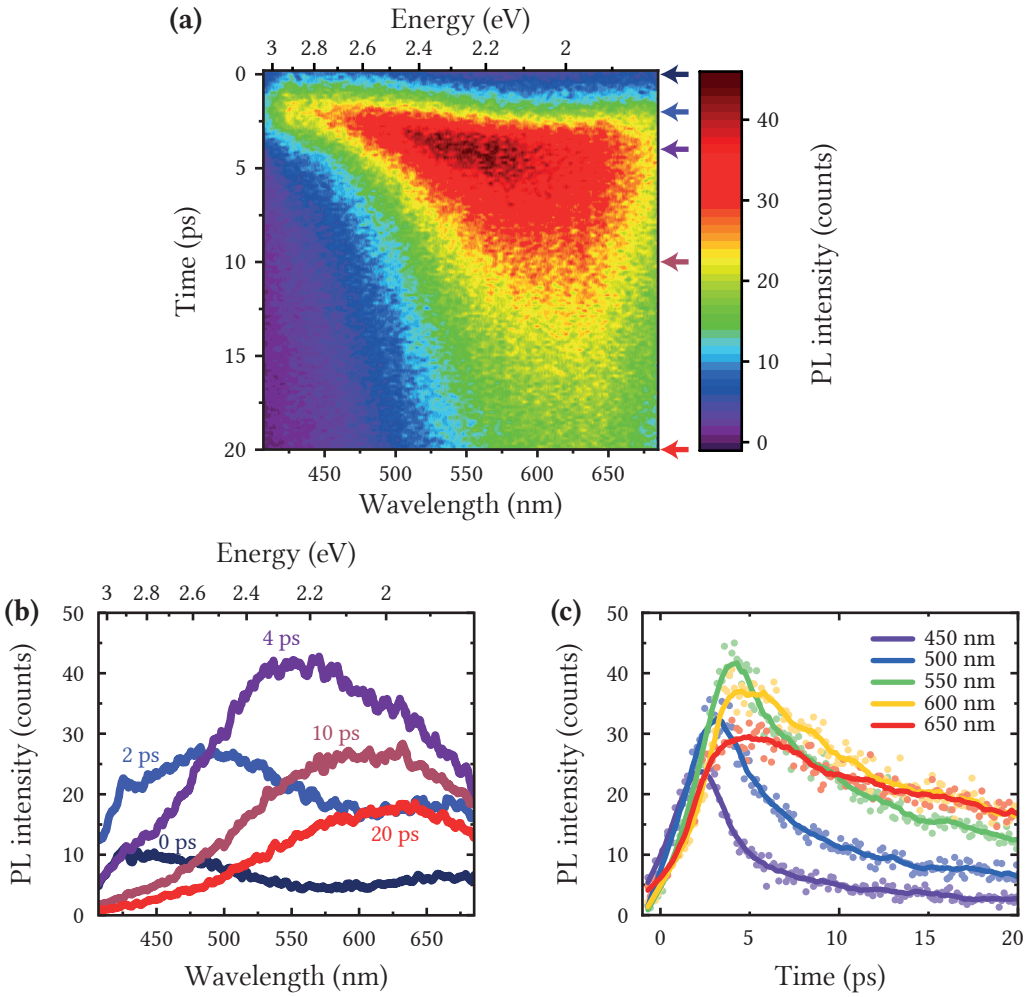

Figure 5.3: Time-Resolved Emission of $Cs_2AgBiBr_6$ DP NCs. **(a)** The PL signal from $Cs_2AgBiBr_6$ DP NCs after photoexcitation at 375 nm (56 mW) is depicted as a color map. The NCs have been dispersed in toluene in a 2 mm cuvette showing a transmission of 10 % at the excitation wavelength. **(b)** PL spectra at various times after photoexcitation (indicated by the arrows in panel a). **(c)** The PL signal as a function of time at specific emission wavelengths. The dots represent the raw data, whereas the lines are a result of a data smoothing process.

the previous section, this high energetic emission can be related to the recombination of direct bound excitons. Within 10 ps, the PL signal gradually redshifts to longer wavelengths (see also Figure 5.3b). During this time, electrons scatter from the X point *via* the Γ valley down to the CBM at the L point leading to the emission at 650 nm (1.91 eV), which corresponds to the steady-state PL maximum.

The efficiency of intervalley scattering strongly depends on the electron-phonon coupling strength. As it has already been discussed in Subsection 2.1.3, the Fröhlich interaction is more significant in perovskites than in classical semiconductors. Furthermore, recent results show that electron-phonon coupling is even more enhanced in DPs compared to lead-based perovskites.[189] This is consistent with the observation of quick intervalley scattering.

Figure 5.3c shows the PL intensity as a function of time at certain emission wavelengths. The emission maximum is reached later in the red spectral region and the decay is significantly slower compared to shorter wavelengths. The PL at 460 nm (2.7 eV) associate with direct bound excitons reduces strongly within 3 ps. This short lifetime confirms the previous interpretation that the high exciton binding energy leads to quick radiative recombination.

The bound excitons at the X point are sketched in Figure 5.4. During the intervalley scattering process taking place on a time scale of 10 ps, the bound excitons become indirect and their binding energy reduces (indicated by the larger exciton Bohr radius). This is in agreement with the observed longer PL lifetime at longer wavelengths as this emission stems from the indirect transition. It should be noted that the PL lifetime mostly reflects nonradiative processes due to the very low PL QY. Accordingly, the radiative lifetime of indirect bound excitons is even much longer. For example, in the case of $Cs_2AgBiBr_6$ single crystals, a PL lifetime of ~660 ns has been observed.[43]

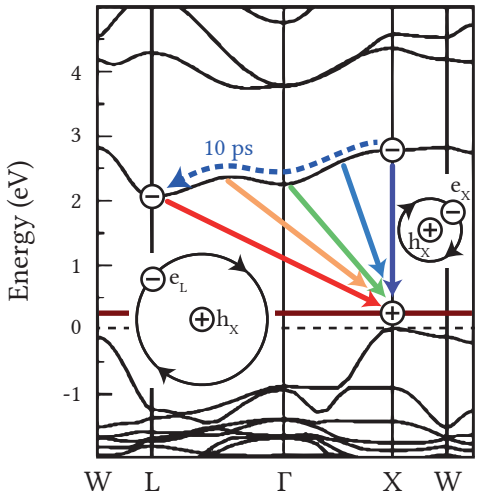

Figure 5.4: Transfer of Direct to Indirect Bound Excitons. While electrons scatter toward the L point, excitons become indirect and the emission wavelength redshifts. Furthermore, the changing effective mass of electrons leads to a reduced exciton binding energy. Thus, the exciton Bohr radius increases.

5.3 The Hole Trapping Process

To obtain a consistent picture of the initial charge carrier dynamics, the hole trapping process that leads to the formation of defect-related direct bound excitons is investigated in this section using DT spectroscopy. To this end, free charge carriers were generated by exciting the NCs at 330 nm (3.76 eV), which corresponds to a transition involving higher energetic branches of the electronic band structure. The change in transmission of the sample in the first 3 ps after photoexcitation is shown in Figure 5.5 as a color map. A broad negative signal indicated by the purple arrow appears directly after photoexcitation (blue area). This means that the transmission has decreased compared to the steady-state. A possible explanation may be excited state absorption. This corresponds to a scenario where a charge carrier, which has already been excited by the pump pulse, absorbs a second photon (of the probe pulse) thus occupying an even higher energetic state. The closely-spaced higher energetic branches of the band structure (especially for the hole) suggest that such intraband transitions are possible. Furthermore, two positive DT signals can be observed. The first one is located at 430 nm (2.88 eV), which matches the position of the absorption peak related to direct bound excitons at the X point (blue arrow). The second one appears at shorter wavelengths ($\leq$ 350 nm), where transitions involving higher energetic bands are dominating (black arrow). Both positive signals are attributed to phase space filling.

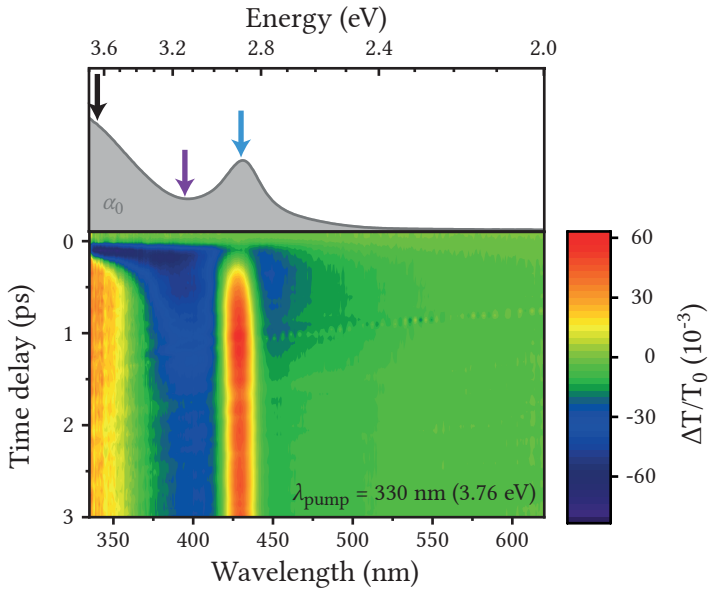

Figure 5.5: DT Signal after Excitation within the Continuum. A color map showing the temporal evolution of the DT signal from $Cs_2AgBiBr_6$ DP NCs dispersed in toluene after photoexcitation at 330 nm (excitation photon density ~$1.2 \cdot 10^{15}$ cm^2). The concentration of NCs equals an OD of 0.4 at the excitonic peak in a 2 mm cuvette. The gray spectrum displayed in the top panel corresponds to the linear absorption for reference.

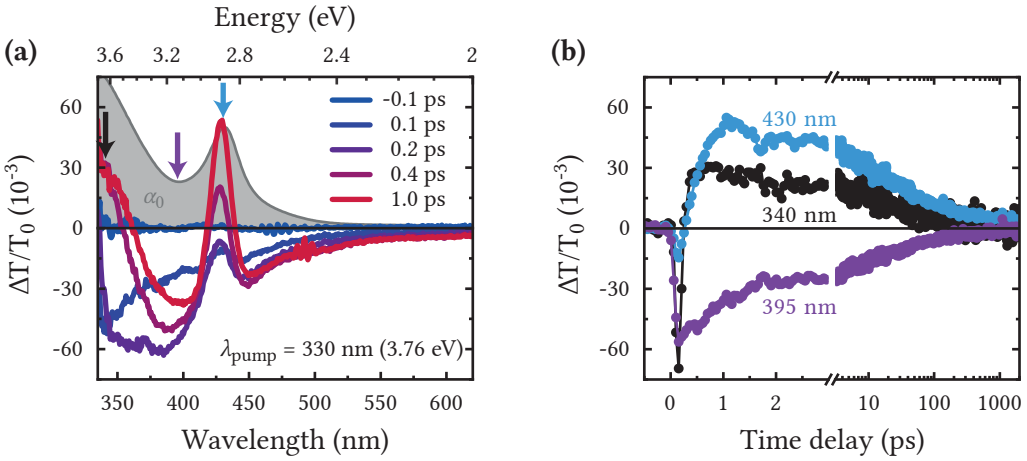

Figure 5.6: Spectral and Temporal Evolution of the DT Signal. (a) DT spectra at various time delays after photoexcitation, taken from Figure 5.5. The linear absorption spectrum is shown for reference by the gray area. **(b)** The DT signal as a function of time at specific probe wavelengths that are indicated by the arrows in (a). Note the logarithmic time axis after 3 ps.

Figure 5.6a shows the temporal evolution of the DT spectra again. Panel (b), on the other hand, displays the time-resolved signals at the probe wavelengths that correspond to the above mentioned three features. The probe wavelengths are indicated by the arrows in panel (a). Interestingly, only the signal associated with direct bound excitons (430 nm, blue) shows a significant rise time. It reaches the maximum 1 ps after the pump pulse has arrived. Subsequently, all signals decay on a similar timescale of several tens of picoseconds to zero. The fact that all three signals decay on a comparable time scale suggests that they are caused by the same charge carriers, which is consistent with the previous interpretation regarding phase space filling and excited state absorption.

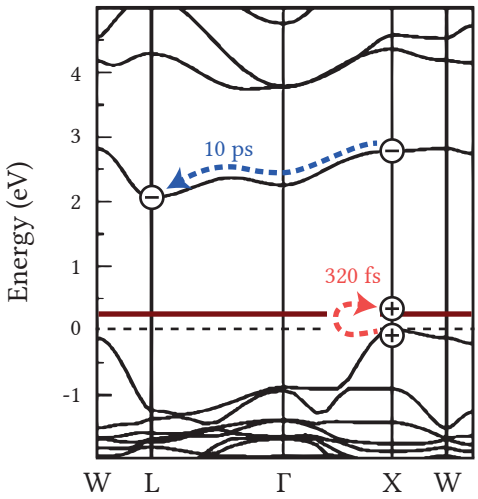

Figure 5.7: The Hole Trapping Process. As indicated by the red arrow, holes become trapped within 320 fs. The blue arrow again represents intervalley scattering talking place on a time scale of 10 ps.

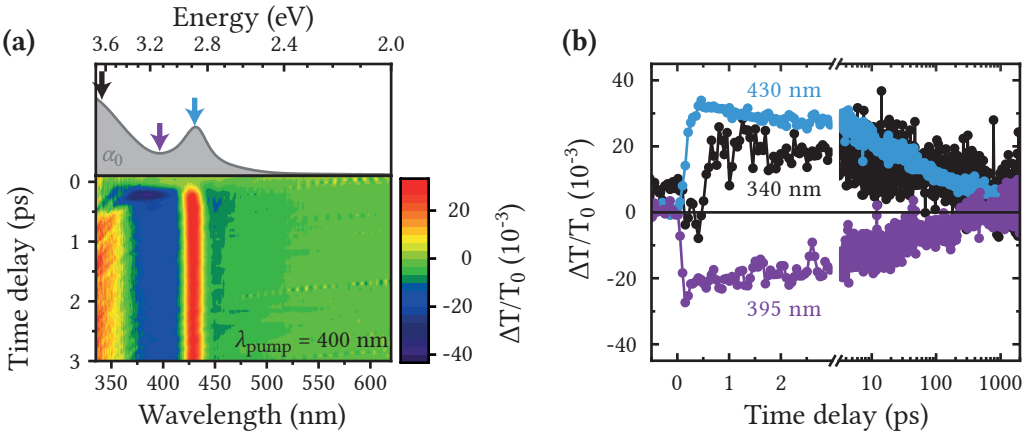

Figure 5.8: DT Signal after Excitation of the Excitonic Transition. (a) A color map showing the temporal evolution of the DT signal from $Cs_2AgBiBr_6$ DP NCs dispersed in toluene after photoexcitation at 400 nm (excitation photon density ~$1.4 \cdot 10^{15}$ cm^2). The gray spectrum displayed in the top panel corresponds to the linear absorption for reference. **(b)** The DT signal as a function of time at specific probe wavelengths that are indicated by the arrows in (a). Note the logarithmic time axis after 3 ps.

The finite rise time of the signal at 430 nm (2.88 eV) can be determined as 320 fs using an exponential model. Accordingly, this time scale can be related to the formation of defect-related direct bound excitons. As the hole trapping process induces the formation of these excitons, the 320 fs can be ascribed to the hole trapping time. This is indicated by the red arrow in Figure 5.7.

This interpretation is consistent with the (nearly) resonant excitation of direct bound excitons discussed in the following. If the sample is pumped at 400 nm (3.1 eV), a similar DT signal as before can be observed (see Figure 5.8a). However, as can be seen in panel (b), a closer look at the three probe wavelengths reveals that the signal at 430 nm (blue) rises this time instantaneously. This confirms the previous interpretation as the direct bound excitons causing this phase space filling are resonantly excited and do not have to form first. Interestingly, the induced absorption in the spectral range between both positive signals can be observed in both excitation scenarios. However, the transitions relevant for the excited state absorption and the relative contributions from electrons and holes are not fully understood yet.

It has already previously been mentioned that the DT signal can be interpreted as the sum of the Fermi distributions at the states relevant for a specific transition (phase space filling). On the other hand, the PL signal is proportional to the product of them. Hence, a comparison of both signals is presented in the following. Figure 5.9 shows the PL signal of direct bound excitons after photoexcitation of continuum transitions as the red line. The corresponding DT signal is given by the black line. The PL signal quickly decays to zero, which has already been explained by the short radiative lifetime of direct bound excitons and the intervalley scattering process. The DT signal, on the other hand, shows two time scales.

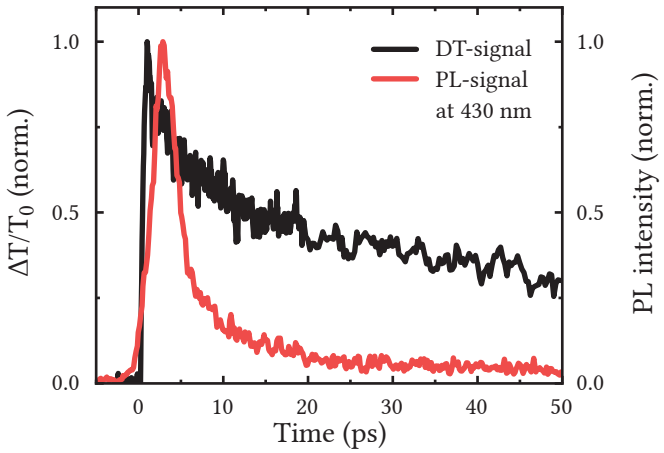

Figure 5.9: Comparison of PL and DT Signals. The black line corresponds to the time-resolved PL signal at 430 nm after photoexcitation at 375 nm (the data are taken from Figure 5.3a). The red line shows the DT signal at 430 nm after photoexcitation at 330 nm (taken from Figure 5.6b). The fast decay component stems from electron intervalley scattering and the recombination of direct bound excitons. The long-living component in case of the DT signal is due to partial phase space filling by the holes.

There is a short component (≤10 ps), which may be explained by the intervalley scattering process of electrons as well since they can no longer contribute to the phase space filling at the direct excitonic transition. Furthermore, there is a long-living signal. This can be related to partial phase space filling of the direct excitonic transition by the trapped holes.

If the excitation density increases, a second electron-hole pair may be excited on an individual NC. This increases the phase space filling and can thus be observed by DT spectroscopy. Figure 5.10 shows the time-resolved DT signal at a probe wavelength of 430 nm, which corresponds to the direct bound excitonic transition, for an increasing excitation photon

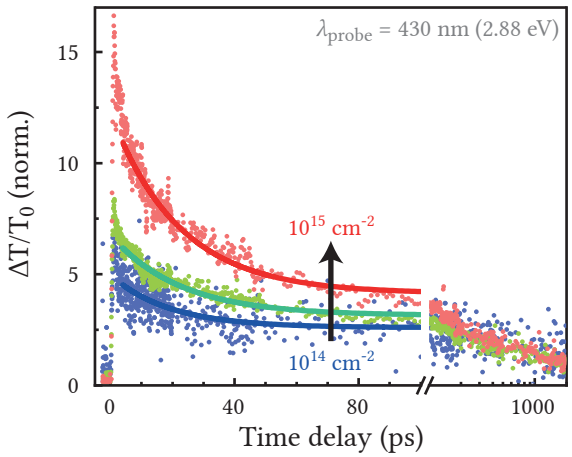

Figure 5.10: Exciton Annihilation. Pump intensity dependence of the DT signal at the direct excitonic transition (430 nm) after photoexcitation at 330 nm. The data are normalized to the long decay component, which is independent of the pump intensity. Dots correspond to the raw data, whereas lines represent a monoexponential fit. Note the logarithmic time axis after 100 ps.

density. Independent of the excitation power, there is a decay component on the order of 10 ps. This can be related to the intervalley scattering process of electrons, which reduces the phase space filling at the direct excitonic transition as discussed above. Furthermore, a new decay component appears with increasing excitation power. Using an exponential function, a power-independent decay constant of 20 ps can be determined. The increased signal at early times can be explained by the excitation of a second electron-hole pair on an individual NCs. Accordingly, the reduction of this signal is related to the recombination of this second electron-hole pair. Possibly, this recombination is due to exciton-exciton annihilation. In this process, one exciton recombines and transfers its energy to the second one, which thus occupies a higher energetic state and subsequently quickly relaxes by phonon scattering.

5.4 What is this Semiconductor Good for?

It has been shown that the initial charge carrier dynamics within $Cs_2AgBiBr_6$ DP NCs can be consistently explained by the interplay of defect-related bound excitons and intervalley scattering. The presence of Ag^+ vacancies leads to hole trapping within a few hundred femtoseconds, which increases the effective mass of holes. Accordingly, the trapped holes can form bound excitons together with heavy electrons at the direct band gap. Thus, these excitons possess a huge binding energy of several hundred meV and a giant oscillator strength, which explains the dominant peak in the steady-state absorption spectrum. Furthermore, the direct bound excitons are responsible for a high energetic emission. Given the fact that intervalley scattering of electrons takes place on the order of 10 ps, the high energetic emission stems from the first few picoseconds after photoexcitation and can be explained by the large oscillator strength of the bound excitons. As the direct bound excitons become indirect, the emission redshifts by 1 eV. At the same time, the effective mass of the electrons decreases due to an increasing dispersion of the CB toward the CBM. Hence, the exciton binding energy reduces and, in combination with the indirect character of the transition, the radiative lifetime increases strongly. Finally, it has been observed that the lifetime of a second electron-hole pair on an individual NC is only 20 ps, which might be related to an exciton-exciton annihilation process.

So far, nontoxic $Cs_2AgBiBr_6$ DP has been mainly applied in the fabrication of solar cells,[190–192] X-ray and UV detectors,[180,181,193–195] and photocatalysts.[196–198] Such applications benefit from long charge carrier diffusion times within $Cs_2AgBiBr_6$ DP[43,179] and its excellent structural stability.[199] However, the strong electron-phonon coupling may prevent a desired large charge carrier mobility.[189,200] Furthermore, the large band gap energy is not ideal for photovoltaic applications.[201]

Despite these few drawbacks, solar cells with a power conversion efficiency of 2.84 % have been realized using $Cs_2AgBiBr_6$ DP.[202] Though this efficiency is an order of magnitude

worse compared to solar cells based on lead halide perovskites,[19] it shows that DPs are a promising new candidate for nontoxic perovskite-based solar cells. The main challenge for a further improvement of their efficiency is to deal with intrinsic and extrinsic defects, which impede a quick charge carrier extraction. Especially, the fabrication process of devices needs to be optimized to obtain high-quality DP films. Furthermore, a suitable energetic alignment between the individual layers of a device is critical. In the case of photodetectors, $Cs_2AgBiBr_6$ DP shows already similar device characteristics as lead-based perovskites. Moreover, such devices exhibit excellent stability at ambient conditions and elevated temperatures.[193]

While the low PL QY of $Cs_2AgBiBr_6$ DP NCs is discouraging for light-emitting applications, it has been shown that surface treatment can enhance the radiative efficiency by passivating defect states.[203] Nevertheless, the major drawback for light emitting-applications is the large indirect band gap. This can be overcome by using DPs of different composition (*e. g.*, by replacing Bi^{3+} ions with In^{3+} or Sb^{3+} and Ag^{+} with Cu^{+}).[204,205] For example, $Cs_2AgInCl_6$ DP with some Bi^{3+} impurities has a direct band gap and allows for the generation of warm white light with a high emission yield of up to 86 %.[184]

$Cs_2AgBiBr_6$ DP is utilized in further interesting research fields including environmentally robust memristors for information storage,[206] real-time humidity sensing,[207] and photoelectrochemical cells that store solar energy.[208] All these diverse applications, in which DPs are already used, show the future potential of this versatile material. In light of the results presented in this chapter, the applications mentioned above may be further improved by considering the strong influence of trap states on the initial charge carrier dynamics.

6

Conclusions and Outlook

The goal of this thesis was to investigate the charge carrier dynamics in nontoxic semiconductor QDs, which are needed for optoelectronic applications. On the one hand, InP/ZnS and InP/ZnSe colloidal core/shell QDs emitting in the red spectral region were characterized. Such QDs have already shown promising characteristics as a substitution of cadmium-based QDs that are used in state-of-the-art LEDs. On the other hand, $Cs_2AgBiBr_6$ DP NCs were studied as they are a potential alternative to the established lead-based halide perovskites, which are used for solar cells and light-emitting applications. To design efficient devices, it is of utmost importance to have a fundamental understanding of the physical processes taking place in these materials. Especially the initial ultrafast dynamics of charge carriers after photoexcitation plays thereby a crucial role.

In the case of InP-based QDs, it was possible to determine the exact charge carrier relaxation times as a function of the initial excess energy with respect to the states leading to emission. As expected, the relaxation takes longer if the excess energy increases. Notably, the relaxation takes up to an order of magnitude longer, reaching several picoseconds, if the charge carriers are excited to states within the shell material. Based on Fermi's Golden Rule, this is due to a small wave function overlap between core and shell states. Furthermore, it turned out that the electron relaxes faster than the hole despite large energetic gaps between the discrete electron states, which should result in a phonon bottleneck. Similar to their cadmium-based counterparts, this was explained by an efficient Auger-like scattering process where the electron transfers its excess energy to the hole, which thus occupies even higher energetic states. Subsequently, the hole relaxes by phonon scattering. As this process takes time, a competing trapping process becomes significant and leads to nonradiative recombina-

tion. Thus, some QDs turn dark and the PL QY decreases with increasing excess energy. With regard to devices, these results demonstrate that it is crucial to consider the injection of charge carriers into the QDs. Specifically, the energetic alignment between charge transport/injection layers and the QDs should be optimized such that the charge carriers enter the QDs close to the states leading to emission. Thus, a trapping-prone slow relaxation can be avoided leading to a large radiative efficiency.

In the case of LEDs, a narrow emission linewidth is needed to reach a large color gamut. While the PL linewidth determined for an ensemble of InP-based QDs is larger compared to cadmium-based QDs, measurements on the single-particle level showed that this can be related to inhomogeneous broadening. This is caused by the size distribution of the QDs, which results in a varying strength of quantum confinement. Hence, a further improvement of the chemical synthesis leading to a sharper size distribution may be needed. Nevertheless, nontoxic InP-based QDs show a similar characteristics compared to cadmium-based QDs, which is encouraging for future applications based on these QDs.

In contrast to conventional lead-based halide perovskites, $Cs_2AgBiBr_6$ DP NCs show an indirect band gap, which results in a substantially different charge carrier dynamics. Besides the indirect band gap, the energetic band structure leads to strongly varying and anisotropic effective masses of charge carriers. Furthermore, defects play a crucial role as they cause the formation of direct bound excitons showing a huge binding energy. Namely, silver vacancies cause hole trapping within a few hundred femtoseconds. The trapped holes, having an infinite effective mass, can thus form excitons with the heavy electrons at the direct band gap transition. As such bound excitons show a giant oscillator strength, a high-energetic emission close to the direct band gap transition can be observed despite the fact that intervalley scattering of electrons takes place on a time scale of 10 ps. As the bound excitons become indirect, the emission redshifts by 1 eV leading to the main PL signal at 650 nm. At the same time, the effective mass of electrons reduces due to an increasing dispersion of the band structure toward the CBM. This results in a reduced exciton binding energy and the radiative lifetime of the charge carriers increases.

This consistent picture of the initial charge carrier dynamics within $Cs_2AgBiBr_6$ DP NCs may facilitate the improvement of applications based on DPs. Especially the role of defects is a key point in order to understand the physical processes taking place. While the low radiative efficiency is a challenge for light-emitting applications, this material may be used in solar cells and photodetectors.

References

[1] Richard P. Feynman. "There's Plenty of Room at the Bottom." In: *Engineering and Science* 23.5 (1960), pp. 22–36 (cited on page 1).

[2] Andrey L. Rogach, ed. *Semiconductor Nanocrystal Quantum Dots: Synthesis, Assembly, Spectroscopy and Applications*. Wien: Springer, 2008. DOI: 10.1007/978-3-211-75237-1 (cited on page 1).

[3] European Parliament and Council. "On the Restriction of the Use of Certain Hazardous Substances in Electrical and Electronic Equipment." In: *Official Journal of the European Union* 54.L174 (2011), pp. 88–110 (cited on page 1).

[4] Brad A. Kairdolf, Andrew M. Smith, Todd H. Stokes, May D. Wang, Andrew N. Young, and Shuming Nie. "Semiconductor Quantum Dots for Bioimaging and Biodiagnostic Applications." In: *Annual Review of Analytical Chemistry* 6 (2013), pp. 143–162. DOI: 10.1146/annurev-anchem-060908-155136 (cited on page 1).

[5] Edward H. Sargent. "Infrared Photovoltaics Made by Solution Processing." In: *Nature Photonics* 3.6 (2009), pp. 325–331. DOI: 10.1038/nphoton.2009.89 (cited on page 1).

[6] Kyung-Sang Cho, Eun Kyung Lee, Won-Jae Joo, Eunjoo Jang, Tae-Ho Kim, Sang Jin Lee, Soon-Jae Kwon, Jai Yong Han, Byung-Ki Kim, Byoung Lyong Choi, and Jong Min Kim. "High-Performance Crosslinked Colloidal Quantum-Dot Light-Emitting Diodes." In: *Nature Photonics* 3.6 (2009), pp. 341–345. DOI: 10.1038/nphoton.2009.92 (cited on page 2).

[7] Ken Werner. "Five Short Display Stories from CES 2018." In: *Information Display* 34.2 (2018), pp. 28–34. DOI: 10.1002/j.2637-496X.2018.tb01071.x (cited on page 2).

[8] Vanessa Wood and Vladimir Bulović. "Colloidal Quantum Dot Light-Emitting Devices." In: *Nano Reviews* 1.1 (2010), p. 5202. DOI: 10.3402/nano.v1i0.5202 (cited on page 2).

[9] Yiran Jiang, Seong-Yong Cho, and Moonsub Shim. "Light-Emitting Diodes of Colloidal Quantum Dots and Nanorod Heterostructures for Future Emissive Displays." In: *Journal of Materials Chemistry C* 6.11 (2018), pp. 2618–2634. DOI: 10.1039/c7tc05972h (cited on page 2).

[10] Beverly A. Rzigalinski and Jeannine S. Strobl. "Cadmium-Containing Nanoparticles: Perspectives on Pharmacology and Toxicology of Quantum Dots." In: *Toxicology and Applied Pharmacology* 238.3 (2009), pp. 280–288. DOI: 10.1016/j.taap.2009.04.010 (cited on page 2).

[11] Hung Chia Wang, Heng Zhang, Hao Yue Chen, Han Cheng Yeh, Mei Rurng Tseng, Ren Jei Chung, Shuming Chen, and Ru Shi Liu. "Cadmium-Free InP/ZnSeS/ZnS Heterostructure-Based Quantum Dot Light-Emitting Diodes with a ZnMgO Electron Transport Layer and a Brightness of Over 10 000 cd m^{-2}." In: *Small* 13.13 (2017), p. 1603962. DOI: 10.1002/smll.201603962 (cited on pages 2, 67).

[12] Jaehoon Lim, Myeongjin Park, Wan Ki Bae, Donggu Lee, Seonghoon Lee, Changhee Lee, and Kookheon Char. "Highly Efficient Cadmium-Free Quantum Dot Light-Emitting Diodes Enabled by the Direct Formation of Excitons within InP@ZnSeS Quantum Dots." In: *ACS Nano* 7.10 (2013), pp. 9019–9026. DOI: 10.1021/nn403594j (cited on pages 2, 67).

[13] Yu Tong, Eva Bladt, Meltem F. Ayguler, Aurora Manzi, Karolina Z. Milowska, Verena A. Hintermayr, Pablo Docampo, Sara Bals, Alexander S. Urban, Lakshminarayana Polavarapu, and Jochen Feldmann. "Highly Luminescent Cesium Lead Halide Perovskite Nanocrystals with Tunable Composition and Thickness by Ultrasonication." In: *Angewandte Chemie, International Edition* 55.44 (2016), pp. 13887–13892. DOI: 10.1002/anie.201605909 (cited on page 2).

[14] Amrita Dey, Pravin Rathod, and Dinesh Kabra. "Role of Localized States in Photoluminescence Dynamics of High Optical Gain $CsPbBr_3$ Nanocrystals." In: *Advanced Optical Materials* 6.11 (2018), p. 1800109. DOI: 10.1002/adom.201800109 (cited on page 2).

[15] Samuel D. Stranks and Henry J. Snaith. "Metal-Halide Perovskites for Photovoltaic and Light-Emitting Devices." In: *Nature Nanotechnology* 10.5 (2015), pp. 391–402. DOI: 10.1038/nnano.2015.90 (cited on page 2).

[16] Loredana Protesescu, Sergii Yakunin, Maryna I. Bodnarchuk, Franziska Krieg, Riccarda Caputo, Christopher H. Hendon, Ruo Xi Yang, Aron Walsh, and Maksym V. Kovalenko. "Nanocrystals of Cesium Lead Halide Perovskites ($CsPbX_3$, X = Cl, Br, and I): Novel Optoelectronic Materials Showing Bright Emission with Wide Color Gamut." In: *Nano Letters* 15.6 (2015), pp. 3692–3696. DOI: 10.1021/nl5048779 (cited on pages 2, 20).

[17] Javad Shamsi, Alexander S. Urban, Muhammad Imran, Luca de Trizio, and Liberato Manna. "Metal Halide Perovskite Nanocrystals: Synthesis, Post-Synthesis Modifications, and Their Optical Properties." In: *Chemical Reviews* 119.5 (2019), pp. 3296–3348. DOI: 10.1021/acs.chemrev.8b00644 (cited on page 2).

[18] David A. Egger, Achintya Bera, David Cahen, Gary Hodes, Thomas Kirchartz, Leeor Kronik, Robert Lovrincic, Andrew M. Rappe, David R. Reichman, and Omer Yaffe. "What Remains Unexplained about the Properties of Halide Perovskites?" In: *Advanced Materials* 30.20 (2018), p. 1800691. DOI: 10.1002/adma.201800691 (cited on page 2).

[19] National Renewable Energy Laboratory. *Best Research-Cell Efficiencies*. URL: https://www.nrel.gov/pv/assets/pdfs/best-research-cell-efficiencies.20200925.pdf (visited on 09/29/2020) (cited on pages 2, 101).

[20] Yichuan Ling, Zhao Yuan, Yu Tian, Xi Wang, Jamie C. Wang, Yan Xin, Kenneth Hanson, Biwu Ma, and Hanwei Gao. "Bright Light-Emitting Diodes Based on Organometal Halide Perovskite Nanoplatelets." In: *Advanced Materials* 28.2 (2016), pp. 305–311. DOI: 10.1002/adma.201503954 (cited on page 2).

[21] Naresh K. Kumawat, Amrita Dey, Aravindh Kumar, Sreelekha P. Gopinathan, K. L. Narasimhan, and Dinesh Kabra. "Band Gap Tuning of $CH_3NH_3Pb(Br_{(1-x)}Cl_x)_3$ Hybrid Perovskite for Blue Electroluminescence." In: *ACS Applied Materials & Interfaces* 7.24 (2015), pp. 13119–13124. DOI: 10.1021/acsami.5b02159 (cited on page 2).

[22] Feng Zhang, Haizheng Zhong, Cheng Chen, Xian-gang Wu, Xiangmin Hu, Hailong Huang, Junbo Han, Bingsuo Zou, and Yuping Dong. "Brightly Luminescent and Color-Tunable Colloidal $CH_3NH_3PbX_3$ (X = Br, I, Cl) Quantum Dots: Potential Alternatives for Display Technology." In: *ACS Nano* 9.4 (2015), pp. 4533–4542. DOI: 10.1021/acsnano.5b01154 (cited on page 2).

[23] Verena A. Hintermayr, Alexander F. Richter, Florian Ehrat, Markus Doblinger, Willem Vanderlinden, Jasmina A. Sichert, Yu Tong, Lakshminarayana Polavarapu, Jochen Feldmann, and Alexander S. Urban. "Tuning the Optical Properties of Perovskite Nanoplatelets through Composition and Thickness by Ligand-Assisted Exfoliation." In: *Advanced Materials* 28.43 (2016), pp. 9478–9485. DOI: 10.1002/adma.201602897 (cited on pages 2, 7, 23).

[24] Bernhard J. Bohn, Yu Tong, Moritz Gramlich, May Ling Lai, Markus Döblinger, Kun Wang, Robert L. Z. Hoye, Peter Müller-Buschbaum, Samuel D. Stranks, Alexander S. Urban, Lakshminarayana Polavarapu, and Jochen Feldmann. "Boosting Tunable Blue Luminescence of Halide Perovskite Nanoplatelets through Postsynthetic Surface Trap Repair." In: *Nano Letters* 18.8 (2018), pp. 5231–5238. DOI: 10.1021/acs.nanolett.8b02190 (cited on page 2).

[25] Yue-Yu Zhang, Shiyou Chen, Peng Xu, Hongjun Xiang, Xin-Gao Gong, Aron Walsh, and Su-Huai Wei. "Intrinsic Instability of the Hybrid Halide Perovskite Semiconductor $CH_3NH_3PbI_3$." In: *Chinese Physics Letters* 35.3 (2018), p. 36104. DOI: 10.1088/0256-307X/35/3/036104 (cited on page 2).

[26] Nicholas Aristidou, Irene Sanchez-Molina, Thana Chotchuangchutchaval, Michael Brown, Luis Martinez, Thomas Rath, and Saif A. Haque. "The Role of Oxygen in the Degradation of Methylammonium Lead Trihalide Perovskite Photoactive Layers." In: *Angewandte Chemie, International Edition* 54.28 (2015), pp. 8208–8212. DOI: 10.1002/anie.201503153 (cited on page 2).

[27] G. P. Nagabhushana, Radha Shivaramaiah, and Alexandra Navrotsky. "Direct Calorimetric Verification of Thermodynamic Instability of Lead Halide Hybrid Perovskites." In: *Proceedings of the National Academy of Sciences of the United States of America* 113.28 (2016), pp. 7717–7721. DOI: 10.1073/pnas.1607850113 (cited on page 2).

[28] Aslihan Babayigit, Anitha Ethirajan, Marc Muller, and Bert Conings. "Toxicity of Organometal Halide Perovskite Solar Cells." In: *Nature Materials* 15.3 (2016), pp. 247–251. DOI: 10.1038/nmat4572 (cited on page 2).

[29] Eric T. McClure, Molly R. Ball, Wolfgang Windl, and Patrick M. Woodward. "Cs_2AgBiX_6 (X = Br, Cl): New Visible Light Absorbing, Lead-Free Halide Perovskite Semiconductors." In: *Chemistry of Materials* 28.5 (2016), pp. 1348–1354. DOI: 10.1021/acs.chemmater.5b04231 (cited on pages 2, 10, 11, 17, 18, 89–91).

[30] Gustav Rose. "Beschreibung einiger neuen Mineralien des Urals." In: *Annalen der Physik und Chemie* 124.12 (1839), pp. 551–573. DOI: 10.1002/andp.18391241205 (cited on page 5).

[31] H. L. Wells. "Über die Cäsium- und Kalium-Bleihalogenide." In: *Zeitschrift für anorganische Chemie* 3.1 (1893), pp. 195–210. DOI: 10.1002/zaac.18930030124 (cited on page 5).

[32] A. von Hippel. "Ferroelectricity, Domain Structure, and Phase Transitions of Barium Titanate." In: *Reviews of Modern Physics* 22.3 (1950), pp. 221–237. DOI: 10.1103/RevModPhys.22.221 (cited on page 5).

[33] Chr. Kn. Møller. "Crystal Structure and Photoconductivity of Cæsium Plumbohalides." In: *Nature* 182.4647 (1958), p. 1436. DOI: 10.1038/1821436a0 (cited on page 5).

[34] D. Balz and K. Plieth. "Die Struktur des Kaliumnickelfluorids, K_2NiF_4." In: *Zeitschrift für Elektrochemie* 59.6 (1955), pp. 545–551. DOI: 10.1002/bbpc.19550590613 (cited on page 5).

[35] Henry J. Snaith. "Perovskites: The Emergence of a New Era for Low-Cost, High-Efficiency Solar Cells." In: *The Journal of Physical Chemistry Letters* 4.21 (2013), pp. 3623–3630. DOI: 10.1021/jz4020162 (cited on page 6).

[36] Roger H. Mitchell, Mark D. Welch, and Anton R. Chakhmouradian. "Nomenclature of the Perovskite Supergroup: A Hierarchical System of Classification Based on Crystal Structure and Composition." In: *Mineralogical Magazine* 81.3 (2017), pp. 411–461. DOI: 10.1180/minmag.2016.080.156 (cited on page 6).

[37] Quinten A. Akkerman and Liberato Manna. "What Defines a Halide Perovskite?" In: *ACS Energy Letters* 5.2 (2020), pp. 604–610. DOI: 10.1021/acsenergylett.0c00039 (cited on page 6).

[38] Gregor Kieslich, Shijing Sun, and Anthony K. Cheetham. "An Extended Tolerance Factor Approach for Organic-Inorganic Perovskites." In: *Chemical Science* 6.6 (2015), pp. 3430–3433. DOI: 10.1039/C5SC00961H (cited on page 6).

[39] Victor M. Goldschmidt. "Die Gesetze der Krystallochemie." In: *Die Naturwissenschaften* 14.21 (1926), pp. 477–485. DOI: 10.1007/BF01507527 (cited on page 6).

[40] Shunsuke Hirotsu, Jimpei Harada, Masashi Iizumi, and Kazuo Gesi. "Structural Phase Transitions in $CsPbBr_3$." In: *Journal of the Physical Society of Japan* 37.5 (1974), pp. 1393–1398. DOI: 10.1143/JPSJ.37.1393 (cited on pages 7, 17).

[41] Yixin Zhao and Kai Zhu. "Organic-Inorganic Hybrid Lead Halide Perovskites for Optoelectronic and Electronic Applications." In: *Chemical Society Reviews* 45.3 (2016), pp. 655–689. DOI: 10.1039/c4cs00458b (cited on page 7).

[42] Xiaoming Li, Fei Cao, Dejian Yu, Jun Chen, Zhiguo Sun, Yalong Shen, Ying Zhu, Lin Wang, Yi Wei, Ye Wu, and Haibo Zeng. "All Inorganic Halide Perovskites Nanosystem: Synthesis, Structural Features, Optical Properties and Optoelectronic Applications." In: *Small* 13.9 (2017), p. 1603996. DOI: 10.1002/smll.201603996 (cited on page 7).

[43] Adam H. Slavney, Te Hu, Aaron M. Lindenberg, and Hemamala I. Karunadasa. "A Bismuth-Halide Double Perovskite with Long Carrier Recombination Lifetime for Photovoltaic Applications." In: *Journal of the American Chemical Society* 138.7 (2016), pp. 2138–2141. DOI: 10.1021/jacs.5b13294 (cited on pages 7, 95, 100).

[44] Claus F. Klingshirn. *Semiconductor Optics*. Berlin and Heidelberg: Springer, 2012. DOI: 10.1007/978-3-642-28362-8 (cited on pages 8, 10, 19–21, 42).

[45] Gerd Czycholl. *Theoretische Festkörperphysik*. Berlin and Heidelberg: Springer, 2008. DOI: 10.1007/978-3-540-74790-1 (cited on page 9).

[46] Peter Y. Yu and Manuel Cardona. *Fundamentals of Semiconductors*. Berlin and Heidelberg: Springer, 2010. DOI: 10.1007/978-3-642-00710-1 (cited on pages 9, 12, 18, 29, 41, 42).

[47] P. Rochon and E. Fortin. "Photovoltaic Effect and Interband Magneto-Optical Transitions in InP." In: *Physical Review B* 12.12 (1975), pp. 5803–5810. DOI: 10.1103/PhysRevB.12.5803 (cited on pages 10, 11, 25, 68, 70).

[48] Seppo Lindroos, Tapio Kanniainen, and Markku Leskelä. "Growth of Zinc Sulfide Thin Films by the Successive Ionic Layer Adsorption and Reaction (Silar) Method on Polyester Substrates." In: *Materials Research Bulletin* 32.12 (1997), pp. 1631–1636. DOI: 10.1016/S0025-5408(97)00155-4 (cited on pages 10, 68).

[49] H. Morkoç, S. Strite, G. B. Gao, M. E. Lin, B. Sverdlov, and M. Burns. "Large-Band-Gap SiC, III-V Nitride, and II-VI ZnSe-Based Semiconductor Device Technologies." In: *Journal of Applied Physics* 76.3 (1994), pp. 1363–1398. DOI: 10.1063/1.358463 (cited on pages 10, 11, 68).

[50] Laura M. Herz. "Charge-Carrier Dynamics in Organic-Inorganic Metal Halide Perovskites." In: *Annual Review of Physical Chemistry* 67 (2016), pp. 65–89. DOI: 10.1146/annurev-physchem-040215-112222 (cited on pages 10, 14, 16, 20).

[51] Constantinos C. Stoumpos, Christos D. Malliakas, John A. Peters, Zhifu Liu, Maria Sebastian, Jino Im, Thomas C. Chasapis, Arief C. Wibowo, Duck Young Chung, Arthur J. Freeman, Bruce W. Wessels, and Mercouri G. Kanatzidis. "Crystal Growth of the Perovskite Semiconductor $CsPbBr_3$: A New Material for High-Energy Radiation Detection." In: *Crystal Growth & Design* 13.7 (2013), pp. 2722–2727. DOI: 10.1021/cg400645t (cited on page 10).

[52] J. Schanda, G. Gergely, and M. Gál. "Zur Bestimmung der effektiven Masse von Ladungsträgern in ZnS." In: *Zeitschrift für Naturforschung A* 24.9 (1969), pp. 1353–1356. DOI: 10.1515/zna-1969-0913 (cited on page 11).

[53] Marina R. Filip, Carla Verdi, and Feliciano Giustino. "GW Band Structures and Carrier Effective Masses of $CH_3NH_3PbI_3$ and Hypothetical Perovskites of the Type $APbI_3$: A = NH_4, PH_4, AsH_4, and SbH_4." In: *The Journal of Physical Chemistry C* 119.45 (2015), pp. 25209–25219. DOI: 10.1021/acs.jpcc.5b07891 (cited on page 11).

[54] Yatendra P. Varshni. "Temperature Dependence of the Energy Gap in Semiconductors." In: *Physica* 34.1 (1967), pp. 149–154. DOI: 10.1016/0031-8914(67)90062-6 (cited on page 12).

[55] Louis Biadala, Benjamin Siebers, Raquel Gomes, Zeger Hens, Dmitri R. Yakovlev, and Manfred Bayer. "Tuning Energy Splitting and Recombination Dynamics of Dark and Bright Excitons in CdSe/CdS Dot-in-Rod Colloidal Nanostructures." In: *The Journal of Physical Chemistry C* 118.38 (2014), pp. 22309–22316. DOI: 10.1021/jp505887u (cited on page 15).

[56] Louis Biadala, Benjamin Siebers, Yasin Beyazit, Mickaël D. Tessier, Dorian Dupont, Zeger Hens, Dmitri R. Yakovlev, and Manfred Bayer. "Band-Edge Exciton Fine Structure and Recombination Dynamics in InP/ZnS Colloidal Nanocrystals." In: *ACS Nano* 10.3 (2016), pp. 3356–3364. DOI: 10.1021/acsnano.5b07065 (cited on page 15).

[57] Chenghua Hu, Feng Wang, and Zhou Zheng. "Pressure-Induced Metallic Phase Transition and Elastic Properties of Indium Phosphide III-V Semiconductor." In: *Journal of Materials Research* 27.8 (2012), pp. 1105–1111. DOI: 10.1557/jmr.2012.60 (cited on page 15).

[58] Jun Kang and Lin-Wang Wang. "High Defect Tolerance in Lead Halide Perovskite $CsPbBr_3$." In: *The Journal of Physical Chemistry Letters* 8.2 (2017), pp. 489–493. DOI: 10.1021/acs.jpclett.6b02800 (cited on pages 15–17).

[59] Jacky Even, Laurent Pedesseau, Jean-Marc Jancu, and Claudine Katan. "Importance of Spin–Orbit Coupling in Hybrid Organic/Inorganic Perovskites for Photovoltaic Applications." In: *The Journal of Physical Chemistry Letters* 4.17 (2013), pp. 2999–3005. DOI: 10.1021/jz401532q (cited on page 16).

[60] G. Bihlmayer, O. Rader, and R. Winkler. "Focus on the Rashba Effect." In: *New Journal of Physics* 17.5 (2015), p. 50202. DOI: 10.1088/1367-2630/17/5/050202 (cited on page 16).

[61] Dane W. deQuilettes, Kyle Frohna, David Emin, Thomas Kirchartz, Vladimir Bulovic, David S. Ginger, and Samuel D. Stranks. "Charge-Carrier Recombination in Halide Perovskites." In: *Chemical Reviews* 119.20 (2019), pp. 11007–11019. DOI: 10.1021/acs.chemrev.9b00169 (cited on page 16).

[62] Wan-Jian Yin, Tingting Shi, and Yanfa Yan. "Unusual Defect Physics in $CH_3NH_3PbI_3$ Perovskite Solar Cell Absorber." In: *Applied Physics Letters* 104.6 (2014), p. 63903. DOI: 10.1063/1.4864778 (cited on page 16).

[63] Joseph S. Manser, Jeffrey A. Christians, and Prashant V. Kamat. "Intriguing Optoelectronic Properties of Metal Halide Perovskites." In: *Chemical Reviews* 116.21 (2016), pp. 12956–13008. DOI: 10.1021/acs.chemrev.6b00136 (cited on page 16).

[64] P. Hohenberg and W. Kohn. "Inhomogeneous Electron Gas." In: *Physical Review* 136.3B (1964), pp. B864–B871. DOI: 10.1103/PhysRev.136.B864 (cited on page 17).

[65] W. Kohn and L. J. Sham. "Self-Consistent Equations Including Exchange and Correlation Effects." In: *Physical Review* 140.4A (1965), pp. A1133–A1138. DOI: 10.1103/PhysRev.140.A1133 (cited on page 17).

[66] Sebastian Rieger, Bernhard J. Bohn, Markus Döblinger, Alexander F. Richter, Yu Tong, Kun Wang, Peter Müller-Buschbaum, Lakshminarayana Polavarapu, Linn Leppert, Jacek K. Stolarczyk, and Jochen Feldmann. "Excitons and Narrow Bands Determine the Optical Properties of Cesium Bismuth Halides." In: *Physical Review B* 100.20 (2019), p. 201404. DOI: 10.1103/PhysRevB.100.201404 (cited on page 17).

[67] R. J. Elliott. "Intensity of Optical Absorption by Excitons." In: *Physical Review* 108.6 (1957), pp. 1384–1389. DOI: 10.1103/PhysRev.108.1384 (cited on page 18).

[68] Neil W. Ashcroft and N. David Mermin. *Solid State Physics*. New York and London: Harcourt College Publishers, 1976 (cited on page 18).

[69] Jacov Frenkel. "On the Transformation of Light into Heat in Solids. II." In: *Physical Review* 37.10 (1931), pp. 1276–1294. DOI: 10.1103/PhysRev.37.1276 (cited on page 20).

[70] Marina R. Filip, Samuel Hillman, Amir Abbas Haghighirad, Henry J. Snaith, and Feliciano Giustino. "Band Gaps of the Lead-Free Halide Double Perovskites $Cs_2BiAgCl_6$ and $Cs_2BiAgBr_6$ from Theory and Experiment." In: *The Journal of Physical Chemistry Letters* 7.13 (2016), pp. 2579–2585. DOI: 10.1021/acs.jpclett.6b01041 (cited on page 20).

[71] Huaxiang Fu, Lin-Wang Wang, and Alex Zunger. "Excitonic Exchange Splitting in Bulk Semiconductors." In: *Physical Review B* 59.8 (1999), pp. 5568–5574. DOI: 10.1103/PhysRevB.59.5568 (cited on pages 20, 68).

[72] B. Bhattacharjee, D. Ganguli, K. IakoubovskII, A. Stesmans, and S. Chaudhuri. "Synthesis and Characterization of Sol-Gel Derived ZnS: Mn^{2+} Nanocrystallites Embedded in a Silica Matrix." In: *Bulletin of Materials Science* 25.3 (2002), pp. 175–180. DOI: 10.1007/BF02711150 (cited on page 20).

[73] Pelekanos, Ding, Hagerott, Nurmikko, Luo, Samarth, and Furdyna. "Quasi-Two-Dimensional Excitons in (Zn,Cd)Se/ZnSe Quantum Wells: Reduced Exciton-LO-Phonon Coupling due to Confinement Effects." In: *Physical Review B* 45.11 (1992), pp. 6037–6042. DOI: 10.1103/PhysRevB.45.6037 (cited on page 20).

[74] Kenichiro Tanaka, Takayuki Takahashi, Takuma Ban, Takashi Kondo, Kazuhito Uchida, and Noboru Miura. "Comparative Study on the Excitons in Lead-Halide-Based Perovskite-Type Crystals $CH_3NH_3PbBr_3$ $CH_3NH_3PbI_3$." In: *Solid State Communications* 127.9-10 (2003), pp. 619–623. DOI: 10.1016/S0038-1098(03)00566-0 (cited on page 20).

[75] Emmanuel I. Rashba. "Progress in Exciton Spectroscopy: Personal Perspective." In: *Journal of Luminescence* 87-89 (2000), pp. 1–6. DOI: 10.1016/S0022-2313(99)00204-5 (cited on page 20).

[76] Emmanuel I. Rashba and Givi E. Gurgenishvili. "On the Theory of Edge Absorption in Semiconductors." In: *Soviet Physics - Solid State* 4.4 (1962), pp. 759–760 (cited on page 20).

[77] Federico Brivio, Keith T. Butler, Aron Walsh, and Mark van Schilfgaarde. "Relativistic Quasiparticle Self-Consistent Electronic Structure of Hybrid Halide Perovskite Photovoltaic Absorbers." In: *Physical Review B* 89.15 (2014), p. 155204. DOI: 10.1103/PhysRevB.89.155204 (cited on page 20).

[78] E. Menéndez-Proupin, Carlos L. Beltrán Ríos, and P. Wahnón. "Nonhydrogenic Exciton Spectrum in Perovskite $CH_3NH_3PbI_3$." In: *Physica Status Solidi RRL: Rapid Research Letters* 9.10 (2015), pp. 559–563. DOI: 10.1002/pssr.201510265 (cited on pages 20, 21).

[79] Sadao Adachi. "GaAs, AlAs, and $Al_xGa_{1-x}As$: Material Parameters for Use in Research and Device Applications." In: *Journal of Applied Physics* 58.3 (1985), pp. R1–R29. DOI: 10.1063/1.336070 (cited on page 21).

[80] M. Helm, W. Knap, W. Seidenbusch, R. Lassnig, E. Gornik, R. Triboulet, and L. L. Taylor. "Polaron Cyclotron Resonance in n-CdTe and n-InP." In: *Solid State Communications* 53.6 (1985), pp. 547–550. DOI: 10.1016/0038-1098(85)90189-9 (cited on page 21).

[81] Michael Sendner, Pabitra K. Nayak, David A. Egger, Sebastian Beck, Christian Müller, Bernd Epding, Wolfgang Kowalsky, Leeor Kronik, Henry J. Snaith, Annemarie Pucci, and Robert Lovrinčić. "Optical Phonons in Methylammonium Lead Halide Perovskites and Implications for Charge Transport." In: *Materials Horizons* 3.6 (2016), pp. 613–620. DOI: 10.1039/C6MH00275G (cited on page 21).

[82] J. Pollmann and H. Büttner. "Effective Hamiltonians and Bindings Energies of Wannier Excitons in Polar Semiconductors." In: *Physical Review B* 16.10 (1977), pp. 4480–4490. DOI: 10.1103/PhysRevB.16.4480 (cited on page 21).

[83] Michal Baranowski and Paulina Plochocka. "Excitons in Metal-Halide Perovskites." In: *Advanced Energy Materials* 10.26 (2020), p. 1903659. DOI: 10.1002/aenm.201903659 (cited on page 21).

[84] Feliciano Giustino and Henry J. Snaith. "Toward Lead-Free Perovskite Solar Cells." In: *ACS Energy Letters* 1.6 (2016), pp. 1233–1240. DOI: 10.1021/acsenergylett.6b00499 (cited on page 21).

[85] Yehonadav Bekenstein, Jakob C. Dahl, Jianmei Huang, Wojciech T. Osowiecki, Joseph K. Swabeck, Emory M. Chan, Peidong Yang, and A. Paul Alivisatos. "The Making and Breaking of Lead-Free Double Perovskite Nanocrystals of Cesium Silver-Bismuth Halide Compositions." In: *Nano Letters* 18.6 (2018), pp. 3502–3508. DOI: 10.1021/acs.nanolett.8b00560 (cited on page 21).

[86] Shunran Li, Jiajun Luo, Jing Liu, and Jiang Tang. "Self-Trapped Excitons in All-Inorganic Halide Perovskites: Fundamentals, Status, and Potential Applications." In: *The Journal of Physical Chemistry Letters* 10.8 (2019), pp. 1999–2007. DOI: 10.1021/acs.jpclett.8b03604 (cited on page 21).

[87] K. Sugii, H. Koizumi, and E. Kubota. "Precision Lattice Parameter Measurements on Doped Indium Phosphide Single Crystals." In: *Journal of Electronic Materials* 12.4 (1983), pp. 701–712. DOI: 10.1007/BF02676797 (cited on pages 22, 36).

[88] David J. Norris. "Electronic Structure in Semiconductor Nanocrystals: Optical Experiment." In: *Nanocrystal Quantum Dots*. Ed. by Victor I. Klimov. Boca Raton: Taylor & Francis, 2010, pp. 63–96. DOI: 10.1201/9781420079272 (cited on page 22).

[89] M. Grundmann, R. Heitz, D. Bimberg, J.H.H. Sandmann, and J. Feldmann. "Carrier Dynamics in Quantum Dots: Modeling with Master Equations for the Transitions between Micro-States." In: *Physica Status Solidi B: Basic Solid State Physics* 203.1 (1997), pp. 121–132. DOI: 10.1002/1521-3951(199709)203:1<121::AID-PSSB121>3.0.CO;2-M (cited on page 23).

[90] M. Grundmann and D. Bimberg. "Theory of Random Population for Quantum Dots." In: *Physical Review B* 55.15 (1997), pp. 9740–9745. DOI: 10.1103/PhysRevB.55.9740 (cited on page 23).

[91] Jörg Sandmann. "Ladungsträgerdynamik in verspannungsinduzierten Halbleiter-Quantenpunkten." PhD Thesis. Munich, 1998 (cited on page 23).

[92] Ulrike Woggon. *Optical Properties of Semiconductor Quantum Dots*. Berlin and Heidelberg: Springer, 1997. DOI: 10.1007/BFb0119351 (cited on pages 23, 26, 29, 72).

[93] Jasmina A. Sichert, Yu Tong, Niklas Mutz, Mathias Vollmer, Stefan Fischer, Karolina Z. Milowska, Ramon Garcia Cortadella, Bert Nickel, Carlos Cardenas-Daw, Jacek K. Stolarczyk, Alexander S. Urban, and Jochen Feldmann. "Quantum Size Effect in Organometal Halide Perovskite Nanoplatelets." In: *Nano Letters* 15.10 (2015), pp. 6521–6527. DOI: 10.1021/acs.nanolett.5b02985 (cited on page 23).

[94] Siegfried Flügge. *Practical Quantum Mechanics*. Berlin and Heidelberg: Springer, 1971. DOI: 10.1007/978-3-642-61995-3 (cited on page 24).

[95] Sergey I. Pokutnyi, Oleg V. Ovchinnikov, and Tamara S. Kondratenko. "Absorption of Light by Colloidal Semiconductor Quantum Dots." In: *Journal of Nanophotonics* 10.3 (2016), p. 33506. DOI: 10.1117/1.JNP.10.033506 (cited on pages 26, 71).

[96] Marius Grundmann. *The Physics of Semiconductors*. Cham: Springer, 2016. DOI: 10.1007/978-3-319-23880-7 (cited on page 27).

[97] Su-Huai Wei and Alex Zunger. "Calculated Natural Band Offsets of All II–VI and III–V Semiconductors: Chemical Trends and the Role of Cation d Orbitals." In: *Applied Physics Letters* 72.16 (1998), pp. 2011–2013. DOI: 10.1063/1.121249 (cited on pages 27, 69).

[98] Wolfgang Demtröder. *Laserspektroskopie 1*. Berlin and Heidelberg: Springer, 2011. DOI: 10.1007/978-3-642-21306-9 (cited on page 28).

[99] S. Rudin, T. L. Reinecke, and B. Segall. "Temperature-Dependent Exciton Linewidths in Semiconductors." In: *Physical Review B* 42.17 (1990), pp. 11218–11231. DOI: 10.1103/PhysRevB.42.11218 (cited on page 28).

[100] Bernhard J. Bohn, Thomas Simon, Moritz Gramlich, Alexander F. Richter, Lakshminarayana Polavarapu, Alexander S. Urban, and Jochen Feldmann. "Dephasing and Quantum Beating of Excitons in Methylammonium Lead Iodide Perovskite Nanoplatelets." In: *ACS Photonics* 5.2 (2017), pp. 648–654. DOI: 10.1021/acsphotonics.7b01292 (cited on page 28).

[101] Jagdeep Shah. *Ultrafast Spectroscopy of Semiconductors and Semiconductor Nanostructures*. Berlin and Heidelberg: Springer, 1999. DOI: 10.1007/978-3-662-03770-6 (cited on pages 29, 63).

[102] H. Benisty, C. M. Sotomayor-Torrès, and C. Weisbuch. "Intrinsic Mechanism for the Poor Luminescence Properties of Quantum-Box Systems." In: *Physical Review B* 44.19 (1991), pp. 10945–10948. DOI: 10.1103/PhysRevB.44.10945 (cited on page 30).

[103] Al. L. Efros, V. A. Kharchenko, and M. Rosen. "Breaking the Phonon Bottleneck in Nanometer Quantum Dots: Role of Auger-Like Processes." In: *Solid State Communications* 93.4 (1995), pp. 281–284. DOI: 10.1016/0038-1098(94)00760-8 (cited on pages 30, 82).

[104] C. B. Murray, D. J. Norris, and M. G. Bawendi. "Synthesis and Characterization of Nearly Monodisperse CdE (E = Sulfur, Selenium, Tellurium) Semiconductor Nanocrystallites." In: *Journal of the American Chemical Society* 115.19 (1993), pp. 8706–8715. DOI: 10.1021/ja00072a025 (cited on page 34).

[105] Victor K. LaMer and Robert H. Dinegar. "Theory, Production and Mechanism of Formation of Monodispersed Hydrosols." In: *Journal of the American Chemical Society* 72.11 (1950), pp. 4847–4854. DOI: 10.1021/ja01167a001 (cited on page 34).

[106] Peter Reiss, Marie Carrière, Christophe Lincheneau, Louis Vaure, and Sudarsan Tamang. "Synthesis of Semiconductor Nanocrystals, Focusing on Nontoxic and Earth-Abundant Materials." In: *Chemical Reviews* 116.18 (2016), pp. 10731–10819. DOI: 10.1021/acs.chemrev.6b00116 (cited on pages 34, 36).

[107] Xiaogang Peng, J. Wickham, and A. P. Alivisatos. "Kinetics of II-VI and III-V Colloidal Semiconductor Nanocrystal Growth: "Focusing" of Size Distributions." In: *Journal of the American Chemical Society* 120.21 (1998), pp. 5343–5344. DOI: 10.1021/ja9805425 (cited on page 34).

[108] W. Ostwald. "Studien über die Bildung und Umwandlung fester Körper." In: *Zeitschrift für Physikalische Chemie* 22U.1 (1897). DOI: 10.1515/zpch-1897-2233 (cited on page 34).

[109] Celso de Mello Donegá, Peter Liljeroth, and Daniel Vanmaekelbergh. "Physicochemical Evaluation of the Hot-Injection Method, a Synthesis Route for Monodisperse Nanocrystals." In: *Small* 1.12 (2005), pp. 1152–1162. DOI: 10.1002/smll.200500239 (cited on page 34).

[110] Soon Gu Kwon and Taeghwan Hyeon. "Formation Mechanisms of Uniform Nanocrystals *via* Hot-Injection and Heat-Up Methods." In: *Small* 7.19 (2011), pp. 2685–2702. DOI: 10.1002/smll.201002022 (cited on page 34).

[111] Joel van Embden, Anthony S. R. Chesman, and Jacek J. Jasieniak. "The Heat-Up Synthesis of Colloidal Nanocrystals." In: *Chemistry of Materials* 27.7 (2015), pp. 2246–2285. DOI: 10.1021/cm5028964 (cited on page 34).

[112] Sidney E. Creutz, Evan N. Crites, Michael C. de Siena, and Daniel R. Gamelin. "Colloidal Nanocrystals of Lead-Free Double-Perovskite (Elpasolite) Semiconductors: Synthesis and Anion Exchange to Access New Materials." In: *Nano Letters* 18.2 (2018), pp. 1118–1123. DOI: 10.1021/acs.nanolett.7b04659 (cited on pages 34, 89).

[113] A. A. Guzelian, J. E. B. Katari, A. V. Kadavanich, U. Banin, K. Hamad, E. Juban, A. P. Alivisatos, R. H. Wolters, C. C. Arnold, and J. R. Heath. "Synthesis of Size-Selected, Surface-Passivated InP Nanocrystals." In: *The Journal of Physical Chemistry* 100.17 (1996), pp. 7212–7219. DOI: 10.1021/jp953719f (cited on page 36).

[114] Sudarsan Tamang, Christophe Lincheneau, Yannick Hermans, Sohee Jeong, and Peter Reiss. "Chemistry of InP Nanocrystal Syntheses." In: *Chemistry of Materials* 28.8 (2016), pp. 2491–2506. DOI: 10.1021/acs.chemmater.5b05044 (cited on page 36).

[115] Karl David Wegner, Fanny Dussert, Delphine Truffier-Boutry, Anass Benayad, David Beal, Lucia Mattera, Wai Li Ling, Marie Carrière, and Peter Reiss. "Influence of the Core/Shell Structure of Indium Phosphide Based Quantum Dots on their Photostability and Cytotoxicity." In: *Frontiers in Chemistry* 7 (2019), p. 466. DOI: 10.3389/fchem.2019.00466 (cited on page 36).

[116] Eriko Nitta, Mitsuyoshi Kimata, Mihoko Hoshino, Takuya Echigo, Satoshi Hamasaki, Norimasa Nishida, Masahiro Shimizu, and Takeshi Akasaka. "Crystal Chemistry of ZnS Minerals Formed as High-Temperature Volcanic Sublimates: Matraite Identical with Sphalerite." In: *Journal of Mineralogical and Petrological Sciences* 103.2 (2008), pp. 145–151. DOI: 10.2465/jmps.071022f (cited on page 36).

[117] Paul Ramdohr. "Stilleit, ein neues Mineral, natürliches Zinkselenid, von Shinkolobwe." In: *Zeitschrift der Deutschen Geologischen Gesellschaft* 108.3 (1956), pp. 481–483. DOI: 10.1127/zdgg/108/1956/481 (cited on page 36).

[118] Mickael D. Tessier, Dorian Dupont, Kim de Nolf, Jonathan de Roo, and Zeger Hens. "Economic and Size-Tunable Synthesis of InP/ZnE (E = S, Se) Colloidal Quantum Dots." In: *Chemistry of Materials* 27.13 (2015), pp. 4893–4898. DOI: 10.1021/acs.chemmater.5b02138 (cited on page 36).

[119] Yu-Ho Won, Oul Cho, Taehyung Kim, Dae-Young Chung, Taehee Kim, Heejae Chung, Hyosook Jang, Junho Lee, Dongho Kim, and Eunjoo Jang. "Highly Efficient and Stable InP/ZnSe/ZnS Quantum Dot Light-Emitting Diodes." In: *Nature* 575.7784 (2019), pp. 634–638. DOI: 10.1038/s41586-019-1771-5 (cited on page 36).

[120] Christian Ippen, Tonino Greco, Yohan Kim, Christopher Pries, Jiwan Kim, Min Suk Oh, Chul Jong Han, and Armin Wedel. "Color Tuning of Indium Phosphide Quantum Dots for Cadmium-Free Quantum Dot Light-Emitting Devices with High Efficiency and Color Saturation." In: *Journal of the Society for Information Display* 23.7 (2015), pp. 285–293. DOI: 10.1002/jsid.308 (cited on page 36).

[121] B. Heyne, K. Arlt, A. Geßner, A. F. Richter, M. Döblinger, J. Feldmann, A. Taubert, and A. Wedel. "Mixed Mercaptocarboxylic Acid Shells Provide Stable Dispersions of InPZnS/ZnSe/ZnS Multishell Quantum Dots in Aqueous Media." In: *Nanomaterials* 10.9 (2020), p. 1858. DOI: 10.3390/nano10091858 (cited on page 37).

[122] Woo-Seuk Song, Hye-Seung Lee, Ju Chul Lee, Dong Seon Jang, Yoonyoung Choi, Moongoo Choi, and Heesun Yang. "Amine-Derived Synthetic Approach to Color-Tunable InP/ZnS Quantum Dots with High Fluorescent Qualities." In: *Journal of Nanoparticle Research* 15.6 (2013), p. 1750. DOI: 10.1007/s11051-013-1750-y (cited on page 37).

[123] Brandon M. McMurtry, Kevin Qian, Joseph K. Teglasi, Anindya K. Swarnakar, Jonathan de Roo, and Jonathan S. Owen. "Continuous Nucleation and Size Dependent Growth Kinetics of Indium Phosphide Nanocrystals." In: *Chemistry of Materials* 32.10 (2020), pp. 4358–4368. DOI: 10.1021/acs.chemmater.0c01561 (cited on page 37).

[124] Rohit P. Prasankumar and Antoinette J. Taylor, eds. *Optical Techniques for Solid-State Materials Characterization.* Boca Raton: CRC Press, 2016. DOI: 10.1201/b11040 (cited on page 39).

[125] Jonathan Mooney and Patanjali Kambhampati. "Get the Basics Right: Jacobian Conversion of Wavelength and Energy Scales for Quantitative Analysis of Emission Spectra." In: *The Journal of Physical Chemistry Letters* 4.19 (2013), pp. 3316–3318. DOI: 10.1021/jz401508t (cited on page 40).

[126] Sajan Saini. "Methods for Obtaining the Optical Response after CW Excitation." In: *Optical Techniques for Solid-State Materials Characterization.* Ed. by Rohit P. Prasankumar and Antoinette J. Taylor. Boca Raton: CRC Press, 2016, pp. 151–192. DOI: 10.1201/b11040 (cited on page 42).

[127] Jan Valenta. "Determination of Absolute Quantum Yields of Luminescing Nanomaterials over a Broad Spectral Range: From the Integrating Sphere Theory to the Correct Methodology." In: *Nanoscience Methods* 3.1 (2014), pp. 11–27. DOI: 10.1080/21642311.2014.884288 (cited on page 42).

[128] Patricia I. Scheurle, Andre Mähringer, Andreas C. Jakowetz, Pouya Hosseini, Alexander F. Richter, Gunther Wittstock, Dana D. Medina, and Thomas Bein. "A Highly Crystalline Anthracene-Based MOF-74 Series Featuring Electrical Conductivity and Luminescence." In: *Nanoscale* 11.43 (2019), pp. 20949–20955. DOI: 10.1039/C9NR05431F (cited on page 42).

[129] Kartik Srinivasan, Matthew T. Rakher, and Marcelo Davanço. "Micro-Optical Techniques." In: *Optical Techniques for Solid-State Materials Characterization*. Ed. by Rohit P. Prasankumar and Antoinette J. Taylor. Boca Raton: CRC Press, 2016, pp. 575–618. DOI: 10.1201/b11040 (cited on page 44).

[130] Yanxiu Li, He Huang, Yuan Xiong, Alexander F. Richter, Stephen V. Kershaw, Jochen Feldmann, and Andrey L. Rogach. "Using Polar Alcohols for the Direct Synthesis of Cesium Lead Halide Perovskite Nanorods with Anisotropic Emission." In: *ACS Nano* 13.7 (2019), pp. 8237–8245. DOI: 10.1021/acsnano.9b03508 (cited on page 44).

[131] Yuan Xiong, Xiaoyu Zhang, Alexander F. Richter, Yanxiu Li, Aaron Döring, Peter Kasák, Anton Popelka, Julian Schneider, Stephen V. Kershaw, Seung Jo Yoo, Jin-Gyu Kim, Wei Zhang, Weitao Zheng, Elena V. Ushakova, Jochen Feldmann, and Andrey L. Rogach. "Chemically Synthesized Carbon Nanorods with Dual Polarized Emission." In: *ACS Nano* 13.10 (2019), pp. 12024–12031. DOI: 10.1021/acsnano.9b06263 (cited on pages 44, 60).

[132] Bernhard J. Bohn. "Exciton Dynamics in Lead Halide Perovskite Nanocrystals: Recombination, Dephasing and Diffusion." PhD Thesis. Munich: Ludwig-Maximilians-Universität, 2019 (cited on pages 44, 61).

[133] Wilfried Neumann. *Fundamentals of Dispersive Optical Spectroscopy Systems*. Bellingham: Society of Photo-Optical Instrumentation Engineers (SPIE), 2014. DOI: 10.1117/3.1002528 (cited on page 48).

[134] Wolfgang Becker. *Advanced Time Correlated Single Photon Counting Techniques*. Berlin and Heidelberg: Springer, 2005. DOI: 10.1007/3-540-28882-1 (cited on page 49).

[135] Yu Tong, Ming Fu, Eva Bladt, He Huang, Alexander F. Richter, Kun Wang, Peter Müller-Buschbaum, Sara Bals, Philippe Tamarat, Brahim Lounis, Jochen Feldmann, and Lakshminarayana Polavarapu. "Chemical Cutting of Perovskite Nanowires into Single-Photon Emissive Low-Aspect-Ratio $CsPbX_3$ (X=Cl, Br, I) Nanorods." In: *Angewandte Chemie, International Edition* 57.49 (2018), pp. 16094–16098. DOI: 10.1002/anie.201810110 (cited on page 49).

[136] Gautham Nair, Jing Zhao, and Moungi G. Bawendi. "Biexciton Quantum Yield of Single Semiconductor Nanocrystals from Photon Statistics." In: *Nano Letters* 11.3 (2011), pp. 1136–1140. DOI: 10.1021/nl104054t (cited on page 49).

[137] Alexander L. Efros and David J. Nesbitt. "Origin and Control of Blinking in Quantum Dots." In: *Nature Nanotechnology* 11.8 (2016), pp. 661–671. DOI: 10.1038/nnano.2016.140 (cited on page 49).

[138] Marc Achermann. "Time-Resolved Photoluminescence Spectroscopy." In: *Optical Techniques for Solid-State Materials Characterization*. Ed. by Rohit P. Prasankumar and Antoinette J. Taylor. Boca Raton: CRC Press, 2016, pp. 443–465. DOI: 10.1201/b11040 (cited on page 51).

[139] Andreas Velten, Di Wu, Adrian Jarabo, Belen Masia, Christopher Barsi, Chinmaya Joshi, Everett Lawson, Moungi Bawendi, Diego Gutierrez, and Ramesh Raskar. "Femto-Photography: Capturing and Visualizing the Propagation of Light." In: *ACM Transactions on Graphics* 32.4 (2013), p. 44. DOI: 10.1145/2461912.2461928 (cited on page 55).

[140] M. Achermann, J. A. Hollingsworth, and V. I. Klimov. "Multiexcitons Confined within a Subexcitonic Volume: Spectroscopic and Dynamical Signatures of Neutral and Charged Biexcitons in Ultrasmall Semiconductor Nanocrystals." In: *Physical Review B* 68.24 (2003), p. 314. DOI: 10.1103/PhysRevB.68.245302 (cited on page 60).

[141] Stefanie D. Pritzl, Fernando Pschunder, Florian Ehrat, Santanu Bhattacharyya, Theobald Lohmüller, Maria Ana Huergo, and Jochen Feldmann. "Trans-Membrane Fluorescence Enhancement by Carbon Dots: Ionic Interactions and Energy Transfer." In: *Nano Letters* 19.6 (2019), pp. 3886–3891. DOI: 10.1021/acs.nanolett.9b01071 (cited on page 60).

[142] Andrew Kowalevicz. "Ultrashort Pulse Generation and Measurement." In: *Optical Techniques for Solid-State Materials Characterization*. Ed. by Rohit P. Prasankumar and Antoinette J. Taylor. Boca Raton: CRC Press, 2016, pp. 237–289. DOI: 10.1201/b11040 (cited on page 62).

[143] Y. Shen and G. Z. Yang. "Theory of Self-Phase Modulation and Spectral Broadening." In: *The Supercontinuum Laser Source*. Ed. by Robert R. Alfano. New York: Springer, 2006, pp. 1–32. DOI: 10.1007/0-387-25097-2_1 (cited on page 62).

[144] David Giovanni, Wee Kiang Chong, Yu Yang Fredrik Liu, Herlina Arianita Dewi, Tingting Yin, Yulia Lekina, Ze Xiang Shen, Nripan Mathews, Chee Kwan Gan, and Tze Chien Sum. "Coherent Spin and Quasiparticle Dynamics in Solution-Processed Layered 2D Lead Halide Perovskites." In: *Advanced Science* 5.10 (2018), p. 1800664. DOI: 10.1002/advs.201800664 (cited on page 63).

[145] S. Schmitt-Rink, D. S. Chemla, and D. A. B. Miller. "Linear and Nonlinear Optical Properties of Semiconductor Quantum Wells." In: *Advances in Physics* 38.2 (1989), pp. 89–188. DOI: 10.1080/00018738900101102 (cited on page 63).

[146] S. Schmitt-Rink, D. A. B. Miller, and D. S. Chemla. "Theory of the Linear and Nonlinear Optical Properties of Semiconductor Microcrystallites." In: *Physical Review B* 35.15 (1987), pp. 8113–8125. DOI: 10.1103/PhysRevB.35.8113 (cited on page 63).

[147] S. Schmitt-Rink. "Ultrafast Nonlinear Optical Phenomena in Semiconductor Quantum Wells." In: *Interfaces, Quantum Wells, and Superlattices*. Ed. by C. Richard Leavens and Roger Taylor. Vol. 179. NATO ASI Series, Series B. Boston, MA: Springer, 1988, pp. 211–226. DOI: 10.1007/978-1-4613-1045-7_12 (cited on page 63).

[148] Victor I. Klimov. "Spectral and Dynamical Properties of Multiexcitons in Semiconductor Nanocrystals." In: *Annual Review of Physical Chemistry* 58 (2007), pp. 635–673. DOI: 10.1146/annurev.physchem.58.032806.104537 (cited on page 63).

[149] David Giovanni, Wee Kiang Chong, Herlina Arianita Dewi, Krishnamoorthy Thirumal, Ishita Neogi, Ramamoorthy Ramesh, Subodh Mhaisalkar, Nripan Mathews, and Tze Chien Sum. "Tunable Room-Temperature Spin-Selective Optical Stark Effect in Solution-Processed Layered Halide Perovskites." In: *Science Advances* 2.6 (2016), p. 1600477. DOI: 10.1126/sciadv.1600477 (cited on page 63).

[150] Vinay Sharma, Sigalit Aharon, Itay Gdor, Chunfan Yang, Lioz Etgar, and Sanford Ruhman. "New Insights into Exciton Binding and Relaxation from High Time Resolution Ultrafast Spectroscopy of $CH_3NH_3PbI_3$ and $CH_3NH_3PbBr_3$ Films." In: *Journal of Materials Chemistry A* 4.9 (2016), pp. 3546–3553. DOI: 10.1039/C5TA09643J (cited on page 63).

[151] F. Jahnke, M. Kira, S. W. Koch, G. Khitrova, E. K. Lindmark, T. R. Nelson, D. V. Wick, J. D. Berger, O. Lyngnes, H. M. Gibbs, and K. Tai. "Excitonic Nonlinearities of Semiconductor Microcavities in the Nonperturbative Regime." In: *Physical Review Letters* 77.26 (1996), pp. 5257–5260. DOI: 10.1103/PhysRevLett.77.5257 (cited on page 63).

[152] H. Schweizer, A. Forchel, A. Hangleiter, S. Schmitt-Rink, J. P. Löwenau, and H. Haug. "Ionization of the Direct-Gap Exciton in Photoexcited Germanium." In: *Physical Review Letters* 51.8 (1983), pp. 698–701. DOI: 10.1103/PhysRevLett.51.698 (cited on page 63).

[153] W. H. Knox, D. S. Chemla, D. A. B. Miller, J. B. Stark, and S. Schmitt-Rink. "Femtosecond AC Stark Effect in Semiconductor Quantum Wells: Extreme Low- and High-Intensity Limits." In: *Physical Review Letters* 62.10 (1989), pp. 1189–1192. DOI: 10.1103/PhysRevLett.62.1189 (cited on page 63).

[154] Ye Yang, Mengjin Yang, Kai Zhu, Justin C. Johnson, Joseph J. Berry, Jao van de Lagemaat, and Matthew C. Beard. "Large Polarization-Dependent Exciton Optical Stark Effect in Lead Iodide Perovskites." In: *Nature Communications* 7 (2016), p. 12613. DOI: 10.1038/ncomms12613 (cited on page 63).

[155] V. I. Klimov, D. W. McBranch, C. A. Leatherdale, and M. G. Bawendi. "Electron and Hole Relaxation Pathways in Semiconductor Quantum Dots." In: *Physical Review B* 60.19 (1999), pp. 13740–13749. DOI: 10.1103/PhysRevB.60.13740 (cited on pages 67, 76, 80).

[156] V. I. Klimov, A. A. Mikhailovsky, D. W. McBranch, C. A. Leatherdale, and M. G. Bawendi. "Mechanisms for Intraband Energy Relaxation in Semiconductor Quantum Dots: The Role of Electron-Hole Interactions." In: *Physical Review B* 61.20 (2000), pp. R13349–R13352. DOI: 10.1103/PhysRevB.61.R13349 (cited on page 67).

[157] Victor I. Klimov. "Optical Nonlinearities and Ultrafast Carrier Dynamics in Semiconductor Nanocrystals." In: *The Journal of Physical Chemistry B* 104.26 (2000), pp. 6112–6123. DOI: 10.1021/jp9944132 (cited on page 67).

[158] S. Xu, A. A. Mikhailovsky, J. A. Hollingsworth, and V. I. Klimov. "Hole Intraband Relaxation in Strongly Confined Quantum Dots: Revisiting the "Phonon Bottleneck" Problem." In: *Physical Review B* 65.4 (2002), p. 45319. DOI: 10.1103/PhysRevB.65.045319 (cited on page 67).

[159] Victor I. Klimov and Duncan W. McBranch. "Femtosecond 1P-to-1S Electron Relaxation in Strongly Confined Semiconductor Nanocrystals." In: *Physical Review Letters* 80.18 (1998), pp. 4028–4031. DOI: 10.1103/PhysRevLett.80.4028 (cited on page 67).

[160] Jeff L. Blackburn, Randy J. Ellingson, Olga I. Mićić, and Arthur J. Nozik. "Electron Relaxation in Colloidal InP Quantum Dots with Photogenerated Excitons or Chemically Injected Electrons." In: *The Journal of Physical Chemistry B* 107.1 (2003), pp. 102–109. DOI: 10.1021/jp026746w (cited on page 67).

[161] Randy J. Ellingson, Jeff L. Blackburn, Jovan Nedeljkovic, Garry Rumbles, Marcus Jones, Huaxiang Fu, and Arthur J. Nozik. "Theoretical and Experimental Investigation of Electronic Structure and Relaxation of Colloidal Nanocrystalline Indium Phosphide Quantum Dots." In: *Physical Review B* 67.7 (2003), p. 75308. DOI: 10.1103/PhysRevB.67.075308 (cited on pages 67, 80).

[162] Randy J. Ellingson, Jeff L. Blackburn, Pingrong Yu, Garry Rumbles, Olga I. Mićić, and Arthur J. Nozik. "Excitation Energy Dependent Efficiency of Charge Carrier Relaxation and Photoluminescence in Colloidal InP Quantum Dots." In: *The Journal of Physical Chemistry B* 106.32 (2002), pp. 7758–7765. DOI: 10.1021/jp025666p (cited on page 67).

[163] Garry Rumbles, Donald C. Selmarten, Randy J. Ellingson, Jeffrey L. Blackburn, Pingrong Yu, Barton B. Smith, Olga I. Mićić, and Arthur J. Nozik. "Anomalies in the Linear Absorption, Transient Absorption, Photoluminescence and Photoluminescence Excitation Spectroscopies of Colloidal InP Quantum Dots." In: *Journal of Photochemistry and Photobiology A: Chemistry* 142.2-3 (2001), pp. 187–195. DOI: 10.1016/S1010-6030(01)00513-5 (cited on page 67).

[164] Alexander F. Richter, Michael Binder, Bernhard J. Bohn, Nathan Grumbach, Shany Neyshtadt, Alexander S. Urban, and Jochen Feldmann. "Fast Electron and Slow Hole Relaxation in InP-Based Colloidal Quantum Dots." In: *ACS Nano* 13.12 (2019), pp. 14408–14415. DOI: 10.1021/acsnano.9b07969 (cited on page 67).

[165] Jialong Zhao, Julie A. Bardecker, Andrea M. Munro, Michelle S. Liu, Yuhua Niu, I-Kang Ding, Jingdong Luo, Baoquan Chen, Alex K.-Y. Jen, and David S. Ginger. "Efficient CdSe/CdS Quantum Dot Light-Emitting Diodes Using a Thermally Polymerized Hole Transport Layer." In: *Nano Letters* 6.3 (2006), pp. 463–467. DOI: 10.1021/nl052417e (cited on page 68).

[166] Kyungnam Kim, Hangyeoul Lee, Jaewook Ahn, and Sohee Jeong. "Highly Luminescing Multi-Shell Semiconductor Nanocrystals InP/ZnSe/ZnS." In: *Applied Physics Letters* 101.7 (2012), p. 73107. DOI: 10.1063/1.4745844 (cited on pages 69, 70).

[167] Gregory Kalyuzhny and Royce W. Murray. "Ligand Effects on Optical Properties of CdSe Nanocrystals." In: *The Journal of Physical Chemistry B* 109.15 (2005), pp. 7012–7021. DOI: 10.1021/jp045352x (cited on page 73).

[168] U. Woggon, H. Giessen, F. Gindele, O. Wind, B. Fluegel, and N. Peyghambarian. "Ultrafast Energy Relaxation in Quantum Dots." In: *Physical Review B* 54.24 (1996), pp. 17681–17690. DOI: 10.1103/PhysRevB.54.17681 (cited on page 76).

[169] Gianluca Grimaldi, Jaco J. Geuchies, Ward van der Stam, Indy Du Fossé, Baldur Brynjarsson, Nicholas Kirkwood, Sachin Kinge, Laurens D. A. Siebbeles, and Arjan J. Houtepen. "Spectroscopic Evidence for the Contribution of Holes to the Bleach of Cd-Chalcogenide Quantum Dots." In: *Nano Letters* 19.5 (2019), pp. 3002–3010. DOI: 10.1021/acs.nanolett.9b00164 (cited on page 80).

[170] S. Hunsche, T. Dekorsy, V. Klimov, and H. Kurz. "Ultrafast Dynamics of Carrier-Induced Absorption Changes in Highly-Excited CdSe Nanocrystals." In: *Applied Physics B: Laser and Optics* 62.1 (1996), pp. 3–10. DOI: 10.1007/BF01081240 (cited on page 80).

[171] Verena A. Hintermayr, Lakshminarayana Polavarapu, Alexander S. Urban, and Jochen Feldmann. "Accelerated Carrier Relaxation through Reduced Coulomb Screening in Two-Dimensional Halide Perovskite Nanoplatelets." In: *ACS Nano* 12.10 (2018), pp. 10151–10158. DOI: 10.1021/acsnano.8b05029 (cited on page 83).

[172] George Volonakis, Marina R. Filip, Amir Abbas Haghighirad, Nobuya Sakai, Bernard Wenger, Henry J. Snaith, and Feliciano Giustino. "Lead-Free Halide Double Perovskites *via* Heterovalent Substitution of Noble Metals." In: *The Journal of Physical Chemistry Letters* 7.7 (2016), pp. 1254–1259. DOI: 10.1021/acs.jpclett.6b00376 (cited on page 89).

[173] Cuncun Wu, Qiaohui Zhang, Yang Liu, Wei Luo, Xuan Guo, Ziru Huang, Hungkit Ting, Weihai Sun, Xinrui Zhong, Shiyuan Wei, Shufeng Wang, Zhijian Chen, and Lixin Xiao. "The Dawn of Lead-Free Perovskite Solar Cell: Highly Stable Double Perovskite $Cs_2AgBiBr_6$ Film." In: *Advanced Science* 5.3 (2018), p. 1700759. DOI: 10.1002/advs.201700759 (cited on pages 89, 90).

[174] Muhammad Usman and Qingfeng Yan. "Recent Advancements in Crystalline Pb-Free Halide Double Perovskites." In: *Crystals* 10.2 (2020), p. 62. DOI: 10.3390/cryst10020062 (cited on page 89).

[175] Liang Chu, Waqar Ahmad, Wei Liu, Jian Yang, Rui Zhang, Yan Sun, Jianping Yang, and Xing'ao Li. "Lead-Free Halide Double Perovskite Materials: A New Superstar Toward Green and Stable Optoelectronic Applications." In: *Nano-Micro Letters* 11.1 (2019), p. 6050. DOI: 10.1007/s40820-019-0244-6 (cited on page 89).

[176] Sasha Khalfin and Yehonadav Bekenstein. "Advances in Lead-Free Double Perovskite Nanocrystals, Engineering Band-Gaps and Enhancing Stability through Composition Tunability." In: *Nanoscale* 11.18 (2019), pp. 8665–8679. DOI: 10.1039/c9nr01031a (cited on page 89).

[177] Xin-Gang Zhao, Dongwen Yang, Ji-Chang Ren, Yuanhui Sun, Zewen Xiao, and Lijun Zhang. "Rational Design of Halide Double Perovskites for Optoelectronic Applications." In: *Joule* 2.9 (2018), pp. 1662–1673. DOI: 10.1016/j.joule.2018.06.017 (cited on page 89).

[178] Hang Hu, Binghai Dong, and Wei Zhang. "Low-Toxic Metal Halide Perovskites: Opportunities and Future Challenges." In: *Journal of Materials Chemistry A* 5.23 (2017), pp. 11436–11449. DOI: 10.1039/c7ta00269f (cited on page 89).

[179] Robert L. Z. Hoye, Lissa Eyre, Fengxia Wei, Federico Brivio, Aditya Sadhanala, Shijing Sun, Weiwei Li, Kelvin H. L. Zhang, Judith L. MacManus-Driscoll, Paul D. Bristowe, Richard H. Friend, Anthony K. Cheetham, and Felix Deschler. "Fundamental Carrier Lifetime Exceeding 1 µs in $Cs_2AgBiBr_6$ Double Perovskite." In: *Advanced Materials Interfaces* 5.15 (2018), p. 1800464. DOI: 10.1002/admi.201800464 (cited on pages 89, 92, 100).

[180] Julian A. Steele, Weicheng Pan, Cristina Martin, Masoumeh Keshavarz, Elke Debroye, Haifeng Yuan, Subhasree Banerjee, Eduard Fron, Dries Jonckheere, Cheol Woong Kim, Wouter Baekelant, Guangda Niu, Jiang Tang, Johan Vanacken, Mark van der Auweraer, Johan Hofkens, and Maarten B. J. Roeffaers. "Photophysical Pathways in Highly Sensitive $Cs_2AgBiBr_6$ Double-Perovskite Single-Crystal X-Ray Detectors." In: *Advanced Materials* 30.46 (2018), p. 1804450. DOI: 10.1002/adma.201804450 (cited on pages 89, 100).

[181] Cuncun Wu, Bowen Du, Wei Luo, Yang Liu, Tieyi Li, Duo Wang, Xuan Guo, Hungkit Ting, Zheyu Fang, Shufeng Wang, Zhijian Chen, Yanxue Chen, and Lixin Xiao. "Highly Efficient and Stable Self-Powered Ultraviolet and Deep-Blue Photodetector Based on $Cs_2AgBiBr_6/SnO_2$ Heterojunction." In: *Advanced Optical Materials* 6.22 (2018), p. 1800811. DOI: 10.1002/adom.201800811 (cited on pages 89, 100).

[182] Davide Bartesaghi, Adam H. Slavney, María C. Gélvez-Rueda, Bridget A. Connor, Ferdinand C. Grozema, Hemamala I. Karunadasa, and Tom J. Savenije. "Charge Carrier Dynamics in $Cs_2AgBiBr_6$ Double Perovskite." In: *The Journal of Physical Chemistry C* 122.9 (2018), pp. 4809–4816. DOI: 10.1021/acs.jpcc.8b00572 (cited on page 89).

[183] Amrita Dey, Alexander F. Richter, Tushar Debnath, He Huang, Lakshminarayana Polavarapu, and Jochen Feldmann. "Transfer of Direct to Indirect Bound Excitons by Electron Intervalley Scattering in $Cs_2AgBiBr_6$ Double Perovskite Nanocrystals." In: *ACS Nano* 14.5 (2020), pp. 5855–5861. DOI: 10.1021/acsnano.0c00997 (cited on page 89).

[184] Jiajun Luo, Xiaoming Wang, Shunran Li, Jing Liu, Yueming Guo, Guangda Niu, Li Yao, Yuhao Fu, Liang Gao, Qingshun Dong, Chunyi Zhao, Meiying Leng, Fusheng Ma, Wenxi Liang, Liduo Wang, Shengye Jin, Junbo Han, Lijun Zhang, Joanne Etheridge, Jianbo Wang, Yanfa Yan, Edward H. Sargent, and Jiang Tang. "Efficient and Stable Emission of Warm-White Light from Lead-Free Halide Double Perovskites." In: *Nature* 563.7732 (2018), pp. 541–545. DOI: 10.1038/s41586-018-0691-0 (cited on pages 90, 92, 101).

[185] Maurizia Palummo, Eduardo Berrios, Daniele Varsano, and Giacomo Giorgi. "Optical Properties of Lead-Free Double Perovskites by *Ab Initio* Excited-State Methods." In: *ACS Energy Letters* 5 (2020), pp. 457–463. DOI: 10.1021/acsenergylett.9b02593 (cited on page 92).

[186] Jingxiu Yang, Peng Zhang, and Su-Huai Wei. "Band Structure Engineering of $Cs_2AgBiBr_6$ Perovskite through Order-Disordered Transition: A First-Principle Study." In: *The Journal of Physical Chemistry Letters* 9.1 (2018), pp. 31–35. DOI: 10.1021/acs.jpclett.7b02992 (cited on page 92).

[187] Zewen Xiao, Weiwei Meng, Jianbo Wang, and Yanfa Yan. "Thermodynamic Stability and Defect Chemistry of Bismuth-Based Lead-Free Double Perovskites." In: *ChemSusChem* 9.18 (2016), pp. 2628–2633. DOI: 10.1002/cssc.201600771 (cited on page 92).

[188] S. J. Zelewski, J. M. Urban, A. Surrente, D. K. Maude, A. Kuc, L. Schade, R. D. Johnson, M. Dollmann, P. K. Nayak, H. J. Snaith, P. Radaelli, R. Kudrawiec, R. J. Nicholas, P. Plochocka, and M. Baranowski. "Revealing the Nature of Photoluminescence Emission in the Metal-Halide Double Perovskite $Cs_2AgBiBr_6$." In: *Journal of Materials Chemistry C* 7.27 (2019), pp. 8350–8356. DOI: 10.1039/C9TC02402F (cited on page 93).

[189] Julian A. Steele, Pascal Puech, Masoumeh Keshavarz, Ruoxi Yang, Subhasree Banerjee, Elke Debroye, Cheol Woong Kim, Haifeng Yuan, Nam Ho Heo, Johan Vanacken, Aron Walsh, Johan Hofkens, and Maarten B. J. Roeffaers. "Giant Electron-Phonon Coupling and Deep Conduction Band Resonance in Metal Halide Double Perovskite." In: *ACS Nano* 12.8 (2018), pp. 8081–8090. DOI: 10.1021/acsnano.8b02936 (cited on pages 95, 100).

[190] Martina Pantaler, Kyung Taek Cho, Valentin I. E. Queloz, Inés García Benito, Christian Fettkenhauer, Irina Anusca, Mohammad Khaja Nazeeruddin, Doru C. Lupascu, and Giulia Grancini. "Hysteresis-Free Lead-Free Double-Perovskite Solar Cells by Interface Engineering." In: *ACS Energy Letters* 3.8 (2018), pp. 1781–1786. DOI: 10.1021/acsenergylett.8b00871 (cited on page 100).

[191] Enrico Greul, Michiel L. Petrus, Andreas Binek, Pablo Docampo, and Thomas Bein. "Highly Stable, Phase Pure $Cs_2AgBiBr_6$ Double Perovskite Thin Films for Optoelectronic Applications." In: *Journal of Materials Chemistry A* 5.37 (2017), pp. 19972–19981. DOI: 10.1039/C7TA06816F (cited on page 100).

[192] Po-Kai Kung, Ming-Hsien Li, Pei-Ying Lin, Jia-Yun Jhang, Martina Pantaler, Doru C. Lupascu, Giulia Grancini, and Peter Chen. "Lead-Free Double Perovskites for Perovskite Solar Cells." In: *Solar RRL* 4.2 (2019), p. 1900306. DOI: 10.1002/solr.201900306 (cited on page 100).

[193] Jie Yang, Chunxiong Bao, Weihua Ning, Bo Wu, Fuxiang Ji, Zhibo Yan, Youtian Tao, Jun-Ming Liu, Tze Chien Sum, Sai Bai, Jianpu Wang, Wei Huang, Wenjing Zhang, and Feng Gao. "Stable, High-Sensitivity and Fast-Response Photodetectors Based on Lead-Free $Cs_2AgBiBr_6$ Double Perovskite Films." In: *Advanced Optical Materials* 58 (2019), p. 1801732. DOI: 10.1002/adom.201801732 (cited on pages 100, 101).

[194] Weicheng Pan, Haodi Wu, Jiajun Luo, Zhenzhou Deng, Cong Ge, Chao Chen, Xiaowei Jiang, Wan-Jian Yin, Guangda Niu, Lujun Zhu, Lixiao Yin, Ying Zhou, Qingguo Xie, Xiaoxing Ke, Manling Sui, and Jiang Tang. "$Cs_2AgBiBr_6$ Single-Crystal X-Ray Detectors with a Low Detection Limit." In: *Nature Photonics* 11.11 (2017), pp. 726–732. DOI: 10.1038/s41566-017-0012-4 (cited on page 100).

[195] Tong Li, Jing Wang, Ziyan Gao, Peng Lv, Yuben Yang, Junsheng Wu, Jiawang Hong, Xueyun Wang, and Yanwen Zhou. "Local Stress Enhanced Photocurrent of Visible Light Photo-Detection in $Cs_2AgBiBr_6$ Single Crystal." In: *Applied Physics Letters* 115.13 (2019), p. 131103. DOI: 10.1063/1.5116088 (cited on page 100).

[196] Zhenzhen Zhang, Yongqi Liang, Hanlin Huang, Xingyi Liu, Qi Li, Langxing Chen, and Dongsheng Xu. "Stable and Highly Efficient Photocatalysis with Lead-Free Double-Perovskite of $Cs_2AgBiBr_6$." In: *Angewandte Chemie, International Edition* 58.22 (2019), pp. 7263–7267. DOI: 10.1002/anie.201900658 (cited on page 100).

[197] Lei Zhou, Yang-Fan Xu, Bai-Xue Chen, Dai-Bin Kuang, and Cheng-Yong Su. "Synthesis and Photocatalytic Application of Stable Lead-Free $Cs_2AgBiBr_6$ Perovskite Nanocrystals." In: *Small* 14.11 (2018), p. 1703762. DOI: 10.1002/smll.201703762 (cited on page 100).

[198] George Volonakis and Feliciano Giustino. "Surface Properties of Lead-Free Halide Double Perovskites: Possible Visible-Light Photo-Catalysts for Water Splitting." In: *Applied Physics Letters* 112.24 (2018), p. 243901. DOI: 10.1063/1.5035274 (cited on page 100).

[199] Liyuan Dong, Shijing Sun, Zeyu Deng, Wei Li, Fengxia Wei, Yajun Qi, Yanchun Li, Xiaodong Li, Peixiang Lu, and U. Ramamurty. "Elastic Properties and Thermal Expansion of Lead-Free Halide Double Perovskite $Cs_2AgBiBr_6$." In: *Computational Materials Science* 141 (2018), pp. 49–58. DOI: 10.1016/j.commatsci.2017.09.014 (cited on page 100).

[200] Robin Kentsch, Mirko Scholz, Jonas Horn, Derck Schlettwein, Kawon Oum, and Thomas Lenzer. "Exciton Dynamics and Electron–Phonon Coupling Affect the Photovoltaic Performance of the $Cs_2AgBiBr_6$ Double Perovskite." In: *The Journal of Physical Chemistry C* 122.45 (2018), pp. 25940–25947. DOI: 10.1021/acs.jpcc.8b09911 (cited on page 100).

[201] Christopher N. Savory, Aron Walsh, and David O. Scanlon. "Can Pb-Free Halide Double Perovskites Support High-Efficiency Solar Cells?" In: *ACS Energy Letters* 1.5 (2016), pp. 949–955. DOI: 10.1021/acsenergylett.6b00471 (cited on page 100).

[202] Xiaoqing Yang, Yonghui Chen, Pengyun Liu, Huimin Xiang, Wei Wang, Ran Ran, Wei Zhou, and Zongping Shao. "Simultaneous Power Conversion Efficiency and Stability Enhancement of $Cs_2AgBiBr_6$ Lead-Free Inorganic Perovskite Solar Cell through Adopting a Multifunctional Dye Interlayer." In: *Advanced Functional Materials* 30.23 (2020), p. 2001557. DOI: 10.1002/adfm.202001557 (cited on page 100).

[203] Bin Yang, Junsheng Chen, Songqiu Yang, Feng Hong, Lei Sun, Peigeng Han, Tõnu Pullerits, Weiqiao Deng, and Keli Han. "Lead-Free Silver-Bismuth Halide Double Perovskite Nanocrystals." In: *Angewandte Chemie, International Edition* 57.19 (2018), pp. 5359–5363. DOI: 10.1002/anie.201800660 (cited on page 101).

[204] Abhoy Karmakar, Mya S. Dodd, Satyam Agnihotri, Enrico Ravera, and Vladimir K. Michaelis. "Cu(II)-Doped $Cs_2SbAgCl_6$ Double Perovskite: A Lead-Free, Low-Bandgap Material." In: *Chemistry of Materials* 30.22 (2018), pp. 8280–8290. DOI: 10.1021/acs.chemmater.8b03755 (cited on page 101).

[205] T. Thao Tran, Jessica R. Panella, Juan R. Chamorro, Jennifer R. Morey, and Tyrel M. McQueen. "Designing Indirect–Direct Bandgap Transitions in Double Perovskites." In: *Materials Horizons* 4.4 (2017), pp. 688–693. DOI: 10.1039/C7MH00239D (cited on page 101).

[206] Xue-Feng Cheng, Wen-Hu Qian, Jia Wang, Chuang Yu, Jing-Hui He, Hua Li, Qing-Feng Xu, Dong-Yun Chen, Na-Jun Li, and Jian-Mei Lu. "Environmentally Robust Memristor Enabled by Lead-Free Double Perovskite for High-Performance Information Storage." In: *Small* 15.49 (2019), p. 1905731. DOI: 10.1002/smll.201905731 (cited on page 101).

[207] Zhenhua Weng, Jiajun Qin, Akrajas Ali Umar, Jiao Wang, Xin Zhang, Haoliang Wang, Xiaolei Cui, Xiaoguo Li, Lirong Zheng, and Yiqiang Zhan. "Lead-Free $Cs_2BiAgBr_6$ Double Perovskite-Based Humidity Sensor with Superfast Recovery Time." In: *Advanced Functional Materials* 29.24 (2019), p. 1902234. DOI: 10.1002/adfm.201902234 (cited on page 101).

[208] Kiran Prabhu and Aravind Kumar Chandiran. "Solar Energy Storage in a $Cs_2AgBiBr_6$ Halide Double Perovskite Photoelectrochemical Cell." In: *Chemical Communications* 56.53 (2020), pp. 7329–7332. DOI: 10.1039/D0CC02743J (cited on page 101).

List of Figures

List of Tables

List of Abbreviations

APD	avalanche photodiode
BBO	BaB_2O_4 (beta barium borate)
BRF	birefringent filter (also known as *Lyot filter*)
CB	conduction band
CBM	conduction band minimum
CCD	charge-coupled device
CeNS	Center for NanoScience
CTA	$CsTiOAsO_4$ (cesium titanyl arsenate)
CW	continuous wave
DFT	density functional theory
DP	double perovskite
DPG	German Physical Society
DT	differential transmission
e	electron
ELQ-LED	Electroluminescent Quantum Materials-Based Light-Emitting Device
FCC	face-centered cubic
FRET	Förster resonance energy transfer
FWHM	full width at half maximum
h	hole
he	heavy electron
hh	heavy hole
IR	infrared
IRF	instrument response function
KTP	$KTiOPO_4$ (potassium titanyl phosphate)
LA	longitudinal acoustic
LBO	LiB_3O_5 (lithium triborate)
LD	laser diode
le	light electron
LED	light-emitting diode
lh	light hole
LO	longitudinal optical
MCP	multi-channel plate

ML	mode-locked
NA	numerical aperture
NC	nanocrystal
NIM	Nanosystems Initiative Munich
OD	optical density
OPA	optical parametric amplifier
OPO	optical parametric oscillator
PD	photodiode
PL	photoluminescence
PLE	photoluminescence excitation
QD	quantum dot
QY	quantum yield
SHG	second-harmonic generation
soe	split-off electron
soh	split-off hole
SolTech	Solar Technologies go Hybrid
TA	transverse acoustic
TCSPC	time-correlated single photon counting
TEM	transmission electron microscope
THG	third-harmonic generation
Ti:sapphire	Ti:Al_2O_3 (titanium-doped sapphire)
UV	ultraviolet
VB	valence band
VBM	valence band maximum
WLL	white-light laser
YAG	$Y_3Al_5O_{12}$ (yttrium aluminium garnet)

Acknowledgments

It was a great experience for me to conduct my research at the *Chair for Photonics and Optoelectronics*. During my time as a PhD student, I learned a lot, not only scientifically but also personally. Many people were involved in my research project and I would like to take this opportunity to thank them for their support and friendship.

First of all, I want to thank my 'Doktorvater' **Prof. Dr. Jochen Feldmann** as he gave me the possibility to work on such an intriguing project in a great scientific environment. Our highly productive discussions were crucial for the success of my work. I benefited a lot from his broad scientific knowledge and experience, which is still inspiring to me. Furthermore, he made it possible that I could participate and present my results not only at the stimulating meetings of the ELQ-LED project but also at various (international) conferences. In this context, I especially want to highlight his extremely valuable feedback on all my presentations, posters, and manuscripts. During our moving to the *Nano-Institute Munich*, he gave me the opportunity to look for new high-end scientific equipment and to set it up successfully. I thank him for the trust he has placed in me.

I also want to thank **PD Dr. Theobald Lohmüller**, **Dr. Lakshminarayana Polavarapu**, and **Dr. Jacek K. Stolarczyk** for the great collaborations. For example, in all the perovskite projects and during the moving. At the beginning of my time as a PhD student, **Prof. Dr. Alexander S. Urban** was still an assistant at this chair, but now he has his own research group. Nevertheless, we have always been connected within the ELQ-LED project and I thank him for his constant support.

A special thanks goes to my dear colleagues and friends who helped me proofreading this thesis: **Stefanie D. Pritzl**, **Ilka Vinçon**, **Sebastian Rieger**, and **Amrita Dey**.

I want to highlight the great experience of supervising master students. Many thanks to **Anja Barfüßer** and **Michael Binder** — it was always a pleasure to work with you!

All the scientific work would not have been as much fun if there were no great colleagues and entertaining lunch breaks. Therefore, I want to thank all of them who enriched my time at the chair: all previously mentioned people and **Nicola Kerschbaumer**, **Dr. En-Ping Yao**, **Simone Strohmair**, **Francis Schuknecht**, **Dr. He Huang**, **Dr. Tushar Debnath**, **Jiawen Fang**, **Yiou Wang**, ...

Additionally, I want to thank my former colleagues and I am glad that we still see each other regularly: **Dr. Bernhard J. Bohn**, **Dr. Aurora Manzi**, **Dr. Verena A. Hintermayr**, **Florian Ehrat**, **Dr. Carla Pernpeintner**, **Christoph Maier**, and **Patrick Urban**.

Many thanks goes to **Gerlinde Adam** for her great help regarding administrative work. I also want to thank **Stefan Niedermaier** and **Talee Barghouti** for the technical support in the laboratories, especially during the moving.

I also thank the partners of the ELQ-LED project for an exciting cooperation and productive meetings. A special thanks goes to **Merck** and **Fraunhofer IAP** who provided me with high-quality samples.

Finally, I want to express my gratitude to my wife **Anna** who always motivated me and kept my back free when I had to focus on my thesis. And last but not least, I thank my parents **Edith** and **Jürgen** as well as my sister **Ulrike** for their constant support.